博士論文

Studies on Gelation Kinetics and Elasticity-Structure Relationship of Model Polymer Networks

（モデル高分子網目からなるゲルの反応動力学および弾性-構造相関に関する研究）

西　健吾

Contents

Chapter 1

General Introduction

1.1 Historical Background

When an infinite polymer network is formed by an introduction of cross-links into polymer solutions or melts, one can observe a transition from viscous solution to elastic solid. This transition is called sol-gel transition. A variety of commercial products, namely rubbers, gels, paints, and adhesives, are made by way of gelation point, i.e., the onset of formation of infinitely large clusters. Hence, the understanding of sol-gel transition or the network formation is of particular importance not only from basic science but also from industrial points of view.

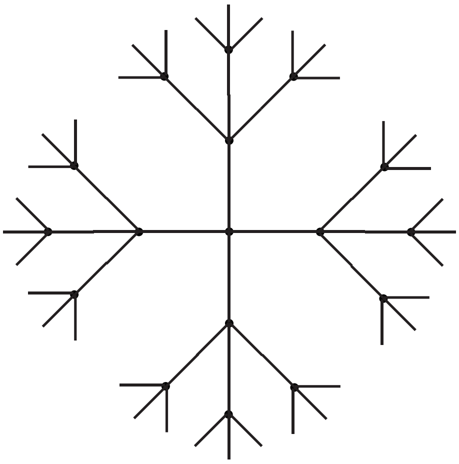

Figure 1.1: Schematic picture of Bethe lattice.

The early studies of the sol-gel transition date back to the onset of the polymer science. The first quantitative theories of gelation is the tree-like theory proposed by Flory[1] and Stockmayer[2] in 1940's. Afterwards, Gordon[3–5] organized this theory by utilizing cascade theory proposed by Good.[6,7] This theory postulates that all sites of an infinite Bethe lattice are occupied by monomers and the possible bonds between neighboring monomers are either formed with probebility p or left unreacted with probability $1-p$. Here, a small part of Bethe lattice is shown in Fig. 1.1.

From this theory, we can analytically calculate the physical properties, such as gelation point, cluster distribution, and elastic modulus.[8–10] For example, the gelation point for f-functional Bethe lattice is given by

$$p_c = \frac{1}{f-1} \quad , \tag{1.1}$$

which well corresponds to experimental results. Furthermore, by using this theory, we can evaluate the reaction probability p from sol fraction, and calculate the elastic modulus G by using p.[8–10]

However, this theory has been criticized because of its unrealistic assumption, i.e., the absence of closed loops.[11,12] Because of this assumption, fractal dimension of an infinite tree-cluster is 4 and it cannot fit in 3D space. Concretely speaking, when a cluster grows in a radial direction at $f = 3$, there is no room to grow beyond 6th generation. As shown in this example, percolation does not occur in the tree-like theory in 3D.[11]

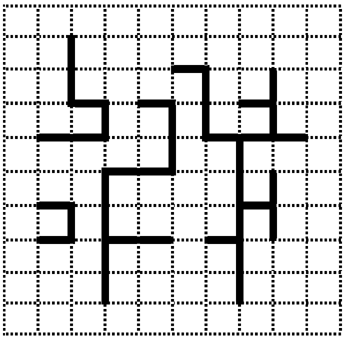

Figure 1.2: Schematic picture of percolation theory.

In 1970's, the studies of phase transition and critical phenomena were applied to the sol-gel transition. Stauffer and de Gennes applied percolation theory to the cross-linking process of polymer network.[12,13] In this theory, all sites of lattice such as square lattice and cubic lattice are occupied by monomers and the possible bonds between neighboring monomers are either formed with probebility p or left unreacted with probability $1-p$ as shown in Fig 1.2. Note that this theory contains loops, which is not taken into account in the tree-like theory. Critical exponents predicted from the tree-like theory and percolation theory are summarize in Table 1. As shown in Table 1, there are big differences in the critical exponents between tree-like theory and percolation theory.

exponent	percolation		tree-like theory	physical property
	$d=2$	$d=3$		$(\varepsilon=p-p_c)$
β	5/36	0.45	1	gel fraction : $\theta\sim\lvert\varepsilon\rvert^{\beta}$
γ	43/18	1.74	1	average polymerization index : $Z\sim\lvert\varepsilon\rvert^{-\gamma}$
ν	4/3	0.88	1/2	correlation length : $\xi\sim\lvert\varepsilon\rvert^{-\nu}$
k	?	0.7∼0.9?	0	viscosity : $\eta\sim\lvert\varepsilon\rvert^{-k}$
f_{el}	4/3?	1.7∼1.9?	3	elastic modulus : $G\sim\lvert\varepsilon\rvert^{f_{\mathrm{el}}}$

Table 1.1: Comparison of critical exponents between tree-like theory and percolation theory. ? means that there is room for argument.

The validity of the percolation theory is partly confirmed by experiments. For example, Martin et al.[14] made a dynamic light scattering study of the decay of density fluctuations in reacting sol-gels.(Fig. 1.3) At gelation point, the dynamic structure factor $S(q,t)$ becomes a power low with an exponents of ~ 0.27, which agrees with the prediction of the percolation theory: $0.24\sim 0.26$.[15] When studying the elastic response of gels, the theoretical prediction of the critical exponent f_{el} well corresponds to the simulation results.[16,17] However, experiments give a wide range of values of the critical exponent f_{el} that groups into different families: (i) $f_{\mathrm{el}}\sim 2$ observed in gelatin gels,[18,19] silica gels[20] and agarose gels,[21] (ii) $f_{\mathrm{el}}\sim 3$ observed in polyester gels,[22,23] epoxy gels[25] and branched polymer gels.[26] One of the reasons for this discrepancy is due to the difficulty in measuring p_c and the elastic modulus near p_c experimentally.

Unlike the tree-like theory, there is no simple relation between the number of unreacted groups on a branched polymer and its degree of polymerization.[11] Consequently, general percolation problems have no simple analytical solution, but have been solved by computer simulation and by approximation. Many approximation methods for the absolute values of percolation conductivity problem[27–29] (Fig. 1.4) have been proposed and applied to diffusion in amorphous and inhomogeneous materials[30] and spinwave properties in disordered ferromagnets.[16] However, no approximation methods for the absolute values of the physical properties of polymer network have been proposed though scaling laws are proposed in the percolation theory.

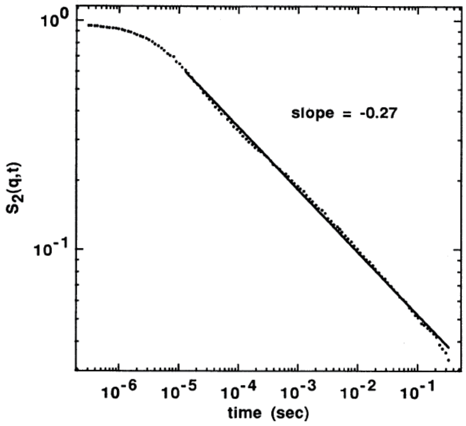

Figure 1.3: The dynamic structure factor of silica gel at the gelation point.[14]

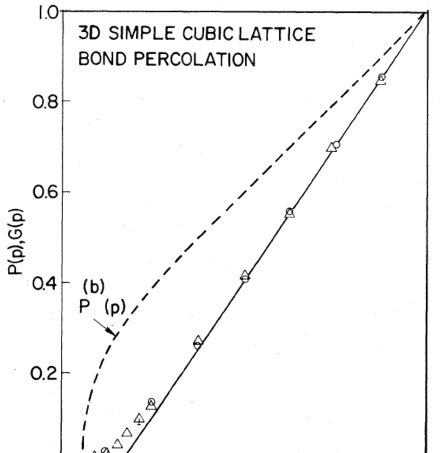

Figure 1.4: Percolation probability, $P(p)$ (dashed line), and conductance, $G(p)$ (data points), for bond percolation on 3D simple cubic network. $G(p)$ is normalized to unity at $p = 1$. The solid line indicates the prediction of the effective medium approximation.[27]

From above discussion, one comes to understand that one of the most important factors determining the physical properties of polymer network is the connectivity probability p. Thus, the knowledge for the gelation kinetics is important. Let us consider the AB-type polycondensation of multifunctional monomers. In general, when the mean-field approximation is applied to the reactivity of terminal functional group, the reaction rate equation is expected to be described as a simple reaction rate equation.

$$\frac{dC_A(t)}{dt} = \frac{dC_B(t)}{dt} = -kC_A(t)C_B(t) \tag{1.2}$$

Here, $C_A(t)$, $C_B(t)$, and k are the concentrations of species A and B and reaction rate constant. However, in many cases, the gelation kinetics can not be described so simply because gelation kinetics is generally complicated due to some effective factors relative to ordinary chemical kinetics with low molecular weight. The first one is the substitution effect originated from a reaction probability of one terminal group to another.[1] This effect can be either positive or negative depending on the electron state, which is typical in a reaction using low-molecular-weight cross-linkers as is well known. Hence, it is difficult to assume the reactivity of terminal groups to be constant during the gelation. The second one is the steric hindrance. When we use low-molecular-weight cross-linkers in the gelation,[34–36] it is easily expected that reactive sites are buried in the cluster formed in the course of reaction. In this case, the contact probability of reaction site appreciably decreases during the network formation process. Lastly, the diffusion motion of clusters also affects the cross-linking kinetics. Because clusters grow during the gelation process, the diffusion motion of clusters changes with time and complicates the gelation kinetics.

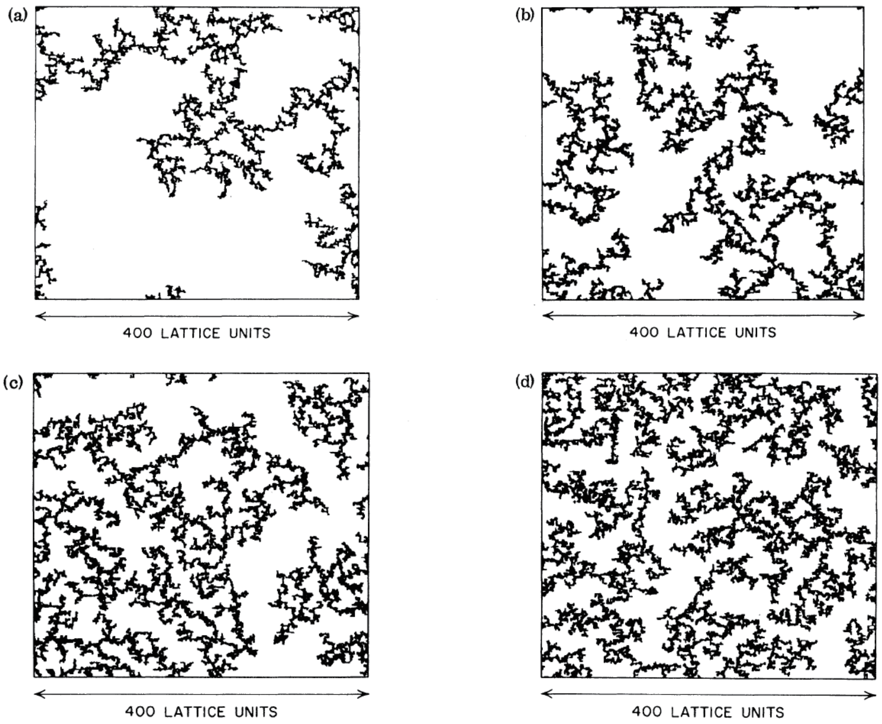

Figure 1.5: The final stage of simulations on 400×400 lattice. In (a) the cluster contains 10,000 particles; for (b) $N = 15,000$; (c) $N = 20,000$; and for (d) $N = 25,000$.[31]

A typical model for the diffusion-controlled gelation is cluster-clester aggregation. In this model, particles diffuse, collide, and aggregate each other. Typical simulation results are shown in Fig. 1.5.[31] As shown in Fig. 1.5, an infinite network is formed in the system with an increase of the particle density.

The kinetics of this process can be described by the mean-field approach of the Smoluchowski equation accurately if the fractal geometry of the clusters is taken into account.[32] The Smoluchowski equation is given by

$$\frac{\partial C_k(t)}{\partial t} = \frac{1}{2}\sum_{i+j=k} K_{ij} C_i(t) C_j(t) - C_k(t) \sum_{j=1}^{\infty} K_{kj} C_j(t) \quad , \tag{1.3}$$

Here, $C_i(t)$ and K_{ij} are the concentration of i-mers and the collision coefficient, respectively. This equation means that k-mer develops because the concentration of k-mers is increased by all reactions between i-mers and j-mers such that $i + j = k$, and reduced by reactions between k-mers and all the rest. This equation can be analytically solved when the collision coefficient K_{ij} is $i + j$ and ij.[33]

Compared to theoretical and model studies, real experiments are far more complicated. As an example, let us see multifunctional monomer radical-polymerization, such as the homopolymerization of dimethacrylate and the copolymerization of metylmethacrylate and ethylene glycol dimethacrylate.[37–54] The cross-linking kinetics of free radical polymerization proceeds by the following two reactions.

$$\frac{d\left[R\right]}{dt} = -k_t\left[R\right]^2 \tag{1.4}$$

$$\frac{d\left[M\right]}{dt} = -k_p\left[R\right]\left[M\right] \tag{1.5}$$

Here, $[R]$ and $[M]$ denote the concentration of radicals and double bonds, respectively. Eq. 1.4 corresponds to the connecting kinetics between different radicals attached to polymer ends and called "termination". On the other hand, Eq. 1.5 corresponds to the polymerization and called "propagation".

The termination is a diffusion-limited process, which occurs by one of two mechanisms. The first mechanism involves translational and/or segmental diffusion of macroradicals, which is continually decreasing with increasing conversion in the system. The second has been called reaction diffusion and occurs as immobile radicals on the network react through unreacted double bonds in their vicinity to move and encounter a second radical for termination.

Because of these mechanisms, multifunctional monomer polymerizations exhibit many complex features including autoacceleration and autodeceleration,[47–50] limiting double bond conversion,[47, 51–53] polymerization kinetics which is dependent on the rate of the polymerization[47, 54] as shown in Fig. 1.6. Furthermore, many researchers showed that these polymerization behaviors relates to cross-linking density[37–42] and chain length in the monomer.[43–46] Because these behaviors are complex, the reaction mechanism of multifunctional monomer cross-linking is not fully understood.

The formation process of polymer network during cross-linking reaction has been investigated by scattering experiments. Especially, many studies of time-resolved dynamic light scattering on sol-gel transition were conducted. As an expamle, dynamic light scattering (DLS) results on gelation process of silica gel is shown in Fig. 1.7.[14] Here, gelation time t_{gel} is 406 min. As a gel point approaches, a pronounced slowing down of the relaxation is observed, until at the gel point an ultraslow power-law decay becomes evident. This indicates that the cluster distribution diverges at the gel point

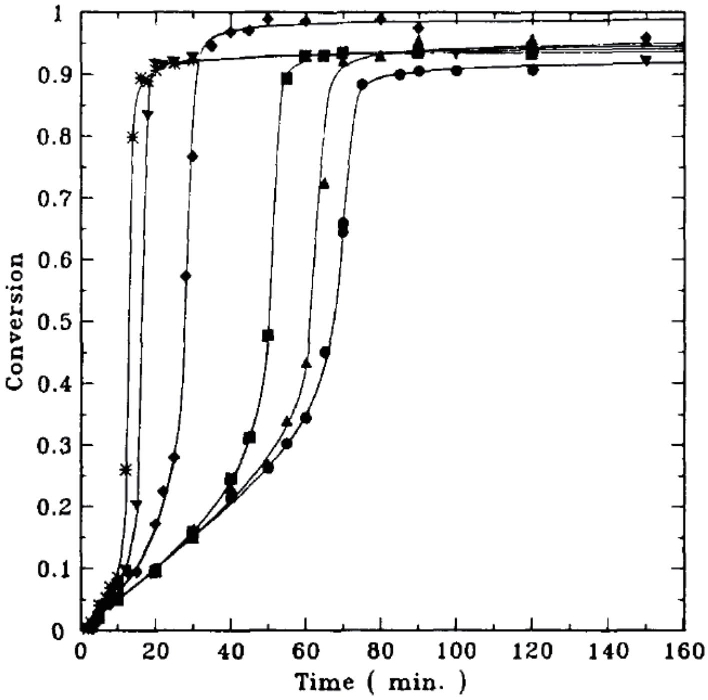

Figure 1.6: Conversion-time histories for the polymerization of methyl methacrylate (MMA) /ethylene glycol dimethacrylate (EGDMA) at 70°C, and various concentration of EGDMA (wt%) : 0 (circle), 0.3 (triangle), 1.0 (square), 5.0 (diamond), 15.0 (reverse triangle), 25.0 (asterisk).[38]

as predicted from percolation theory and leads to an broad spectrum of relaxation time.

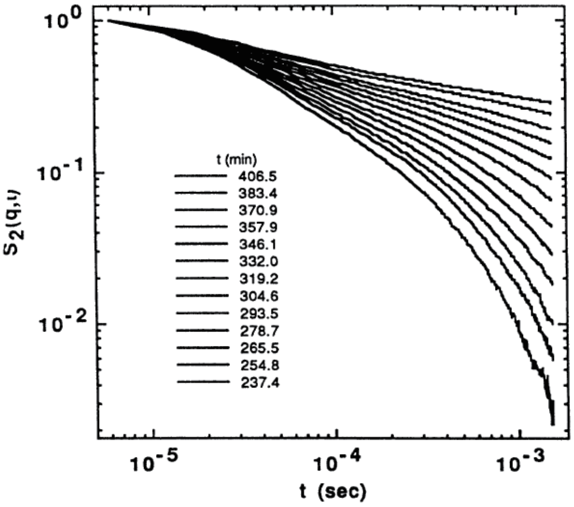

Figure 1.7: Correlation functions for gelling tetramethoxysilicon solution.[14]

On the other hand, there are few static scattering experiments on gelation process because it takes much time for one measurement. Therefore, most of the static scattering studies compare the scattering profile of solution with that of gel. The typical result is shown in Fig. 1.8. This gel was made by the so-called "End-linking" method, i.e., end-coupling of telechelic polymer having a sharp molecular weight distribution by multifunctional cross-linker.[56–59] As seen in Fig. 1.8, it is observed that the gel exhibits a large excess of scattering intensity with respect to the solution for almost the full range of the scattering vector, q, which indicates the existence of heterogeneities. In addition, as swelling ratio Q is increased, the heterogeneities seems to be enhanced.

Several theoretical models to deal with these heterogeneities are proposed.[60,61] Bastide and Leibler proposed a theoretical model based on a percolation of blobs.[61] They considered a reaction bath in the semi-dilute regime and introduce at random and rapidly some cross-links in the solution. (Fig. 1.9) In this process, the network structure coincides with the semi-dilute polymer solution, so the difference of scattering function between semi-dilute solutions and gels cannot be observed. However, when this network is swollen, we have a subtle interspersion of two media: the frozen blob cluster with "high" cross-linking densities and the "interstitial" medium with

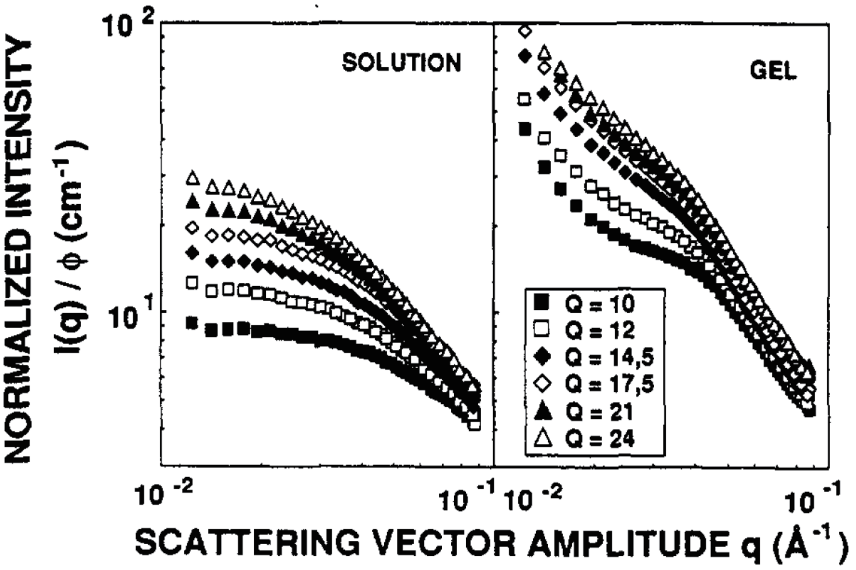

Figure 1.8: Scattering intensity for the end-linked gel and for a semi dilute solution of the same volume fraction ϕ. Several swelling ratios ($Q = 1/\phi$) are shown[55]

low cross-linking densities. This spatial separation of the "high" cross-linking region is responsible for the formation of concentration fluctuations at large scales.(Fig. 1.9) Consequently, according to this approach, an increase in scattering intensity at small angles should be observed. (Fig. 1.10) This model well explains the reason of increment of the scattering function with increasing swelling ratio. Though this model assumes that the difference of scattering function between semi-dilute solutions and gels cannot be observed, many experiments reveals the existence of heterogeneities even in as-prepared state.

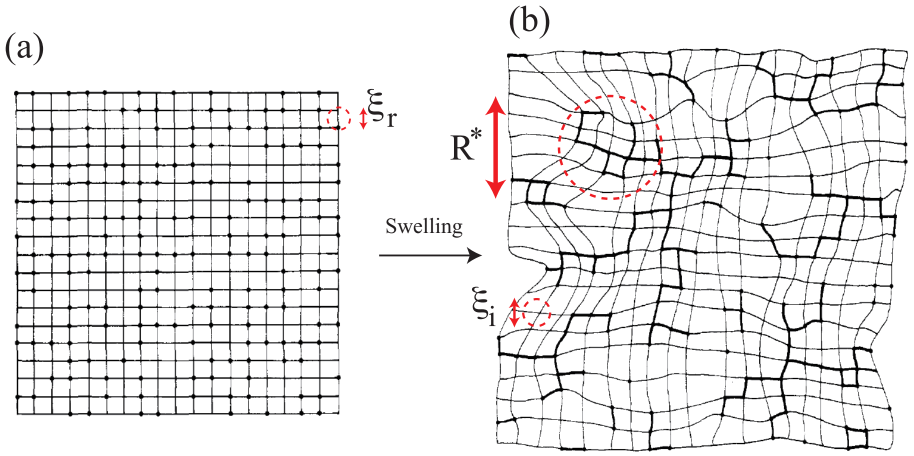

Figure 1.9: (a)Schematic representation of a reaction bath well above the gelation threshold. The size of the lattice site is ξ_r. Black dots represent the interchain cross-links, placed at random. (b)Schematic representation of the overswollen gel by the addition of solvent. ξ_i and R^* denotes the screening length and the size of frozen blob, respectively. The clusters of first chemical neighbor junctions (frozen blobs), which do not swell, are representd by thick solid lines.[61]

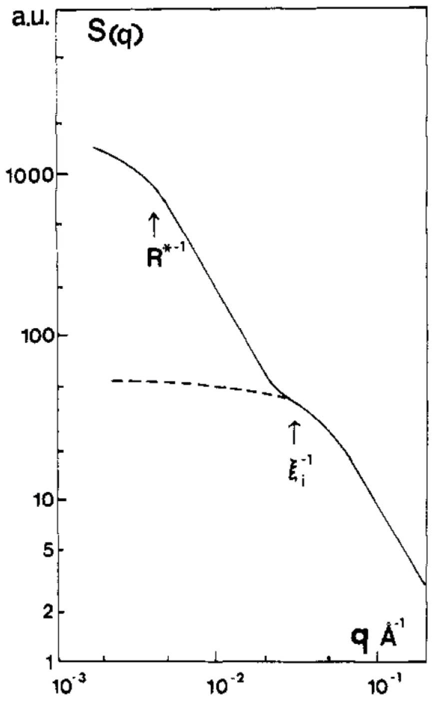

Figure 1.10: Scattering intensity by a swollen network. ξ_i and R^* denote the screening length of the interstitial medium and the size of frozen blob clusters.[61]

To summarize the points so far, though several theories dealing with simple system are proposed, the corresponding experiments are far more complicated and it is difficult to check the validity of these theories. In order to overcome these difficulties, simple and homogeneous gels are desired.

Sakai et al.[62] developed a novel class of hydrogels, called Tetra-PEG gel, which consists of two kinds of four-arm polyethylene glycol (PEG) macromers of the same size, tetraamine-terminated PEG (TAPEG) and tetra-NHS-glutarate-terminated PEG (TNPEG). (Fig. 1.11) Here, NHS represents for *N*-hydroxysuccinimide. Fig. 1.12 and Fig. 1.13 show the scattering functions of as-prepared gels and swollen gels for various concentration and molecular weight of primary polymer.[63] Heterogeneities are not observed not only in as-prepared state but also in swollen state. This indicates that Tetra-PEG gels can be an "ideal polymer network" without significant entanglements and/or defects.

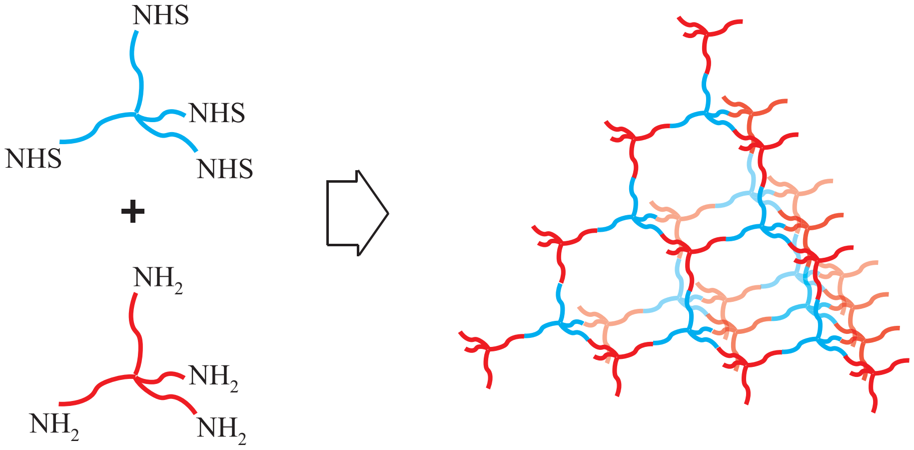

Figure 1.11: Schematic illustration of fabrication scheme of Tetra-PEG gel.

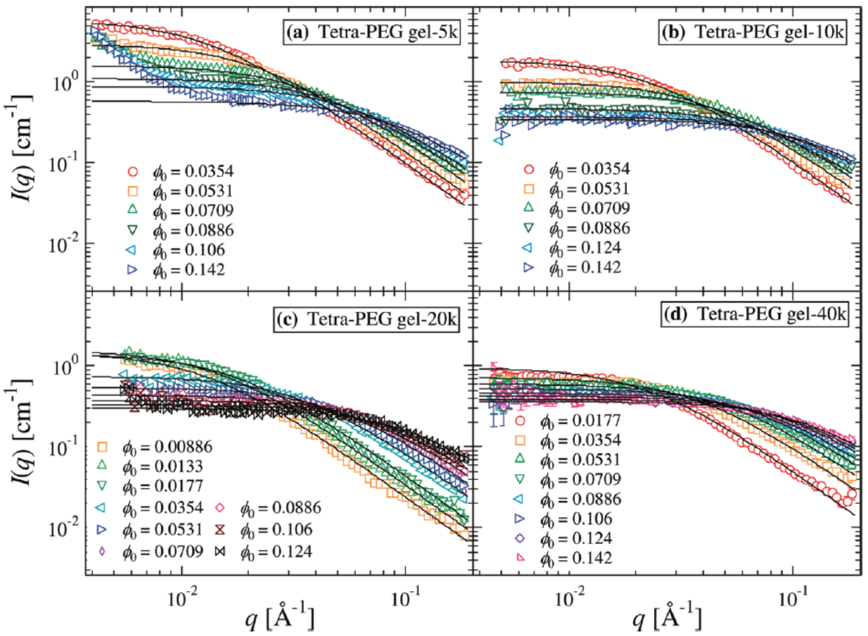

Figure 1.12: SANS curves of as prepared Tetra-PEG gels. The molecular weights of primary polymer are (a) 5, (b) 10, (c) 20, (d) 40 kg/mol.[63]

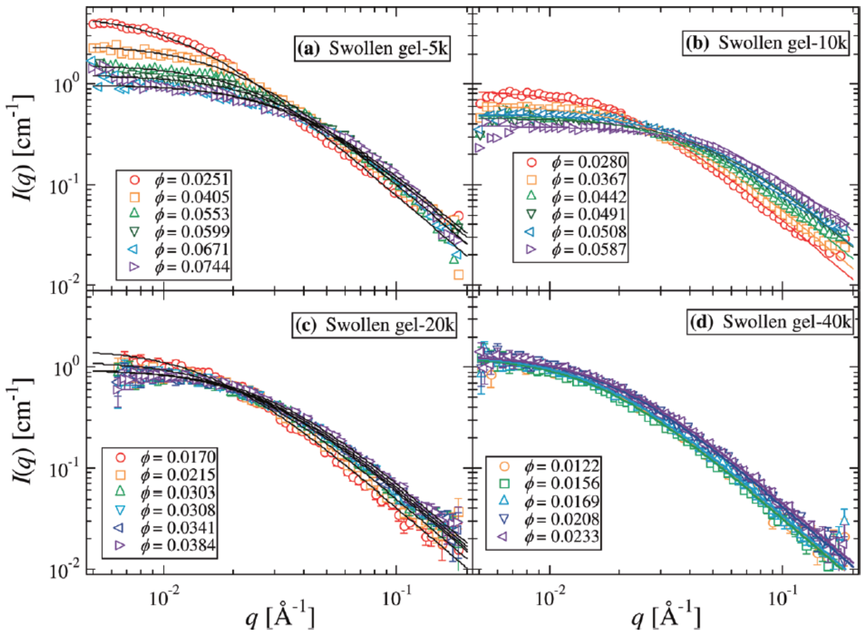

Figure 1.13: SANS curves of swollen Tetra-PEG gels. The molecular weights of primary polymer are (a) 5, (b) 10, (c) 20, and (d) 40 kg/mol.[63]

In addition, Tetra-PEG gels come into use to check the validity of theories of rubber elasticity.[64–70] Let us review one of them.[65] The elastic modulus of polymer network is correlated with the concentration of elastically effective chains by three popular models; the affine, phantom, and junction affine network models. The difference between these models is the fluctuation of cross-links. The affine model assumes that cross-links are firmly connected to the macroscopic body and network strands deform in the same manner with the macroscopic deformation. On the other hand, the phantom network model assumes that cross-links fluctuate, and the deformation of the network strand is suppressed by thermal fluctuations. The junction affine model is the intermediate of these models. Although these models are often used, the requirement conditions for each model or even the validity of each model were not known. Akagi et al. performed the stretching and tearing tests, and for the first time, observed the transition between the phantom and affine network models around the overlapping concentration of prepolymers.(Fig. 1.14) This result indicates that Tetra-PEG gel have near-ideal network and is suitable material for examination of rubber elasticity.

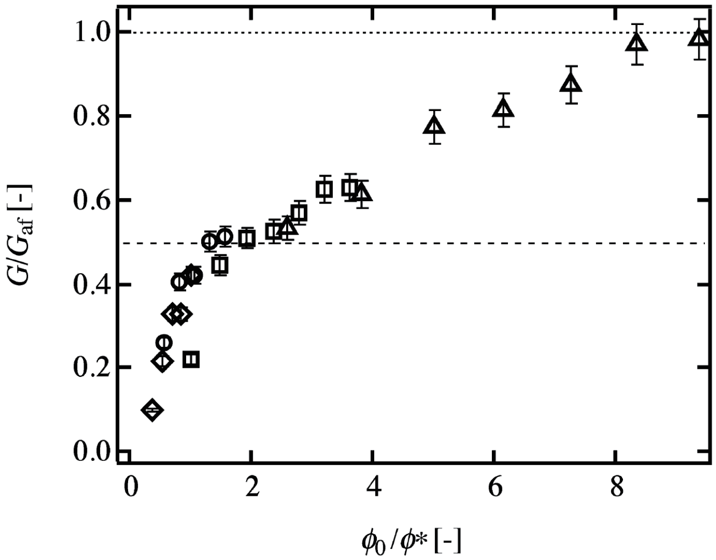

Figure 1.14: The value of G/G_{af} as a function of ϕ_0/ϕ^* for the Tetra-PEG gels. Here, G_{af} denotes the predicted value from affine network model. The molecular weight of primary polymer is 5 kg/mol (rhombus), (b) 10 kg/mol (circle), (c) 20 kg/mol (square), and (d) 40 kg/mol (triangle).The dashed and dotted lines are the guides showing $G/G_{\mathrm{af}} = 0.5$ and 1.0, respectively.[65]

1.2 Outline of the Dissertation

By considering the above discussion, I intended to solve above difficulties in the gelation kinetics as well as rubber elasticity and structure analysis by using ideal polymer network, i.e., Tetra-PEG gel. The following is the lineup of the contents of this dissertation.

In Chapter 2 and 3, I report the kinetic study on the gelation reaction of Tetra-PEG gel system studied by ATR-IR and spectrophotometry. In general, the reaction rate changes during the gelation process because cluster grows and mobility of cluster changes. However, in contrast to ordinary cross-linking systems, it is revealed that the gelation kinetics of Tetra-PEG gel undergoes a simple second-order reaction from beginning to end in Chapter 2. Furthermore, in Chapter 3, we discuss the reason of smooth second-order kinetics of Tetra-PEG gel by extending our study to volume fraction of polymer and primary molecular weight (M_w) dependences of the rate constant in order to discuss the effect of mobility of clusters on gelation kinetics.

In Chapter 4 and 5, I discuss the elasticity of bond-disordered polymer network. The assumption of no closed-loop formation in tree-like theory has been criticized as being unrealistic. Thus in this study, I propose new theories for the elastic modulus of bond-disordered polymer network such as triangular and cubic lattice. In Chapter 4, I derive the first approximation of the elastic modulus G around $p = 1$, and pointed out that it does not depend the local topology of the network structure or the existence of the loops. However, there are two problems at this stage: (1) the applicable region of the first approximation could not be defined and (2) the elastic modulus in the critical region could not be calculated. In order to solve these problems, in Chapter 5, I propose an approximate equation to predict not only the gelation threshold, p_c, and the critical exponent but also the absolute values of elastic modulus G for $p \geq p_c$. The validity of these theories were confirmed by simulations and experiments.

In Chapter 6, in order to elucidate the effect of static inhomogeneities on the scattering profiles, I conduct SANS measurement on the Tetra-PEG gel with systematically introducing two types of the inhomogeneities. Firstly, we prepare defect-rich networks by simply reducing primary polymer concentration, and observe the evolution of network structure by time-resolved SANS during gelation process. Secondly, we prepare Tetra-PEG gels by tuning the reaction probability, p, and soak the p-tuned gels in water to expose the inhomogeneieties. In both measurements, we observed systematical changes in the scattering profiles.On the basis of these results, we discuss the relationship between the defects of polymer network and inhomogeneities by using simple schematic pictures of polymer network.

References

[1] Flory, P. J., *Principles of Polymer Chemistry*, Cornell Univ.: Ithaca, **1953**.

[2] Stockmayer, W. H., *J. Chem. Phys.*, **1943**, 11, (2), 45-55.

[3] Gordon, M., *Proc. R. Soc. London, Ser. A*, **1962**, 268, 240.

[4] Gordon, M.; Scantlebury, G. R., *Proc. R. Soc., A*, **1966**, 292, 1380.

[5] Gordon, M.; Scantlebury, G. R., *J. Polym. Sci., Part C*, **1968**, 16, 3933.

[6] Good, I. J., *Proc. Camb. Phil. Soc.*, **1955**, 51, (1), 240.

[7] Good, I. J., *Proc. Camb. Phil. Soc.*, **1960**, 56, 367-380.

[8] J. Scanlan, *J. Polym. Sci.*, **1960**, 43, 501-507.

[9] L. C. Case, *J. Polym. Sci.*, *1960*, 45, 397-403.

[10] Miller, D. R.; C. W. Macosko, *Macromolecules*, **1976**, 9 (2), 206-211.

[11] Rubinstein, M. ; Colby, R. H., *Polymer Physics*, Oxford Univ. Press., Oxford, **2003**.

[12] de Gennes, P. G., *Scaling Concepts in Polymer Physics*, Cornell University: Ithaca, **1979**.

[13] Stauffer, D.; Aharony, A., *Introduction to percolation theory*, Taylor & Francis: 1994; Vol. 2

[14] Martin, J. E.; Wilcoxon, J.; Odinek, *J. Phys. Rev. A.*, **1991**, 43, 858-871.

[15] de Gennes, P. G., *J. Phys. Lett.*, **1979**, 40, L-197.

[16] Feng, S.; Sen, N. S., *Phys. Rev. Lett.*, **1984**, 52, (3), 216-219.

[17] Farago, O.; Kantor, Y., *EurophysicsLetter*, **2000**, 52, 413.

[18] Djabourov, M.; Leblond, J.; Papon, P., *J. Phys. (Paris)*, **1988**, 49, 319.

[19] Djabourov, M,.*Contmp. Phys.*, **1988**, 29, 273-293.

[20] Devreux, F.; Boilot, J. P.; Chaput, F.; Malier, L.; Axelos, M. A. V., *Phys. Rev. E*, **1993**, 47, 2689-2694.

[21] Tokita, M.; Hikichi, K., *Phys. Rev. A*, **1987**, 35, (10), 4329-4333.

[22] Lusignan, C. P.; Mourey, T. H.; Wilson, J. C.; Colby, R. H. *Phys. rev. E*,**1995**, 52, (6), 6271-6280.

[23] Lusignan, C. P.; Mourey, T. H.; Wilson, J. C.; Colby, R. H., *Phys. rev. E*,**1999**, 60, 5657-5669.

[24] Colby, R. H.; Gillmor, J. R.; Rubinstein, M. *Phys. rev. E*, **1993**, 48, (5), 3712-3716.

[25] Martin, J. E.; Adorf, D.; Wilcoxon, J. P., *Phys. Rev. Lett.*, **1988**, 61, 2620-2623.

[26] Adam, M.; Delsanti, M.; Durand, D., *Macromolecules*, **1985**, 18, (11), 2285-2290.

[27] Kirkpatrick, S., *Rev. Mod. Phys.*, **1973**, 45, (4), 574-588.

[28] Bernasconi, J. *Phys. Rev. B*, **1978**, 18, (5), 2185-2191.

[29] Sahimi, M.; Hughes, B. D.; Scriven, L. E.; Davis, H. T., *Phys. Rev. B*, **1983**, 28, (1), 307-311.

[30] Sahimi, M., *Rev. Mod. Phys.*, **1993**, 65, (4), 1393-1534.

[31] Meakin, P., *Phys. Rev. Lett.*, **1983**, 51, (13), 1119-1122.

[32] Ziff, R. M.; McGrady, E. D.; Meakin, P. *J. Chem. Phys.*, **1985**, 82, (11), 5269-5274.

[33] Ziff, R. M. *J. Stat. Phys.*, **1980**, 23, (2), 241-263.

[34] Horie, K.; Hiura, H.; Sawada, M., *J. Poly. Sci. A-1*, **1970**, 8, 1357-1372.

[35] Dusek, K., *Polym. Gels and Network*, **1996**, 4, 383-404.

[36] Dusek, K.; Duskova-Smrckova, M., *Prog. Polym. Sci.*, **2000**, 25, 1215-1260.

[37] Schulz, G. V., *Z. Phys. Chem. (Muenchen)*, **1956**, 8.

[38] Li, W.-H.; Hamielec, A. E.; Crowe, C. M., *Polymer*, **1989**, 30, 1513-1517.

[39] Li, W.-H.; Hamielec, A. E.; Crowe, C. M., *Polymer*, **1989**, 30, 1518-1523.

[40] Zhu, S.; Tian, Y.; Hamilec, A. E.; Eaton, D. R., *Polymer*, **1990**, 31, 154-159.

[41] Scranton, A. B.; Bowman, C. N.; Klier, J.; Peppas, N. A., *Polymer*, **1992**, 33, 1683-1689.

[42] Young, J. S.; Bowman, C. N., *Macromolecules*, **1999**, 32, 6073-6081.

[43] Anseth, K. S.; Kline, L. M.; Walker, T. A.; Anderson, K. J.; Bowman, C. N., *Macromolecules*, **1995**, 28, 2491-2499.

[44] Cook, W. D., *J. Polym. Sci. A. Polym. chem.*, **1993**, 31, 1053-1067.

[45] Berchtold, K. A.; Bowman, C. N., *RadTeck Europe99 Conference Proceedings*, **1999**, 767.

[46] Anseth, K. S.; Wang, C. M.; Bowman, C. N., *Macromolecules*, **1994**, 27, 650-655.

[47] Kloosterboer, J. G., *Adv. Polym. Sci.*, **1988**, 84, 1-61.

[48] Miyazaki, K.; Horibe, T., *J. Biomed. Mater. Res.*, **1988**, 22, (11), 1011-1022.

[49] Allen, P.; Simon, G.; Williams, D.; Williams, E., *Macromolecules*, *1989*, 22, 809-816.

[50] Cook, W. D., *Polymer*, **1992**, 33, 600-609.

[51] Simon, G.; Allen, P.; Bennett, D.; Williams, D.; Williams, E., *Macromolecules*, **1989**, 22, (2), 3555-3561.

[52] Allen, P.; Bennett, D.; Hagias, S.; Hounslow, A.; Ross, G.; Simon, G.; Williams, D.; Williams, E., *Eur. Polym. J.*, **1989**, 25, 785-789.

[53] Kloosterboer, J.; Lijten, G.; Boots, H., *Makromol. Chem., Macromol. Symp.*, **1989**, 24, 223-230.

[54] Bowman, C. N.; Peppas, N. A., *Macromolecules*, **1991**, 24, 1914-1920.

[55] Mendes, E.; Girard, B.; Picot, C.; Buzier, M.; Boue, F.; Bastide, J., *Macromolecules*, **1993**, 26, 6873-6877.

[56] Jong, L.; Stein, R. S., *Macromolecules*, **1991**, 24, (9), 2323-2329.

[57] Sullivan, J. L.; Mark, J. E.; Hampton, P. G.; Cohen, R. E., *J. Chem. Phys.*, **1978**, 68, 2010-2012.

[58] Mark, J. E.; Rahalkar, R. R.; Sullivan, J. L., *J. Chem. Phys.*, **1979**, 70, 1794-1797.

[59] Llorente, M. A.; Mark, J. E., *J. Chem. Phys.*, **1979**, 71, 682-689.

[60] Panyukov, S.; Rabin, Y., *Macromolecules*, **1996**, 29, 7960-7975.

[61] Bastide, J.; Leibler, L., *Macromolecules* **1988**, 21, 2647-2649.

[62] Sakai, T.; Matsunaga, T.; Yamamoto, Y.; Ito, C.; Yoshida, R.; Suzuki, S.; Sasaki, N.; Shibayama M.; Chung, U. I., *Macromolecules*, **2008**, 41, 5379-5384.

[63] Matsunaga, T.; Sakai, T.; Akagi, Y.; Chung, U. I.; Shibayama, M., *Macromolecules*, **2009**, 42, (16), 6245-6252.

[64] Akagi, Y.; Katashima, T.; Fujii, K.; Matsunaga, T.; Chung, U. I.; Shibayama, M.; Sakai, T.; *Macromolecules*, **2011**, 44, 5817-5821.

[65] Akagi, Y. ; Gong, J. P.; Chung U. I.; Sakai, T. ,*Macromolecules*, **2013**, 46,1035-1040.

[66] Akagi, Y.; Katashima, T.; Sakurai, H.; Chung, U. I.; Sakai, T., *RSC Advavces*, **2013**, 3, 13251-13258.

[67] Katashima, T.; Urayama, K.; Chung, U.-I.; Sakai, T., *Soft matter*, **2012**, 8, 8217-8222.

[68] Sakai, T.; Kurakazu, M.; Akagi, Y.; Shibayama, M.; Chung, U., *Soft Matter*, **2012**, 8, (9), 2730-2736.

[69] Li, X.; Tsutsui, Y.; Matsunaga, T.; Shibayama, M.; Chung, U.; Sakai, T., *Macromolecules*, **2011**, 44, 3567-3571.

[70] Sakai, T.; Akagi, Y.; Matsunaga, T.; Kurakazu, M.; Chung, U.; Shibayama, M., *Macromol. Rapid Commun.*, **2010**, 31, (22), 1954-1959.

Chapter 2

Temperature dependence of gelation kinetics of Tetra-arm polymers

2.1 Introduction

In production of polymeric materials, gelation or cross-linking is one of the fundamental key reactions. A variety of commercial products such as rubbers, gels, paints and adhesives are made by way of gelation threshold, i.e., the onset of formation of infinitely-large clusters. In addition, as gelation or cross-linking is different from ordinary reaction kinetics, it has dramatic changes in macroscopic properties, such as the divergence of viscosity, the sol-gel transition, and the increment of the elastic modulus, and so have attracted scientific interests until now. Hence, the understanding of network formation in terms of structure and kinetics is of particular importance not only from basic science but also from industrial applications.

As mentioned in Introduction, when the mean-field approximation is applied to the reactivity of terminal functional group, the reaction rate equation for cross-linking reaction is described as a simple reaction rate equation (1.2). However, real experiments are more complicated because of the (i)the substitution effect, (ii)the steric hinderance, and (iii)the diffusion motion of clusters. Thus, investigation and knowledge on the gelation reaction has been still limited at the present stage.

In order to avoid these difficulties, we focused on the polycondensation kinetics of Tetra-PEG gel, which is fabricated from AB-type cross-end coupling of two mutually reactive tetra-arm polymers of the same size.[1–9] Each tetra-arm polymer has four amine groups (TAPEG) or activated ester groups (TNPEG). Tetra-PEG gel system is different from conventional crosslinking systems in the way that the crosslinking point is preformed in the precursor; all of the reaction occurs between the arm-ends of precursors. Therefore, the substitution effect and the steric hinderance are expected to be insignificant on Tetra-PEG gel system. The polycondensation process of Tetra-PEG gel was investigated in the viewpoint of the chemical reaction kinetics between mutually reactive terminal groups of Tetra-PEGs by using FT-IR spectroscopy. We, for the first time, report the rate constant, k and activation thermodynamic quantities ($\Delta G^{\ddagger}$,$\Delta H^{\ddagger}$ and $\Delta S^{\ddagger}$) for the gelling polycondensation system through Tetra-PEG gel.

2.2 Experiment

2.2.1 Materials

Tetra-amine-terminated PEG (TAPEG) and tetra-NHS-glutarate-terminated PEG (TNPEG) were prepared from tetra-hydroxyl-terminated PEG (THPEG) having equal arm lengths. The details of TAPEG and TNPEG preparation are reported elsewhere.[9] The molecular weights (M_w) of TAPEG and TNPEG were matched to be 10 kg/mol. Here NHS represents N-hydroxysuccinimide. The activity of the functional groups was estimated using NMR. TNPEG ^{1}H NMR ($CDCl_3$, δ): 2.07 (m, 2H, CH_2 CH_2 CH_2), 2.49 (t, 2H, CH_2 CH_2 CH_2), 2.72 (t, 2H, CH_2 CH_2 CH_2), 2.83 (s, 4H, NCO CH_2 CH_2CON), 3.4 (s, 2H, CH_2O), 3.63(m, (4 m - 2)H, (CH_2 CH_2O)m-1 CH_2), 4.24 (t, 2H, CH_2CH_2O). TAPEG ^{1}H NMR ($CDCl_2$, δ): 1.91 (br, 2H, NH_2), 3.18 (t, 2H, CH_2 CH_2), 3.42 (s, 2H, CH_2O), 3.63 (m, (4 m - 2)H, (CH_2 CH_2O)m - 1CH_2).

2.2.2 IR Spectroscopy

IR spectra were measured at a resolution of 2 cm^{-1} with a coaddition of 128 scans using a Nicolet 6700 Fourier-transform IR spectrometer equipped with a liquid-nitrogen-cooled MCT detector. The attenuated total reflection (ATR) technique was employed to obtain IR spectra of the polymer solution. The solution was filled in an ATR cell, which was made of a horizontal ZnSe crystal (R.I. 2.403) with an incident angle of 45°. The ATR cell was kept at 10-50 °C with an accuracy of 0.1 °C throughout the entire experiment by using a homemade thermoelectric device. The ATR cell was sealed by a toggle-clamp-type cover to prevent the evaporation of solvent.

The reaction rate for degradation of TNPEG was estimated by ATR-IR spectrometry. A constant amount of TNPEG (240 mg) was dissolved in 3.0 mL of 0.2 M phosphate D-buffer (pH7.0) at 10-50 °C and the solutions were added into an ATR cell. The time course of the degradation was investigated by ATR-IR spectra. In gelation system, constant amounts of TAPEG and TNPEG (240 mg) were dissolved in 3 mL of phosphate D-buffer solution (PB; 0.2 M, pH 7). The two solutions thus obtained were mixed in a 50 mL Falcon tube for 30 s at 10-40 °C, and poured into the ATR cell.

IR spectra obtained were deconvoluted to extract single bands. A single band is assumed to be represented as a pseudo-Voigt function, $f_{\mathrm{V}}(\nu) = \gamma f_{\mathrm{L}}(\nu) + (1 - \Gamma) f_{\mathrm{G}}(\nu)$, where $f_{\mathrm{L}}(\nu)$ and $f_{\mathrm{G}}(\nu)$ stand for Lorentzian and Gaussian components, respectively, and the parameter γ $(0 < \gamma < 1)$ is the Lorentzian component. A nonlinear least-squares curve fitting procedure was employed for the analyses. The integrated intensity A of a single band is evaluated according to $A = \gamma A_{\mathrm{L}} + (1 - \gamma) A_{\mathrm{G}}$, where A_{L} and A_{G} denote integrated intensities of the Lorentzian and Gaussian components, respectively. Total Intensity $A_{\mathrm{calc}}(\nu)$ calculated were compared with observed one $A_{\mathrm{obs}}(\nu)$ in terms of the Hamilton R factor, $R = (\Sigma(A_{\mathrm{obs}}(\nu) - A_{\mathrm{calc}}(\nu))^2 / \Sigma A_{\mathrm{calc}}(\nu)^2)^{1/2}$. Observed intensities were indeed reproduced with $R < 0.01$.

2.2.3 DFT calculations

Evaluation of the full geometry optimization followed by normal frequency analyses was carried out on the basis of the density functional theory taking into account an electron correlation effect with Becke's three parameter and Lee-Yang-Parr correlation function (B3LYP), coupled with 6-311+G(d,p) basis set.[10,11] All calculations were carried out using the Gaussian 03 program package.[12] The C_2H_5-CO-NHS, NHS ion and C_2H_5COO ion were examined as a model molecule for terminal NHS ester of TNPEG, dissociated NHS and hydrolyzed terminal end of TNPEG in this gelation system, i.e., main PEG chain within Tetra-PEG is replaced by ethyl group to calculate easily. In this calculation, their molecules were hydrated stepwise from mono- to tri-hydrated ones to obtain the optimized structure and theoretical IR band in all the molecules. Among them, the theoretical bands for the hydrated molecules were well consistent with the experimental IR bands. Typical optimized structures are shown in Figure 2.1.

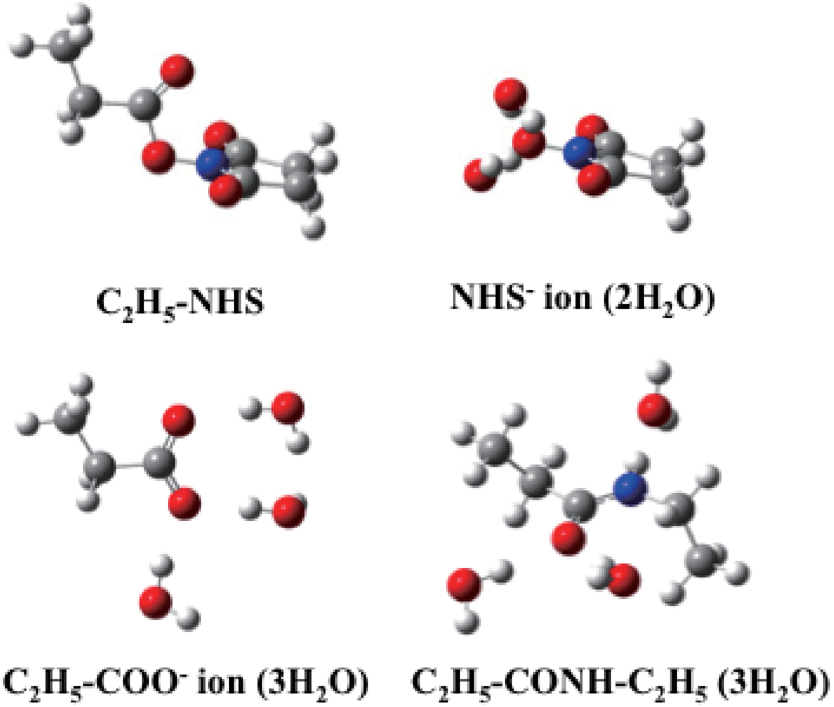

C_2H_5-NHS

NHS$^-$ ion ($2H_2O$)

C_2H_5-COO$^-$ ion ($3H_2O$)

C_2H_5-CONH-C_2H_5 ($3H_2O$)

Figure 2.1: Optimized geometries of the hydrated model molecules obtained from DFT calculations.

2.3 Results and Discussion

2.3.1 Reaction kinetics of Tetra-PEG gel

The main reaction of Tetra-PEG gel system is aminolysis reaction between the amine group within TAPEG and activated ester (N-hydroxysuccinimidyl (NHS) ester) group within TNPEG.

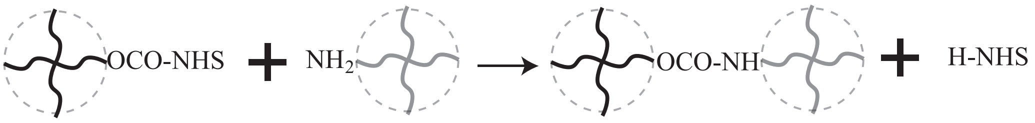

(2.1)

Here two points should be noted. First, the activated ester group within TNPEG gradually dissociates in aqueous solution due to hydrolysis reaction as follows,

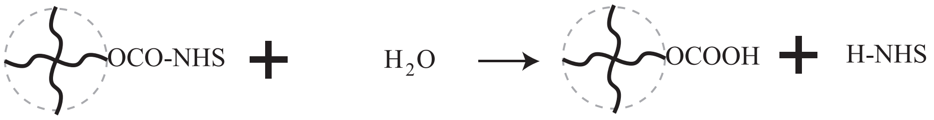

(2.2)

In addition, the terminal NH_2 group within TAPEG coexists with the protonated NH_3^+ in equilibrium, as follows.

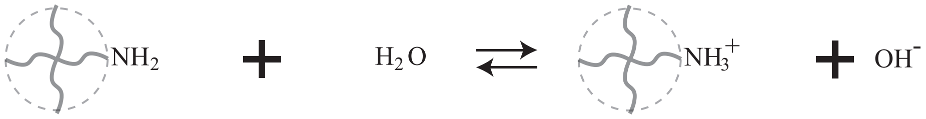

(2.3)

$$K_{\mathrm{a}} = \frac{[-\mathrm{NH_2}]\,[\mathrm{H^+}]}{\left[-\mathrm{NH_3^+}\right]} \tag{2.4}$$

$$[-\mathrm{NH_2}]_{\mathrm{total}} = [-\mathrm{NH_2}] + \left[-\mathrm{NH_3^+}\right] \tag{2.5}$$

where $[\text{-NH}_2]_{\mathrm{total}}$ corresponds to the total concentration of amine group within TAPEG. Only the un-ionized amine group reacts with the activated ester group because the ionized amine group does not have an unshared electron pair. Therefore, the rate equation for the gelation is described as follows.

$$-\frac{d\,[-\mathrm{NH_2}]_{\mathrm{total}}}{dt} = k_{\mathrm{gel}}\,[-\mathrm{NH_2}]\,[-\mathrm{NHS}] = k_{\mathrm{gel}} f\,[-\mathrm{NH_2}]_{\mathrm{total}}\,[-\mathrm{NHS}] \tag{2.6}$$

$$-\frac{d\,[-\mathrm{NH_2}]_{\mathrm{total}}}{dt} = k_{\mathrm{gel}} f\,[-\mathrm{NH_2}]_{\mathrm{total}}\,[-\mathrm{NHS}] + k_{\mathrm{deg}}\,[-\mathrm{NHS}] \tag{2.7}$$

where k_{gel} and f denote the rate constant for the gelation and the fraction of un-ionized amine to total amine, i.e., $f = \frac{[-\mathrm{NH_2}]}{[-\mathrm{NH_2}]_{\mathrm{total}}} = \frac{K_\mathrm{a}}{K_\mathrm{a} + [H^+]}$, respectively. Here f is determined by K_a in equation (2.4) and pH. The pK_a in equation (2.4) was separately determined by potentiometric titration for TAPEG solution and the value was estimated to be 9.27 from the potentiometric titration in our previous work.[3]

On the other hand, though pH was almost controlled by using phosphate buffer, pH was slightly varied along with $[\text{-NH}_2]_{\mathrm{total}}$ in solution. In this work, the values of pH were experimentally determined by pH measurement. Figure 2.2 shows the fraction of un-ionized amine as a function of total amine concentration for Tetra-PEG-NH$_2$ of $M_w = 10$, 20, and 40 kg/mol and for LinearPEG-NH$_2$ of $M_w = 5$ kg/mol. In this study, we expressed the relationship between the fraction of un-ionized amine and total amine concentration with a polynominal equation. The polynominal equation was determined from the fitting. The fitting results for Linear-PEG is

$$\begin{aligned} f &= 2.73 \times 10^{-3} + 2.8428 \times 10^{-2} \times [-\mathrm{NH_2}]_{\mathrm{total}} \\ &\quad +1.5154 \times 10^{-1} \times [-\mathrm{NH_2}]^2_{\mathrm{total}} - 8.2997 \times [-\mathrm{NH_2}]^3_{\mathrm{total}} \quad , \end{aligned} \tag{2.8}$$

that for Tetra-PEG of $M_w = 10$ kg/mol is

$$\begin{aligned} f &= 2.2484 \times 10^{-3} + 3.0418 \times 10^{-2} \times [-\mathrm{NH_2}]_{\mathrm{total}} \\ &\quad +7.5455 \times 10^{-2} \times [-\mathrm{NH_2}]^2_{\mathrm{total}} - 1.9775 \times [-\mathrm{NH_2}]^3_{\mathrm{total}} \quad , \end{aligned} \tag{2.9}$$

that for Tetra-PEG of $M_w = 20$ kg/mol is

$$\begin{aligned} f &= 1.9613 \times 10^{-3} + 2.8186 \times 10^{-2} \times [-\mathrm{NH_2}]_{\mathrm{total}} \\ &\quad +4.7555 \times 10^{-2} \times [-\mathrm{NH_2}]^2_{\mathrm{total}} + 4.8714 \times [-\mathrm{NH_2}]^3_{\mathrm{total}} \quad , \end{aligned} \tag{2.10}$$

and that for Tetra-PEG of $M_w = 40$ kg/mol is

$$\begin{aligned} f &= 1.9069 \times 10^{-3} + 2.5851 \times 10^{-2} \times [-\mathrm{NH_2}]_{\mathrm{total}} \\ &\quad +9.0594 \times 10^{-2} \times [-\mathrm{NH_2}]^2_{\mathrm{total}} + 46.1338 \times [-\mathrm{NH_2}]^3_{\mathrm{total}} \quad , \end{aligned} \tag{2.11}$$

which will be used for the fitting analysis of rate constants.

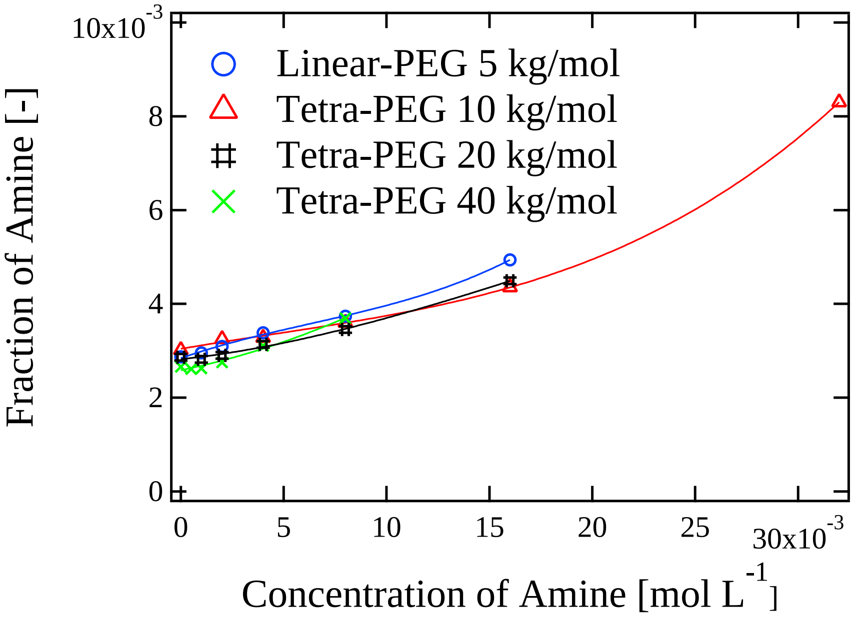

Figure 2.2: The fraction of un-ionized amine as a function of total amine concentration.

2.3.2 Degradation Kinetics of TNPEG in Solution

In order to estimate the rate constant for gelation in Tetra-PEG system, the rate for the degradation of TNPEG was evaluated by IR-ATR measurements. Figure 2.3 shows IR spectra in the range of 1550 -1850 cm^{-1} obtained for TNPEG solution (C = 80 mg/ml) at various t. In this wavenumber range, IR bands originated from TNPEG or dissociated NHS were seriously overlapped with an intense and wide band from water. Therefore, IR spectra examined here were subtracted by those for aqueous buffer solution measured separately to extract TNPEG and dissociated NHS components as shown in Figure 2.3. As seen in Figure 2.3, the peak intensities at 1728, 1778 and 1812 cm^{-1} decreased with increasing t and those at 1555, 1646, 1670 and 1704 cm^{-1} increased. It was found that an isosbestic point is clearly seen at 1720 cm^{-1}, implying that dissociation reaction quantitatively occurs in this system.

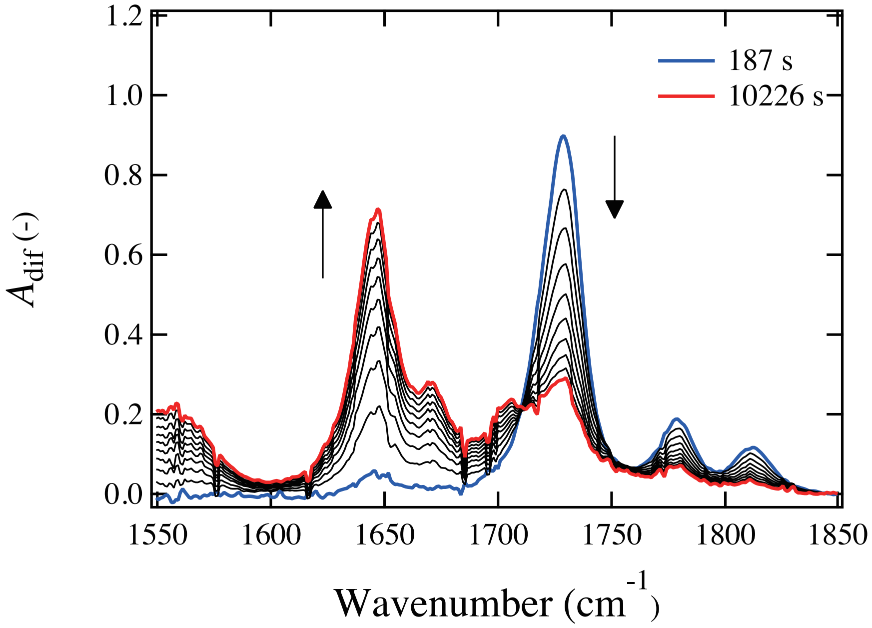

Figure 2.3: Time dependence of IR spectra for TNPEG solution, C = 80 mg/mL, containing 0.2 M phosphate D-buffer (pH 7.0) at 30 °C.

Figure 2.4 shows typical IR bands of TNPEG solution after 1205 s, together with theoretical IR bands for the hydrated C_2H_5-CONHS, NHS ion and C_2H_5COO ion as a model molecules calculated by DFT calculations. The theoretical IR bands of a given molecule are predicted by full geometry optimizations followed by normal frequency analyses, and the optimized structures are shown in Figure 2.1. On the basis of theoretical IR bands, the observed IR spectrum can be satisfactorily deconvoluted into seven bands. Three bands at 1728, 1778 and 1812 cm^{-1} are assigned to the terminal NHS group within TNPEG and three bands at 1646, 1670 and 1704 cm^{-1} to dissociated NHS ion. Weak and broad band at 1555 cm^{-1} is ascribed to the terminal ionized carboxyl group. With regard to the dissociated NHS and TNPEG, we examined to calculate theoretical bands for neutral NHS and TNPEG-COOH. However, their band positions did not represent the observed ones, and we thus concluded that NHS and TNPEG after the degradation exist as ionic species.

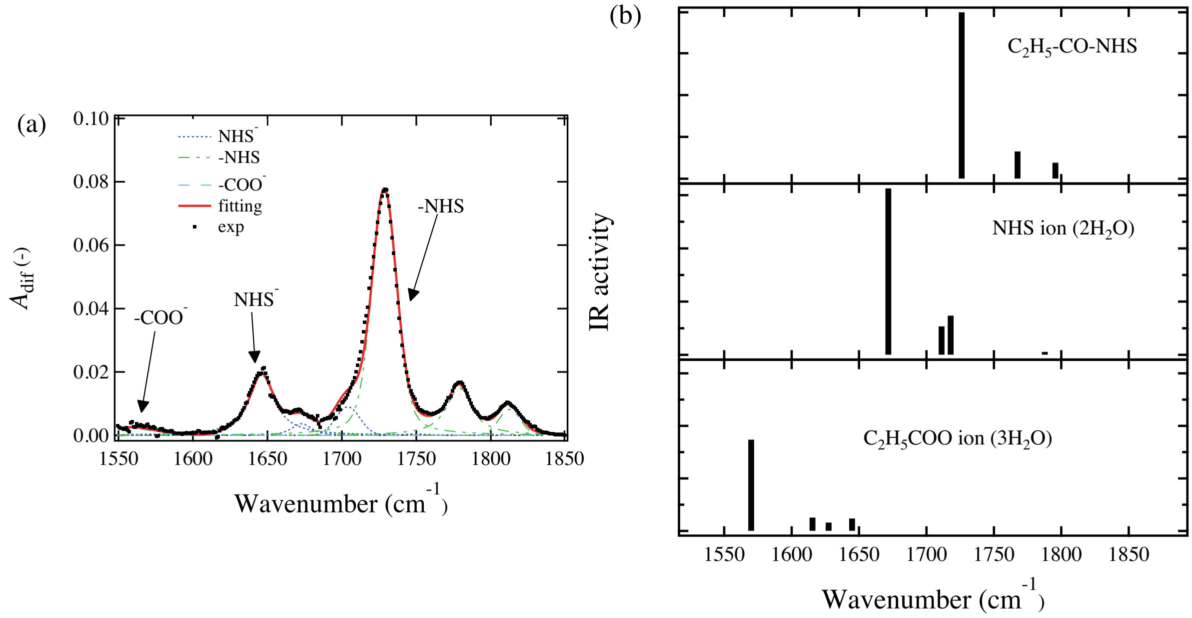

Figure 2.4: (a) Typical deconvoluted IR bands for TNPEG solution, C = 80 mg/mL at 1205 s (30 °C). Dotted black and red lines show the observed and calculated IR spectra. Blue, green, and light blue lines correspond to the dissociated NHS, terminal NHS, and ionized carboxylic acid components, respectively. (b) Theoretical IR bands for hydrated C_2H_5-NHS (neutral), NHS (ion), and $C_2H_5COO^-$ (ion)groups as a simple model, obtained from DFT calculations.

The kinetic trace of [NHS$^-$] at various temperatures, i.e., dissociated NHS ion concentration based on the integrated IR band at 1646 cm^{-1} assigned to stretching ν(C-O) vibration plotted against t, is shown in Figure 2.5(a). Figure 2.5 (b) shows ln([-NHS]/[-NHS]$_0$) vs t, where [-NHS]$_0$ denotes the initial concentration of terminal NHS. As can be seen in these figures, the degradation rate became fast with increasing temperature. The apparent rate constant, k_{deg} was estimated by least square-fit analysis on the basis of the following rate equation; $-d[-\mathrm{NHS}]/dt = d[\mathrm{NHS}^{-}]/dt = k_{\mathrm{deg}}[-\mathrm{NHS}]$. The observed variation (open symbols) was well represented with the fitting curve (solid line). Furthermore, Figure 2.5 (b) clearly indicates the linear relationship between ln([-NHS]/[-NHS]$_0$) and time. These results suggest that the TNPEG in solution dissociates under a pseudo first-order kinetics reaction to give NHS and TNPEG-COO ions. By assuming a second-order reaction kinetics including [-NHS] and [OH$^-$] terms to this dissociation, i.e., we can obtain k'_{deg} independent of [H$^+$] and/or pH. The values were estimated to be k'_{deg} =427, 723, 2060, 3010 and 4730 mol dm^{-3} s^{-1} at 283, 293, 303, 313 and 323 K, respectively. The rate constants obtained here are almost the same as those reported for the corresponding reactions of anisoyl-NHS in the literature, which supports the validity of our experiments.[13] These values will be used as fitting parameters in the following section. The estimated rate constants plotted against reciprocal temperature give the activation enthalpy and entropy according to the Eyring equation for the theory of transition state. The $\ln(k_{\mathrm{deg}}T^{-1})$ vs. T^{-1} plot is shown in Figure 2.6, and the activation $\Delta H^{\ddagger}$ and $\Delta S^{\ddagger}$ are obtained from the slope and intercept of the plot on the basis of the equation $\ln(k_{\mathrm{deg}}T^{-1}) = -\Delta H^{\ddagger}(RT)^{-1} + \Delta S^{\ddagger}R^{-1} + \ln(\kappa k_{\mathrm{B}}h^{-1})$. The $\Delta H^{\ddagger}$, $T\Delta S^{\ddagger}$ and $\Delta G^{\ddagger}$ values were estimated to be 47(4) kJ mol^{-1}, -9(5) kJ mol^{-1} (at T = 298 K) and 56(9) kJ mol^{-1}, respectively. The activation energy are consistent with the corresponding energies for the hydrolysis reaction of 11,11'-dithiobis (N-hydroxysuccinimidylundecanoate) in self-assembled monolayers on Gold, which also supports the validity of our experiments.[14] The estimated activation entropy $\Delta S^{\ddagger} \leq 0$ indicates that the TNPEG dose not completely dissociate to remain TNPEG-CO$\cdots$NHS bond at the transition state on the hydrolysis reaction.

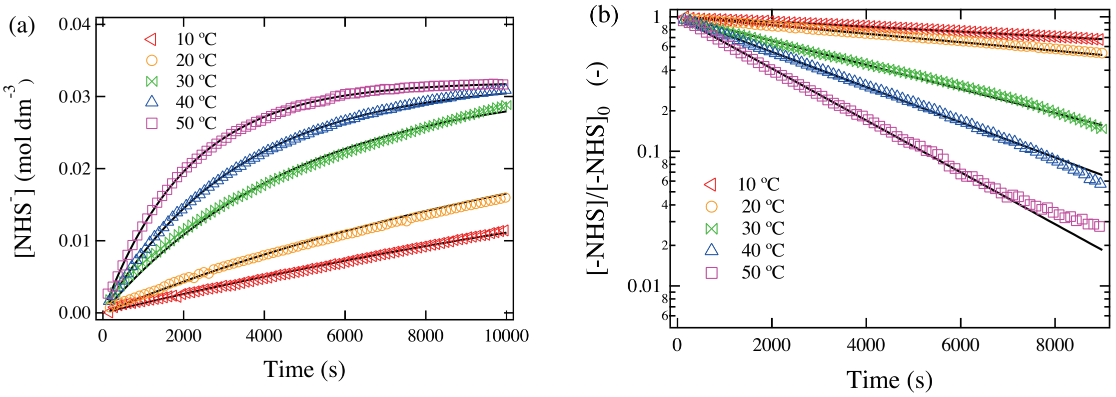

Figure 2.5: (a) Kinetic trace obtained for the degradation of TNPEG at 1646 cm^{-1} (C — O stretching vibration) as a function of t. the concentration of the dissociated NHS is defined as $C_t = (A_t/A_\infty)C_\infty$ where C_t, C_∞, A_t, and A_∞ denote the concentration of dissociated NHS at time t, that at infinitive time, the peak intensity of 1646 cm^{-1} band at t, and that at infinitive time, respectively. (b) Pseudo-first-order plots of the degradation of TNPEG.

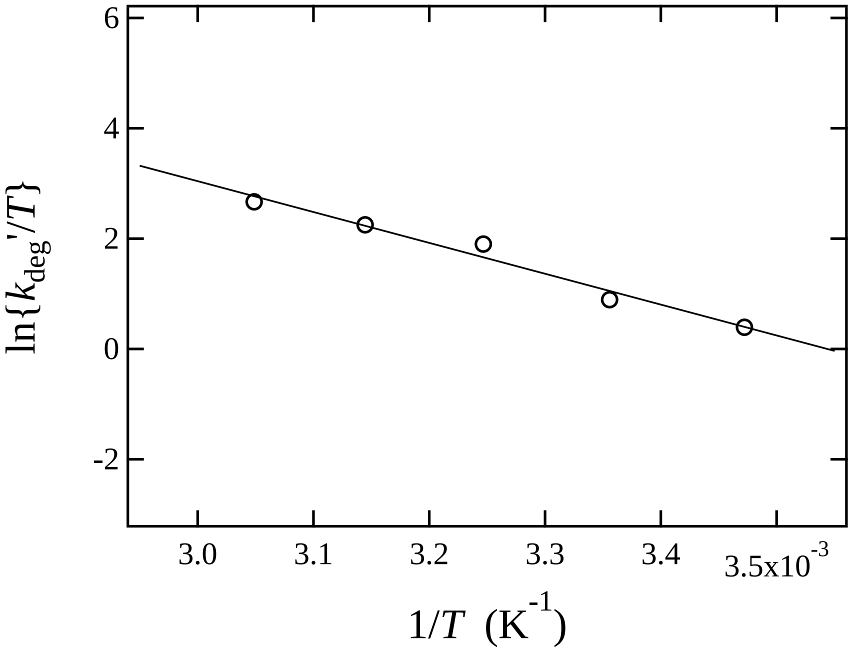

Figure 2.6: The degradation rate constant plotted against temperature as the form of Eyring plot.

2.3.3 Polycondensation kinetics and reaction mechanism of Tetra-PEG gel

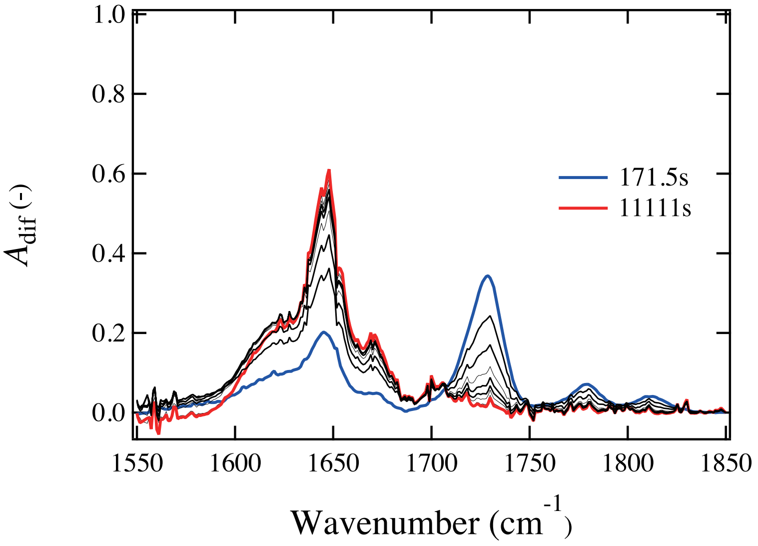

Figure 2.7: Time dependence of IR spectra for the gelation of Tetra-PEG macromers (TNPEG: 80 mg/mL; TAPEG: 80 mg/mL) in solution containing 0.2 M phosphate D-buffer (pH 7.0) at 20 °C.

Figure 2.7 shows the time dependence of IR spectra for Tetra-PEG components at 20°C obtained by subtracting those for buffer solutions. The peak intensities at 1728, 1778 and 1812 cm^{-1} decreased and those at 1614, 1646, 1670 and 1704 cm^{-1} increased with progressing reaction. The IR spectra showed an isosbestic point at around 1720 cm^{-1}, implying that the polycondensation process in Tetra-PEG gel system is successfully observed by our IR technique examined here. Figure 2.8 shows a typical IR spectrum observed at 1400 s, together with theoretical IR bands calculated by DFT calculations. According to theoretical IR bands calculated for the hydrated three simple molecules as a model of terminal groups of Tetra-PEGs, the IR spectrum can be deconvoluted into eight bands, i.e., three bands at 1728, 1778 and 1812 cm^{-1} originated from C_2H_5CO-NHS, three at 1646, 1670 and 1704 cm^{-1} from dissociated NHS ion and 1624 cm^{-1} band from a newly formed amide bond. It is found that there is no peak at 1555 cm^{-1} assigned to the ionized carbonyl group, which is clearly seen in Figure 2.3. This indicates that the formation of amide bond (-CONH-) on the polycondensation successfully proceeds, while hydration of terminal NHS group does not proceed practically.

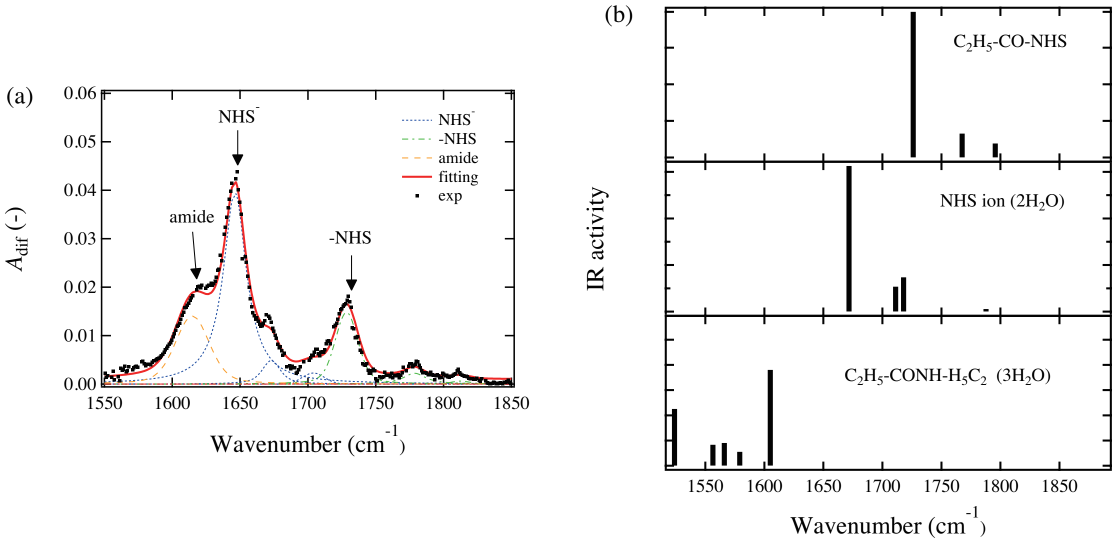

Figure 2.8: (a)Typical deconvoluted IR bands on a gelation process, C = 80 mg/mL at 1400 s (20 °C). Dotted black and red lines show the observed and calculated IR spectra. Blue, green, and orange lines correspond to the dissociated NHS, terminal NHS, and amide bond components, respectively. (b) Theoretical IR bands for hydrated $C_2H_5 - \mathrm{NHS}$ (neutral), NHS (ion), and $C_2H_5COO^-$ (ion) groups as a simple model, obtained from DFT calculations.

Figure 2.9 (a) and (b) show the kinetic traces for the dissociated NHS ion, [NHS$^-$], and second-order plots at various temperatures, respectively, based on the integrated IR intensities of the stretching ν(C-O, NHS) band. It was found that the gelation rate increases with increasing temperature. The fit results using eqs (2.6) and (2.7) were also shown in Figure 2.9 (a). Here, we set k_{deg} as a fixed parameter obtained by the degradation analysis. The fit worked well from the initiation to nearly completion of reaction. Moreover, the second-order plot gives a straight line passing through the origin in Figure 2.9 (b). It should be noted that the gelation occurred at 1187, 496, 194 and 100 s after initiation at 283, 293, 303 and 313 K, respectively. These results suggest that this polycondensation reaction obeys a simple second-order kinetics from the initiation to end regardless of gelation threshold. This reason is suspected to be that the polycondensation kinetics of Tetra-PEG gel is not affected by the substitution effect and steric hinderance.

Figure 2.10 shows the rate constant, k_{gel} plotted against reciprocal temperature as a form of Eyring plot. It is proved that Eyring plot for gelation reaction can be made and this result suggests that k_{gel} is thermodynamically meaningful. The activation enthalpy $\Delta H^{\ddagger}$, entropy $T\Delta S^{\ddagger}$ and Gibbs free energy $\Delta G^{\ddagger}$obtained from the slope

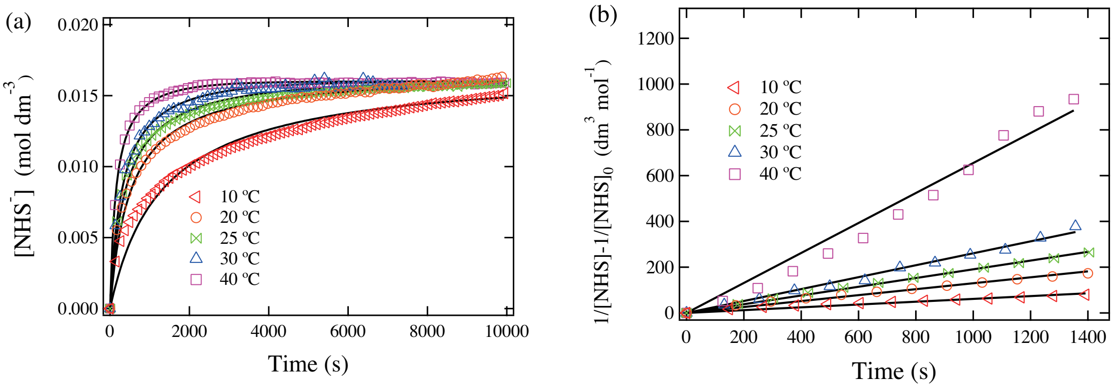

Figure 2.9: (a) Kinetic trace obtained for the gelation at 1646 cm^{-1} (C — O stretching vibration of dissociated NHS) as a function of t. (b)Pseudo-second-order plots of the gelation of Tetra-PEG gel.

and intercept in this figure were estimated to be 49(3), -13(3) kJ mol^{-1} (at $T = 298$ K) and 63(6) kJ mol^{-1}, respectively. Though small, the negative entropy implies the amide bond (NH-CO) between TNPEG and TAPEG is formed as the intermediate product on the polycondensation process, i.e., an associative mechanism operates at the transition state. The activation thermodynamic quantities involve a solvation effect at the transition state. However, it is difficult to discuss the hydration effect at the present stage. We need to accumulate the experimental activation energy in various solvent systems, which is now going on for alcohols or room-temperature ionic liquids.

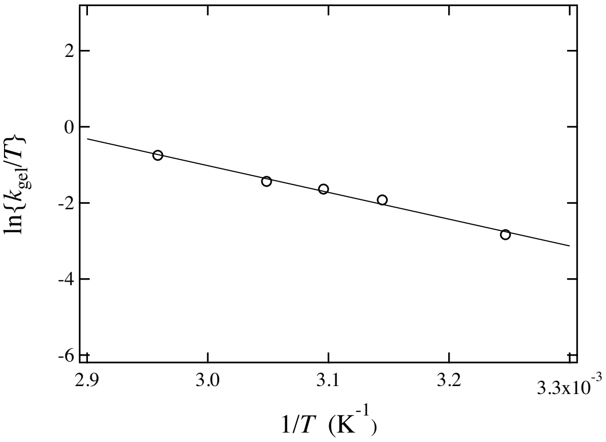

Figure 2.10: $\ln(k_{\mathrm{gel}}/T)$ plotted against $1/T$ as a form of Eyring plot.

2.4 Conclusion

The polycondensation reaction forming Tetra-PEG gel was investigated by ATR-IR spectroscopy in the viewpoint of reaction kinetics. We showed here that (1) the gelation kinetics of Tetra-PEG gel can be simply treated as a chemical reaction between mutually reactive end-groups in solution; (2) the gelation undergoes as a simple second-order reaction from beginning to end regardless of gelation threshold; (3) the gelation mechanism was predicted from the thermodynamic enthalpy and entropy at the transition state estimated by temperature dependence of rate constants. The reason of smooth second-order kinetics is suspected to be that the mean-field approximation can be applied to the reactivity of terminal groups on Tetra-PEGs, i.e. the reactivity of terminal groups on Tetra-PEGs is not affected by the steric hinderance, substitution effet, and gelation threshold, contributing to the homogeneous network structure of Tetra-PEG gel.

References

[1] Akagi, Y.; Katashima, T.; Fujii, K.; Matsunaga, T.; Shibayama, M.; Chung, U.; Sakai, T., *Macromolecules*, **2011**, 44, 5817-5821.

[2] Akagi, Y.; Matsunaga, T.; Shibayama, M.; Chung, U.; Sakai, T., *Macromolecules*, **2010**, 43, 488-493.

[3] Kurakazu, M.; Katashima, T.; Chijiishi, M.; Nishi, N.; Akagi, Y.; Matsunaga, T.; Shibayama, M.; Chung, U.; Sakai, T., *Macromolecules*, **2010**, 43, 3935-3940.

[4] Li, X.; Tsutsui, Y.; Matsunaga, T.; Shibayama, M.; Chung, U.; Sakai, T., *Macromolecules* **2011**, 44, 3567-3571.

[5] Matsunaga, T.; Asai, H.; Akagi, Y.; Sakai, T.; Chung, U.; Shibayama, M., *Macromolecules*, **2011**, 44, 1203-1210.

[6] Matsunaga, T.; Sakai, T.; Akagi, Y.; Chung, U.; Shibayama, M., *Macromolecules*, **2009**, 42, 1344-1351.

[7] Matsunaga, T.; Sakai, T.; Akagi, Y.; Chung, U.; Shibayama, M., *Macromolecules*, **2009**, 42, 6245-6252.

[8] Sakai, T.; Matsunaga, T.; Akagi, Y.; Kurakazu, M.; Chung, U.; Shibayama, M., *Macromol.RapidCommun.*, **2010**, 31, 1954-1959.

[9] Sakai, T.; Matsunaga, T.; Yamamoto, Y.; Ito, C.; Yoshida, R.; Suzuki, S.; Sasaki, N.; Shibayama, M.; Chung, U., *Macromoleules*, **2008**, 41, 5379-5384.

[10] Becke, A. D., *J.Chem.Phys.* **1993**, 98, 5648.

[11] Lee, K. Y.; Mooney, D., *J.Chem.Rev.*, **2001**, 101, 1869.

[12] Frisch, M. J.; Trucks, G. W.; Schlegel, H. B.; Scuseria, G. E.;Robb, M. A.; Cheeseman, J. R.; Montgomery, J., J. A.; Vreven, T.; Kudin, K. N.; Burant, J. C.; Millam, J. M.; Iyengar, S. S.; Tomasi, J.; Barone, V.; Mennucci, B.; Cossi, M.; Scalmani, G.; Rega, N.; Petersson, G. A.; Nakatsuji, H.; Hada, M.; Ehara, M.; Toyota, K.; Fukuda, R.; Hasegawa, J.; Ishida, M.; Nakajima, T.; Honda, Y.; Kitao, O.; Nakai, H.; Klene, M.; Li, X.; Knox, J. E.; Hratchian, H. P.; Cross, J. B.; Adamo, C.; Jaramillo, J.; Gomperts, R.; Stratmann, R. E.; Yazyev, O.; Austin, A. J.; Cammi, R.; Pomelli, C.; Ochterski, J. W.; Ayala, P. Y.; Morokuma, K.; Voth, G. A.; Salvador, P.; Dannenberg, J. J.; Zakrzewski, V. G.; Dapprich, S.; Daniels, A. D.; Strain, M. C.; Farkas, O.; Malick, D. K.; Rabuck, A. D.; Raghavachari, K.; Foresman, J. B.; Ortiz, J. V.; Cui, Q.; Baboul, A. G.; Clifford, S.; Cioslowski, J.; Stefanov, B. B.; Liu, G.; Liashenko, A.; Piskorz, P.; Komaromi, I.; Martin, R. L.; Fox, D. J.; Keith, T.; Al-Laham, M. A.; Peng, C. Y.; Nanayakkara, A.; Challacombe, M.; Gill, P. M. W.; Johnson, B.; Chen, W.; Wong, M. W.; Gonzalez, C.; Pople, J. A. Gaussian 03, Rev. B.04; Gaussian, Inc.: Pittsburgh, PA, 2003.

[13] Cline, G. W.; Hanna, S. B. J., *Org.Chem.*, **1988**, 53, 3583-3586.

[14] Schonherr, H.; Feng, C.; Shovsky, A., *Langmuir*, **2003**, 19, 10843-10851.

Chapter 3

Gelation mechanism of Tetra-arm polymers

3.1 Introduction

In Chapter 2, we pointed out that the gelation of Tetra-PEG undergoes as a simple second-order reaction and the estimated rate constant, k_{gel} shows a linear relationship against reciprocal temperature. This indicates that the reactivity of terminal groups on Tetra-PEGs is not affected by the steric hindrance and substitution effect as mentioned above. Thus, the gelation kinetics of Tetra-PEG gel allows us to be one of models of the cross-linking kinetics.

However, there still remains an unsolved problem in Chapter 2. In general, the reaction rate changes during the gelation process because cluster grows and mobility of cluster changes. According to the previous work of kinetics of cross-linking photopolymerizations,[1–10] center-of-mass diffusion is dramatically suppressed because the large clusters become entangled or crosslinked in the network. Thus, the cross-linking kinetics is generally diffusion limited and the reaction rate constants decrease as the reaction proceeds. However, such effects cannot be seen in the gelation kinetics of Tetra-PEG gels and the reaction rate is constant from beginning to end,[11] the reason of which is a main theme in this study.

The previous study on the kinetics of free radical polymerization with crosslinking showed that the reaction rate of the diffusion-limited cross-linking is affected by cross-linker concentration[3–7] and chain length of monomer,[2,8,9] functionality of monomer.[10] Then, these studies are compared to free radical polymerization without crosslinking. Hence, in this study, we extend our study to volume fraction of polymer (ϕ) and primary molecular weight (M_w) dependences of the gelation kinetics investigated by ATR-IR and UV spectroscopy. Furthermore, we also examined the linear PEG system to compare with the result of Tetra-PEG system. From these experiments, we discuss the reason that the reaction undergoes as a simple second-order reaction from beginning to end and that the gelation kinetics proceeds successfully to form Tetra-PEG gel with high mechanical strength and toughness.

3.2 Experimental Section

3.2.1 Materials

Tetraamine-terminated PEG (Tetra-PEG-NH_2) and tetra-NHS-terminated PEG (Tetra-PEG-NHS) were prepared from tetrahydroxyl-terminated PEG (Tetra-PEG $-$ OH) having equal arm lengths. The details of TAPEG and TNPEG preparation are reported elsewhere.[11] Here, -NHS stands for *N*-hydroxysuccinimide. The molecular weights of Tetra-PEG-NH_2 and Tetra-PEG-NHS were matched to each other (M_w = 10, 20, and 40 kg/mol). Monofunctional amine linear PEG (LinearPEG-NH_2) and NHS linear PEG (Linear-PEG-NHS) were purchased from Nippon Oil and Fat Co.. The molecular weights of LinearPEG-NH_2 and Linear-PEG-NHS were matched to each other (M_w = 5 kg/mol). From this point forward, the Tetra-PEG gels formed from prepolymers with M_w = 10, 20, and 40 kg/mol are named Tetra10K, Tetra20K, and Tetra40K, respectively. In addition, a mixed solution of LinearPEG-NH_2 and Linear-PEG-NHS is named Linear5K.

3.2.2 IR Spectroscopy

In this work, we carried out IR measurements with attenuated total reflection (ATR) technique to obtain quantitative spectra for polymer solutions. ATR-IR spectra were measured at a resolution of 2 cm^{-1} with an accumulation of 128 scans using a Nicolet 6700 Fourier-transform IR spectrometer equipped with a liquid-nitrogen-cooled MCT detector. The solution was filled in an ATR cell, which was made of a horizontal ZnSe crystal (R.I. 2.403) with an incident angle of 45°. The ATR cell was kept at 20 °C with an accuracy of 0.1 °C throughout the entire experiment by using a homemade thermoelectric device. The ATR cell was sealed by a toggle-clamp-type cover to prevent the evaporation of solvent. Constant amounts of Tetra-PEG-NH$_2$ ($M_n = 10$ kg/mol, "ϕ": $0.034 - 0.15$) and Tetra-PEG-NHS ($M_n = 10$ kg/mol,"ϕ": $0.034 - 0.15$) were dissolved in aqueous phosphate buffer solution (0.2 M, pH 7). The two solutions thus obtained were mixed in a 50 mL Falcon tube for 30 s at 20 °C, and poured into the ATR cell.

IR spectra obtained were deconvoluted to extract single bands. A single band is assumed to be represented as a pseudo-Voigt function, $f_\mathrm{V}(\nu) = \gamma f_\mathrm{L}(\nu) + (1 - \Gamma) f_\mathrm{G}(\nu)$, where $f_\mathrm{L}(\nu)$ and $f_\mathrm{G}(\nu)$ stand for Lorentzian and Gaussian components, respectively, and the parameter γ ($0 < \gamma < 1$) is the Lorentzian component. A nonlinear least-squares curve fitting procedure was employed for the analyses. The integrated intensity A of a single band is evaluated according to $A = \gamma A_\mathrm{L} + (1 - \gamma) A_\mathrm{G}$, where A_L and A_G denote integrated intensities of the Lorentzian and Gaussian components, respectively.

3.2.3 UV spectroscopy

Absorption spectra were recorded on JASCO UV-vis spectrophotometer V-630, Nihonbunko, Japan. The quartz cell (thickness : 0.2 cm) was kept at 20 °C throughout the entire experiment. In degradation system, a given amount of PEG-NHS (LinearPEG:15 mg, 10 kg/mol Tetra-PEG: 7.5 mg, 20 kg/mol Tetra-PEG : 15 mg, 40 kg/mol Tetra-PEG : 30 mg) was dissolved in 3.0 mL water including 0.2 M phosphate buffer (pH 7.0) at 20 °C, and the solution was added into an quartz cell just after sample preparation. The measurement time (total) was about 40,000 seconds corresponding to the end of the degradation, and the time interval was 120 seconds at each spectra. In coupling reaction system, aqueous PEG-NH$_2$ and PEG-NHS solutions with same polymer concentration ("ϕ": $0.034 - 0.12$) in 0.2 M phosphate buffer (pH 7) were prepared and then they were mixed in a 50 mL Falcon tube for 30 s at 20 °C, followed by pouring into the cell. Detail procedure of the measurements is the same with above degradation system.

3.3 Results and Discussion

3.3.1 IR measurement on the gelation kinetics

Figure 3.1(a) shows the time dependence of IR spectra for Tetra10K components at 20 °C obtained by subtracting those for buffer solutions. The peak intensities at 1728, 1778, and 1812 cm^{-1} decrease and those at 1614, 1646, 1670, and 1704 cm^{-1} increase with progressing reaction. The IR spectra showed an isosbestic point at around 1720 cm^{-1}, implying that the polycondensation process in the Tetra-PEG gel system is successfully observed by our IR technique examined here. Figure 3.1(b) shows a typical deconvoluted IR spectrum observed at 144 s. According to theoretical IR bands calculated in our previous work,[13] the IR spectrum can be deconvoluted into eight bands, i.e., three bands at 1728, 1778, and 1812 cm^{-1} originated from terminal NHS, three at 1646, 1670, and 1704 cm^{-1} from dissociated NHS ion, and the 1624 cm^{-1} band from a newly formed amide bond. The band at 1728 cm^{-1} disappears at 11050 s in Figure 3.1(a), which indicates that all terminal NHS are dissociated by the aminolysis and the degradation of terminal NHS, and all dissociated NHS contribute to the peak intensity at 1646 cm^{-1}. Therefore, we calculate the concentration of the dissociated NHS ion as follows.

$$\left[\mathrm{NHS}^{-}\right](t) = \frac{[-\mathrm{NHS}]_0}{A_{1646}(\infty)} A_{1646}(t) \tag{3.1}$$

Here, $\left[\mathrm{NHS}^{-}\right](t)$, $[-\mathrm{NHS}]_0$, $A_{1646}(\infty)$, and $A_{1646}(t)$ denotes the concentration of the dissociated NHS ion at time t, the initial concentration of the terminal NHS, the IR intensity at 1646 cm^{-1} at the end of reaction, and at time t, respectively. Figure 3.2 shows the kinetic traces for the dissociated NHS ion, $\left[\mathrm{NHS}^{-}\right]$ evaluated from eq (3.1). The fit results using eqs (2.6) and (2.7) are also shown in Figure 3.2. Here, k_{deg} is fixed to the value obtained from the degradation analysis as discussed in our previous work.[13] The fit worked well from the initiation to nearly completion of reaction. Figure 3.3 shows the rate constant, k_{gel}, plotted against polymer concentration ϕ. As shown in Figure 3.3, the reaction rate constants are almost constant regardless of polymer concentration. The rate constants obtained here are almost the same as that reported for the aminolysis of anisoyl-NHS and n-butylamine in aqueous dioxane, 20% (v/v) in the literature, 50.9 $\mathrm{dm}^3/\mathrm{mol/s}$.[15] From the facts that (1) no dependence of the k_{gel} on the polymer concentration and (2) the k_{gel} is almost the same as those of the aminolysis in a low molecular system, we can point out that the gelation reaction of Tetra-PEG gel is considered to be not diffusion-limited but reaction-limited. In order to investigate the gelation mechanism for further details, we extended our study to study M_w dependence of the reaction kinetics. UV-vis spectroscopy was carried out to determine the rate constants, as described below.

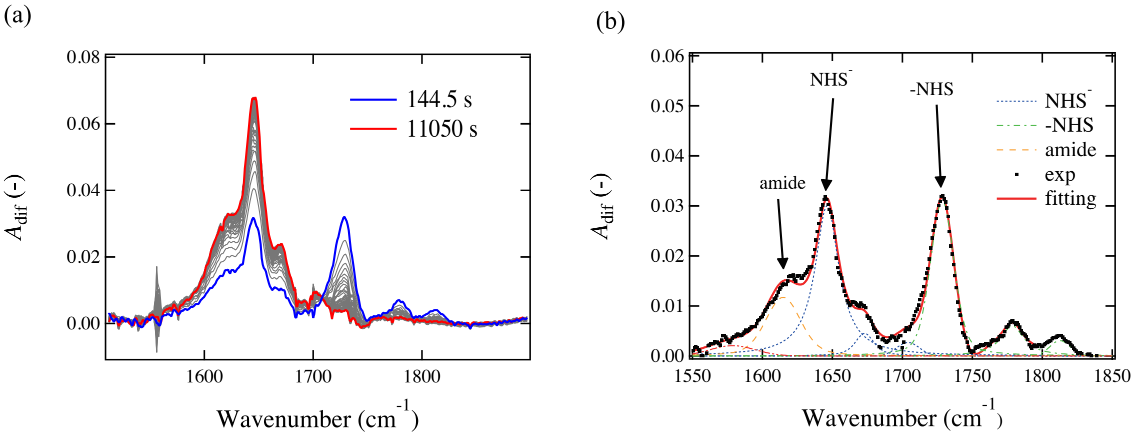

Figure 3.1: (a) Time dependence of IR spectra for the gelation of Tetra- PEG gel ($\phi = 0.096$) in solution containing 0.2 M phosphate D-buffer (pH 7.0) at 20 °C. (b) Typical deconvoluted IR bands on a gelation process, $\phi = 0.096$ at 144 s (20 °C). Dotted black and red lines show the observed and calculated IR spectra. Blue, green, and orange lines correspond to the dissociated NHS, terminal NHS, and amide bond components, respectively.

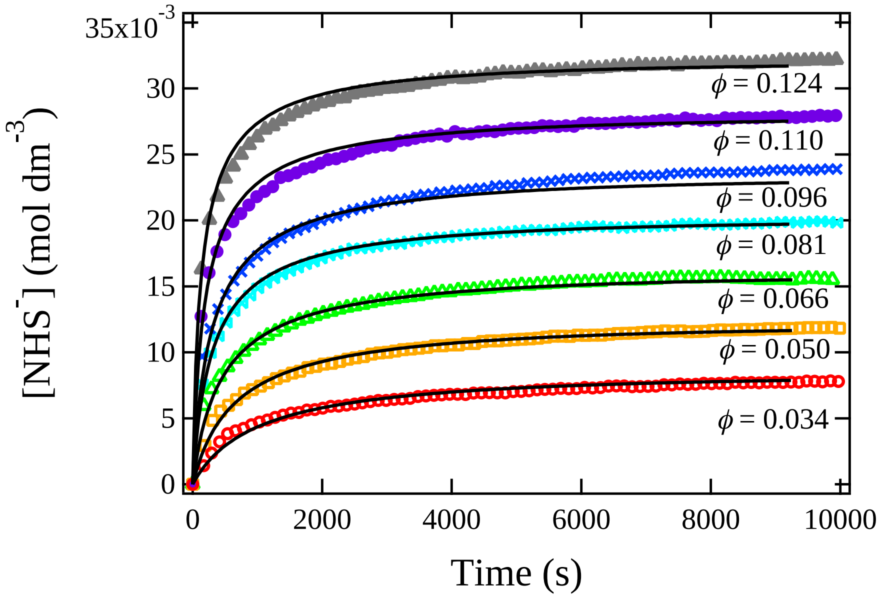

Figure 3.2: Kinetic trace obtained for the gelation at 1646 cm^{-1} (C-O stretching vibration of dissociated NHS) as a function of time.

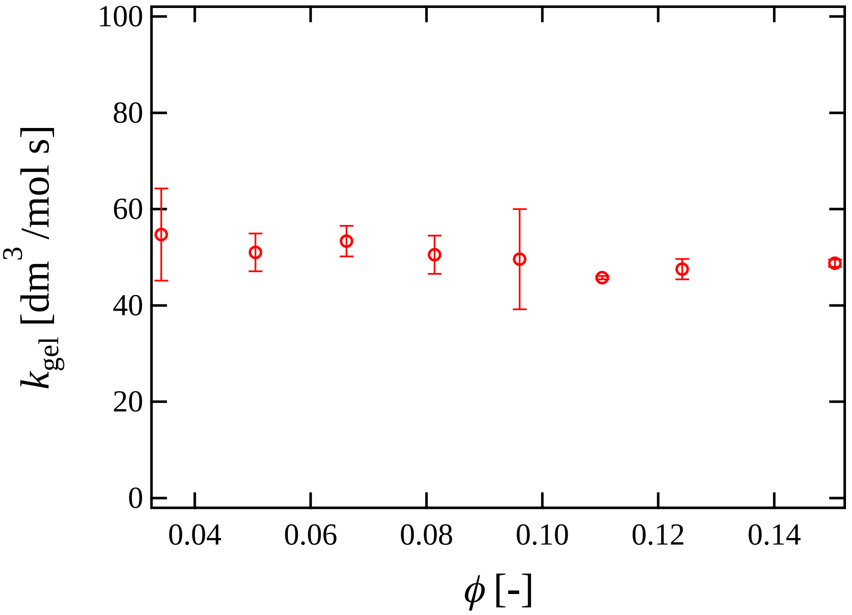

Figure 3.3: k_{gel} plotted against polymer concentration ϕ.

3.3.2 UV measurement on the degradation kinetics of TNPEG

Figure 3.4(a) shows the time dependence of UV spectra for the degradation kinetics of Linear-PEG-NHS ($\phi = 0.0044$). It has been already established in the previous work[16] the dissociated NHS, i.e., $\left[\mathrm{NHS}^-\right]$ in water system shows the absorbance at around 260 nm, whereas it is not for Tetra-PEG-NHS before degradation or gelation. As can be seen in Figure 3.4(a), the peak intensity observed at 260 nm gradually increased with increasing t, indicating that the degradation reaction quantitatively undergoes in the aqueous solution. Figure 3.4(b) shows the kinetic traces of $\left[\mathrm{NHS}^-\right]$ in four PEG-NHS systems (Linear5K and Tetra10K, Tetra20K and Tetra40K), i.e., dissociated NHS ion concentration based on the peak intensity at 260 nm plotted against time. The degradation rate constant, k_{deg}, is estimated by least-squares-fit analysis on the basis of the following rate equation: $-d\left[-\mathrm{NHS}\right]/dt = d\left[\mathrm{NHS}^-\right]/dt = k_{\mathrm{deg}}\left[-\mathrm{NHS}\right]$. The observed variation was well represented with the fitting curve (solid line). The k_{deg} for Tetra-PEG-NHS of M_w = 10 kg/mol, 20 kg/mol, and 40 kg/mol evaluated by the fitting analysis are 2.14×10^{-4}, 1.84×10^{-4}, and 1.88×10^{-4} dm^3/mol/s, respectively. In addition, the degradation rate constants for Linear-PEG-NHS is 2.76×10^{-4} dm^3/mol/s. These values will be used as fitting parameters in the following section.

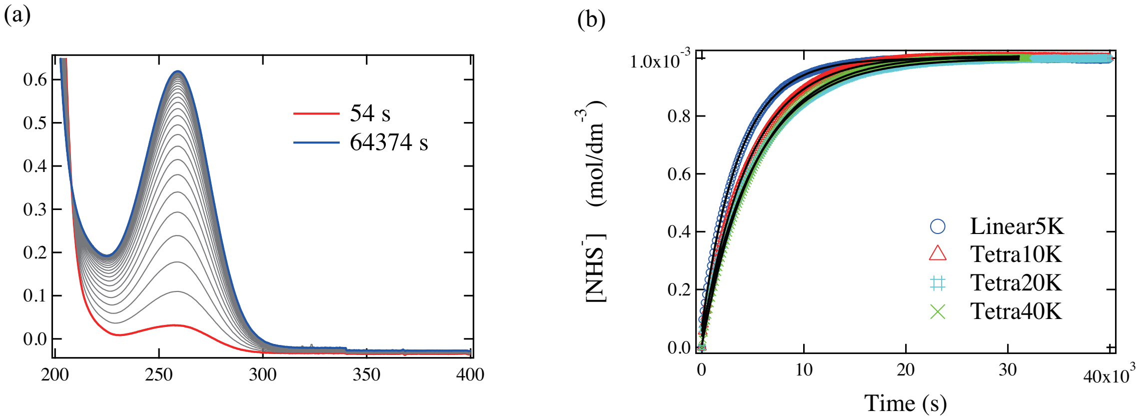

Figure 3.4: (a) Time dependence of UV spectra for the degradation of linear PEG (ϕ = 0.044) in solution containing 0.2 M phosphate buffer (pH 7.0). (b) Kinetic trace obtained for the degradation of terminated NHS at 260 nm as a function of time.

3.3.3 UV measurement on the gelation kinetics of Tetra-PEG gel

As describe in the experimental section, the Tetra-PEG gels formed from prepolymers with M_w = 10, 20, and 40 kg/mol are named Tetra10K, Tetra20K, and Tetra40K, respectively. In addition, a mixed solution of LinearPEG-NH$_2$ and LinearPEG-NHS is named Linear5K. Figure 3.5(a) shows the time dependence of UV spectra for the coupling kinetics of Tetra20K (ϕ =0.066). As shown in Figure 3.5(a), the peak intensity at 260 nm was completely saturated over the reaction time 320 sec. Therefore, we evaluated the dissociated NHS$^-$ concentration, $\left[\mathrm{NHS}^-\right]$ from the absorbance at 285, 287 and 290 nm, resulting in the similar kinetic trace among them (see Figure 3.5(b)). Here, the evaluation procedure of $\left[\mathrm{NHS}^-\right]$ from absorption spectra is the same as the previous section. The solid lines in Figure 3.5(b) show the theoretical curve obtained from fitting analysis using eqs 2.6 and 2.7, which is in good agreement with the observed data from the initiation to nearly completion of reaction.The same procedure was applied to Tetra10K, Tetra40K and Linear5K with various polymer concentrations.

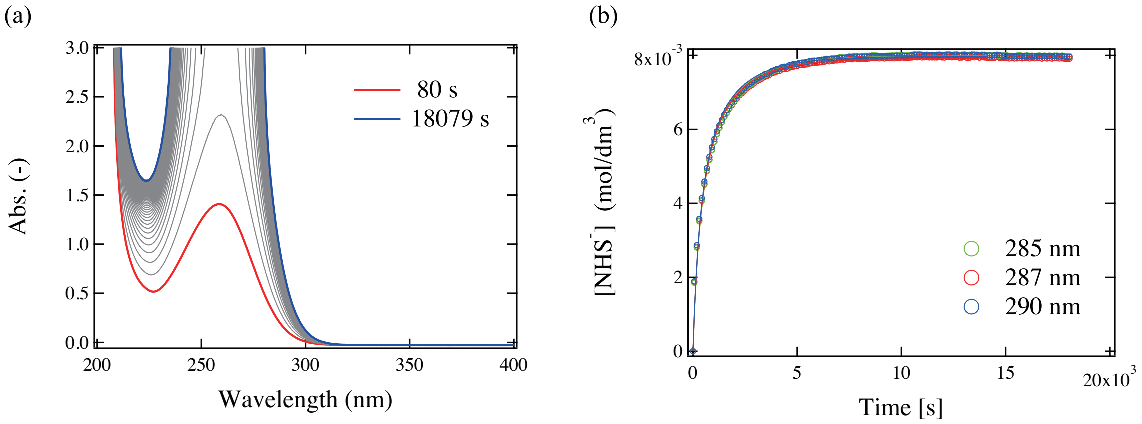

Figure 3.5: (a) Time dependence of UV spectra for the gelation of 20K Tetra-PEG macromers (TNPEG: ϕ = 0.066; TAPEG: ϕ = 0.066) in solution containing 0.2 M phosphate buffer (pH 7.0). (b) Kinetic trace obtained for the gelation at 285, 287, 290 nm as a function of time.

Figure 3.6 shows concentration dependences of the kinetic trace of $\left[\mathrm{NHS}^{-}\right]$ for (a) Linear5K, (b) Tetra10K, (c) Tetra20K, and (d) Tetra40K systems. Here, note that the k_{deg} is fixed to the value determined from the degradation analysis in the previous section. The observed data (symbols) was well represented with the fitting one (solid line) for all the systems, in the gelation entire time-range from the initiation to nearly completion of reaction. The gelation rate constant, k_{gel} was successfully estimated for all the systems, which is shown in Figure 3.7. As shown in Figure 3.7, it was clearly found that the k_{gel} values obtained here are almost constant within experimental error regardless of polymer volume fraction, ϕ and prepolymer molecular weight, M_w, and their k_{gel} values for Tetra-PEG gel are essentially consistent with those for linearPEG system (Linear5k).

Figure 3.6 shows the kinetic traces for $\left[\mathrm{NHS}^{-}\right]$ for (a) Linear5K, (b) Tetra10K, (c) Tetra20K, and (d) Tetra40K. The fit results using eqs 2.6 and 2.7 are also shown in Figure 3.6. Here, k_{deg} is fixed to the value obtained from the degradation analysis in a previous section. The fit worked well from the initiation to nearly completion of reaction. Figure 3.7 shows the rate constant, k_{gel}, plotted against polymer concentration ϕ. As shown in Figure 3.7, k_{gel} are almost constant within experimental error regardless of polymer concentration and primary molecular weight. Also, the reaction rate constants for the gelation kinetics of Tetra-PEG gel are consistent with those of the reaction kinetics of linear-PEG.

Here, we can point out that these k_{gel} values correspond to the aminolysis of a low-molecular weight system[15] such as 50.9 $\mathrm{dm}^3\ \mathrm{mol}^{-1}\ \mathrm{s}^{-1}$, and are much smaller than other diffusion limited systems. For example, rate constants for diffusion controlled reaction of polymer solutions are in the range of $10^8 \sim 10^9$ $\mathrm{dm}^3\ \mathrm{mol}^{-1}\ \mathrm{s}^{-1}$, which depends on polymerization degree and concentration. For another example, rate constants for cross-linking photopolymerization[1–10, 17–24] are in the order of $10^4 \sim 10^5$ $\mathrm{dm}^3\ \mathrm{mol}^{-1}\ \mathrm{s}^{-1}$, and depends on chain-length in monomer and cross-link concentration. In contrast, rate constants of Tetra-PEG gel system are constant around 70 $\mathrm{dm}^3\ \mathrm{mol}^{-1}\ \mathrm{s}^{-1}$, which does not depend on primary molecular weight and polymer concentration. We thus propose here that the gelation kinetics of Tetra-PEG gel is the reaction-limited mechanism not diffusion-limited one. Therefore, the reaction undergoes as a simple second-order reaction during entire course of gelation. That is, the reaction rate of the amide bond formation is much slower than the collision

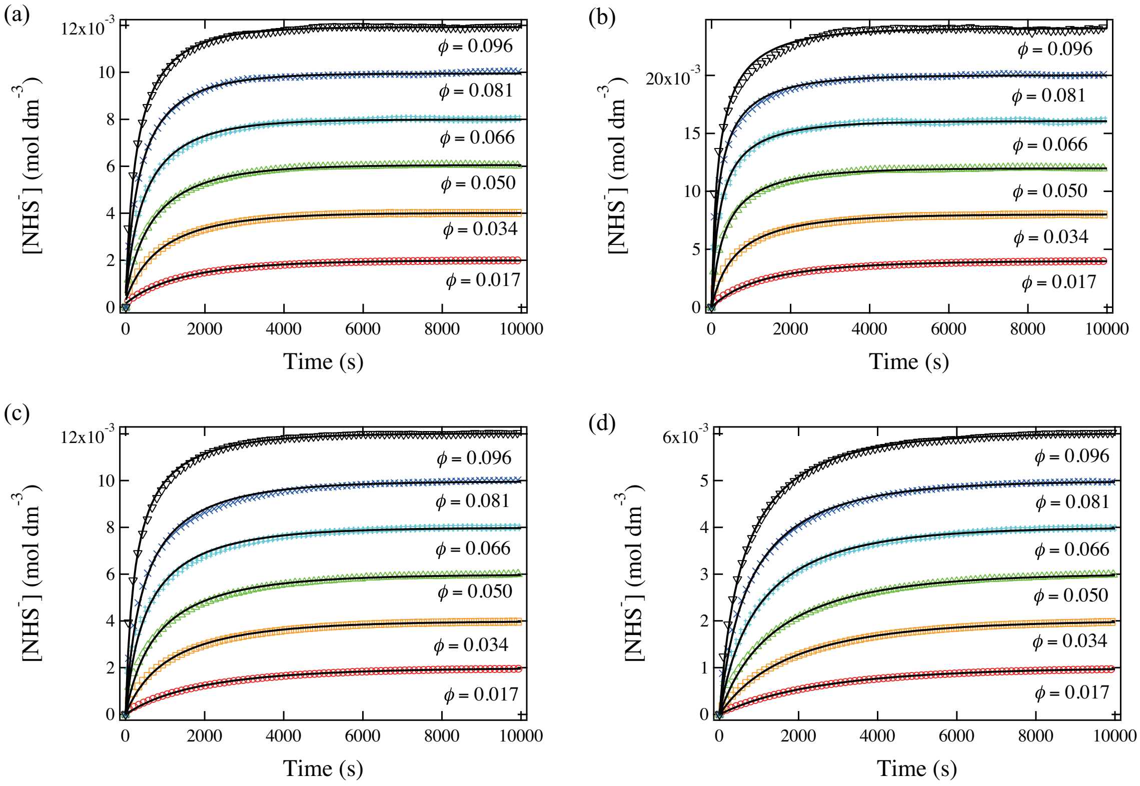

Figure 3.6: Kinetic trace obtained for the gelation of (a) Linear5K, (b) Tetra10K, (c) Tetra20K, and (d) Tetra40K.

rate of the terminal NHS and amine groups.

We have already reported that Tetra-PEG gel has an excellent mechanical property due to a homogeneous polymer network. It is expected that the gelation reaction with reaction-limited in Tetra-PEG system is one of the reason why polymer network is homogeneously formed in Tetra-PEG system. To clearly discuss this at the molecular level, we depict a schematic picture for the reaction process of the diffusion-limited and the reaction-limited cases for AB type cross-end coupling reaction in Figure 3.8. In the case of the diffusion-limited reaction, the reaction rate is much higher than the collision rate of A and B. Therefore, A and B react just after A and B encounter, and prepolymers cannot mix homogeneously. Hence, the gelation reaction proceeds neither efficiently nor uniformly as shown in Figure 3.8(a). On the other hand, in the case of the reaction-limited reaction, which is the case of Tetra-PEG gel, the collision rate of A and B is much higher than the reaction rate. Even if A is close to B, the encountered pairs are often separated without bond formation. Because A and

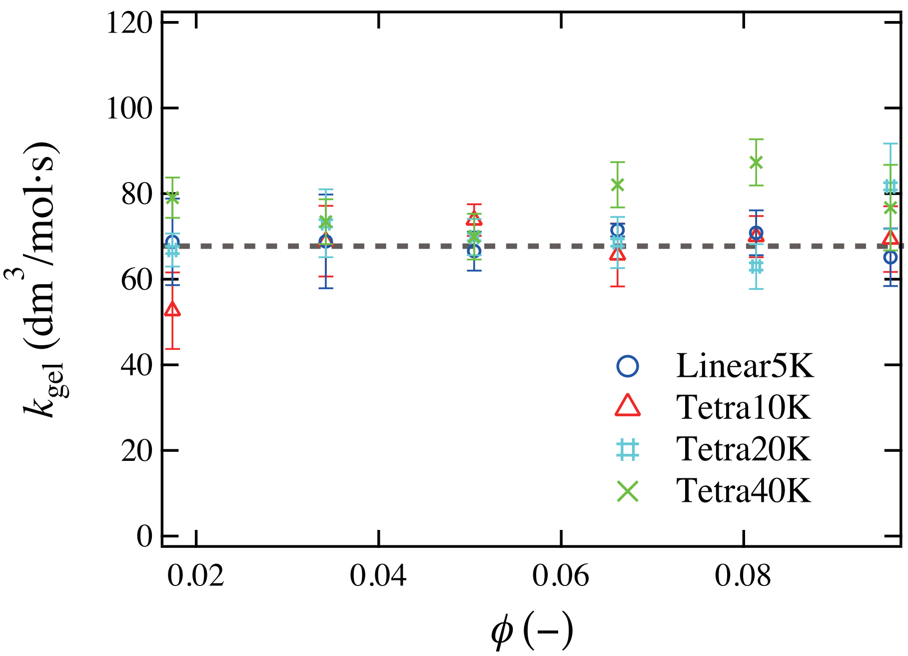

Figure 3.7: k_{gel} plotted against polymer concentration ϕ for Linear5K, Tetra10K, Tetra20K, and Tetra40K.

B prepolymers easily diffuse and are homogeneously mixed in the system, the gelation reaction proceeds efficiently and uniformly as depicted in Figure 3.8(b). These discussions imply that, in order to achieve high-efficient and homogeneous gel, it is necessary to attach reaction groups whose reaction rate is relatively low but the final conversion is high.

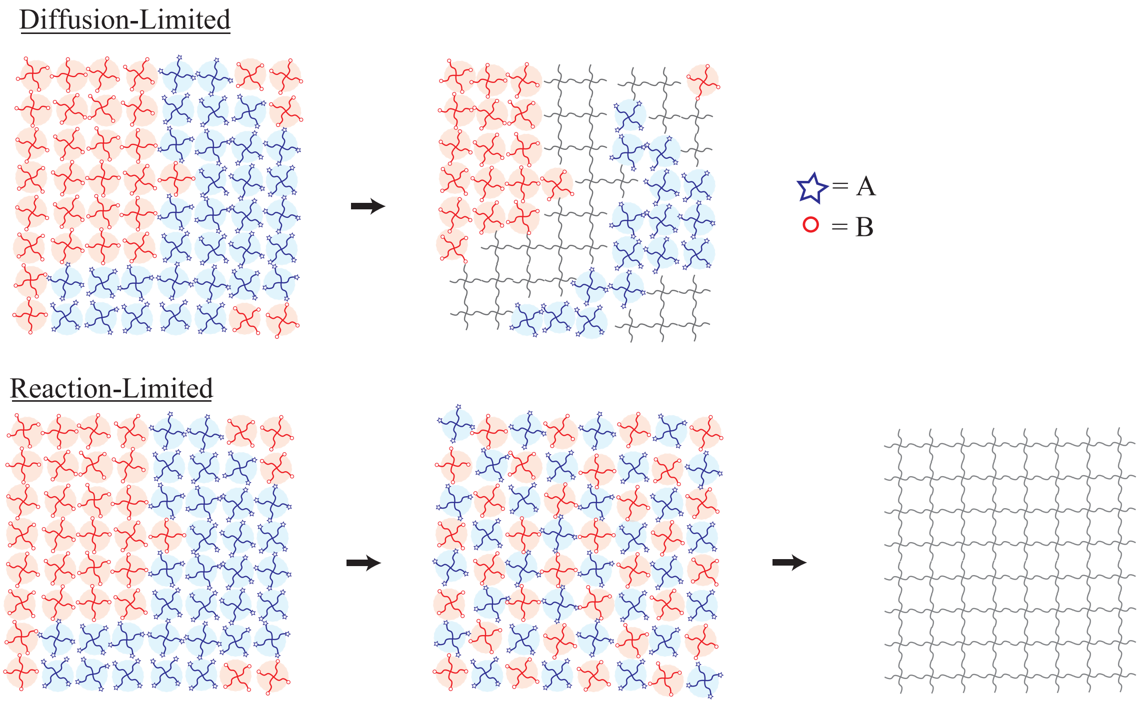

Figure 3.8: A schematic picture of reaction process of Tetra-PEG gel in the case of a diffusion-limited gelation and a reaction-limited gelation.

3.4 Conclusion

The gelation mechanism of Tetra-PEG gel was investigated by IR and UV measurements. It was found that the reaction rate constant of gelation kinetics of Tetra-PEG gelation is independent of polymer concentration and the prepolymer molecular weight. In addition, the reaction rate is comparable to that of linear-PEG systems, and corresponds to the aminolysis of a low molecular system. These results indicate that the gelation reaction of Tetra-PEG gel is not diffusion-limited but reaction-limited. It is concluded that the reaction-limited reaction is one of the keys of homogeneous network formation of Tetra-PEG gel.

References

[1] Schulz, G. V., *Z. Phys. Chem. (Muenchen)*, 1956, 8.

[2] Anseth, K. S.; Kline, L. M.; Walker, T. A.; Anderson, K. J.; Bowman, C. N., *Macromolecules*, **1995**, 28, 2491-2499.

[3] Li, W.-H.; Hamielec, A. E.; Crowe, C. M., *Polymer*, **1989**, 30, 1513-1517.

[4] Li, W.-H.; Hamielec, A. E.; Crowe, C. M., *Polymer*, **1989**, 30, 1518-1523.

[5] Zhu, S.; Tian, Y.; Hamilec, A. E.; Eaton, D. R., *Polymer*, **1990**, 31, 154-159.

[6] Scranton, A. B.; Bowman, C. N.; Klier, J.; Peppas, N. A., *Polymer*, **1992**, 33, 1683-1689.

[7] Young, J. S.; Bowman, C. N., *Macromolecules*, **1999**, 32, 6073-6081.

[8] Cook, W. D., *J. Polym. Sci. A. Polym. chem.*, **1993**, 31, 1053-1067.

[9] Berchtold, K. A.; Bowman, C. N., *RadTeck Europe99 Conference Proceedings*, **1999**, 767.

[10] Anseth, K. S.; Wang, C. M.; Bowman, C. N., *Macromolecules*, **1994**, 27, 650-655.

[11] Sakai, T.; Matsunaga, T.; Yamamoto, Y.; Ito, C.; Yoshida, R.; Suzuki, S.; Sasaki, N.; Shibayama, M.; Chung, U. I., *Macromolecules*, **2008**, 41, (14), 5379-5384.

[12] Fujii, K.; Asai, H.; Ueki, T.; Sakai, T.; Imaizumi, S.; Chung, U.; Watanabe, M.; Shibayama, M., *Soft Matter*, **2012**, 8, (6), 1756-1759.

[13] Nishi, K.; Fujii, K.; Chijiishi, M.; Katsumoto, Y.; Chung, U.; Sakai, T.; Shibayama, M., *Macromolecules*, **2012**, 45, (2), 1031-1036.

[14] Kurakazu, M.; Katashima, T.; Chijiishi, M.; Nishi, K.; Akagi, Y.; Matsunaga, T.; Shibayama, M.; Chung, U.; Sakai, T., *Macromolecules*, **2010**, 43, (8), 3935-3940.

[15] Cline, G. W.; Hanna, S. B., *J. Org. Chem.*, **1988**, 53, 3583-3586.

[16] Miron, T.; Wikchek, M., *Anal. Biochem.*, **1982**, 126, 433-435.

[17] Kloosterboer, J. G., *Adv. Polym. Sci.*, **1988**, 84, 1-61.

[18] Miyazaki, K.; Horibe, T., *J. Biomed. Mater. Res.*, **1988**, 22, (11), 1011-1022.

[19] Allen, P.; Simon, G.; Williams, D.; Williams, E., *Macromolecules*, **1989**, 22, 809-816.

[20] Cook, W. D., *Polymer*, 1992, 33, 600-609.

[21] Simon, G.; Allen, P.; Bennett, D.; Williams, D.; Williams, E., *Macromolecules*, **1989**, 22, (2), 3555-3561.

[22] Allen, P.; Bennett, D.; Hagias, S.; Hounslow, A.; Ross, G.; Simon, G.; Williams, D.; Williams, E., *Eur. Polym. J.*, **1989**, 25, 785-789.

[23] Kloosterboer, J.; Lijten, G.; Boots, H., *Makromol. Chem., Macromol. Symp.*, **1989**, 24, 223-230.

[24] Bowman, C. N.; Peppas, N. A., *Macromolecules*, **1991**, 24, 1914-1920.

[25] Mita, I.; Horie, K.; Takeda, M., *Macromolecules*, **1981**, 14, 1428-1433.

[26] Friedman, B.; O 'Shaughnessy, B., *Macromolecules*, **1993**, 26, 5726-5739.

[27] Friedman, B.; O 'Shaughnessy, B., *Europhys. Lett.*, **1993**, 23, (9), 667-672.

[28] Friedman, B.; O 'Shaughnessy, B., *Macromolecules*, **1993**, 26, (4888-4898), 4888.

[29] O 'Shaughnessy, B., *Macromolecules*, **1994**, 27, 3875-3884.

Chapter 4

The first approximation of the elastic modulus around $p = 1$

4.1 Introduction

The theories of rubber elasticity describe the macroscopic relationships between the mechanical stress and the strain of elastometric materials on the basis of microscopic structure of polymer.[1–8] By using the theories of rubber elasticity, we can obtain the structural information of rubbers and gels from a simple stress-strain measurement of a piece of rubber, such as the concentration of elastically effective chains, the chain length between cross-links, and the number of trapped entanglements.[8] Considering the significance of a variety of applications of rubbers in the history, proper and better understanding of the theories of rubber elasticity is very important not only from basic science but also from industrial points of view.

In spite of its long history of the theories of rubber elasticity, there still remain some topics. One of major topics is the relationship between the reaction probability (p) and the elastic modulus (G). Note that, though the relationship between G and the structure parameters, such as the number of elastically effective chains (n) and elastically effective cross-links (m) is well established as discussed in affine network model and phantom network model, the relationship between p and G is not well established. In order to derive this relationship, we need to describe the network structure at a given p and specify which bond in the network is elastically effective. This topic is important not only in the scientific terms of description of a random polymer network, but also in the industrial terms of evaluation of connectivity defects.

In this topic, there are two problems. The first problem is that a theory describing the relationship between the reaction probability (p) and the elastic modulus (G) on general lattices, such as a triangular lattice or a diamond lattice, is not well established. The typical model giving the analytical solution is a tree like theory, which is proposed by Flory,[9] Scanlan,[10] Case,[11] and Miller and Macosko.[12] This theory provides a clear picture of percolation threshold and the fractions of various ranks of crosslinking as a function of p for post-gelation systems, i.e., $p > p_c$, where p_c is the reaction probability at gelation threshold. Hence, the tree-like theory has often been employed to discuss the effect of p on rubber elasticity. However, the tree-like theory was developed on an unrealistic structure, i.e., tree-like structure (See Figure 4.1(a)), where intramolecular reaction (the loop) is not allowed (See Figure 4.1(b)). Because of this assumption, the tree-like theory has a serious problem that a cluster spanning the whole system cannot fit in the 3D space.[13] As a result, the tree-like theory has been open to criticism since it was proposed. In order to overcome this criticism, many studies on loops have been conducted, but a simple and general method is not well established.[14–16]

The second problem is that experimentally suitable systems for examining the theory of elasticity have never been available. As a matter of fact, it was impossible to prepare a model network consisting of monodisperse strands (i.e., chains between neighboring crosslinks) and free from entanglements. We have overcome this problem by developing a new type of polymer network, i.e., Tetra-PEG gel.[17]

In this study, we investigate the effect of local topology of the network or the existence of the loops on the relationship between G and p in the $p \gg p_c$ region. First, we derived the approximate expression of G for the loops-containing network in the $p \gg p_c$ region. Secondly, we conducted simulations for deformation of polymer chains on triangular and diamond lattices.[18] Finally, we made mechanical testing experiments on a p-tuned Tetra-PEG gel. Tetra-PEG gels are formed by A-B type cross-end coupling of two tetra-arm poly(ethylene glycol) (PEG) unit.[17] Our previous works demonstrated that a Tetra-PEG gel is free from heterogeneities and is a potential candidate for an ideal polymer network.[19] In this experiment, we prepare a series of p-tuned Tetra-PEG gel networks by forming Tetra-PEG gel with activity-tuned TNPEG. Here, TNPEG denotes tetra-arm PEG having activated ester group, i.e., N-hydroxysuccinimidyl (NHS) ester (TNPEG) at chain end. The activity of the activated ester on TNPEG is tuned by partial hydration prior to the initiation of gelation reaction (Figure 4.2). The elastic moduli for p-tuned networks obtained will be compared with general law proposed in this work and the tree-like theory.

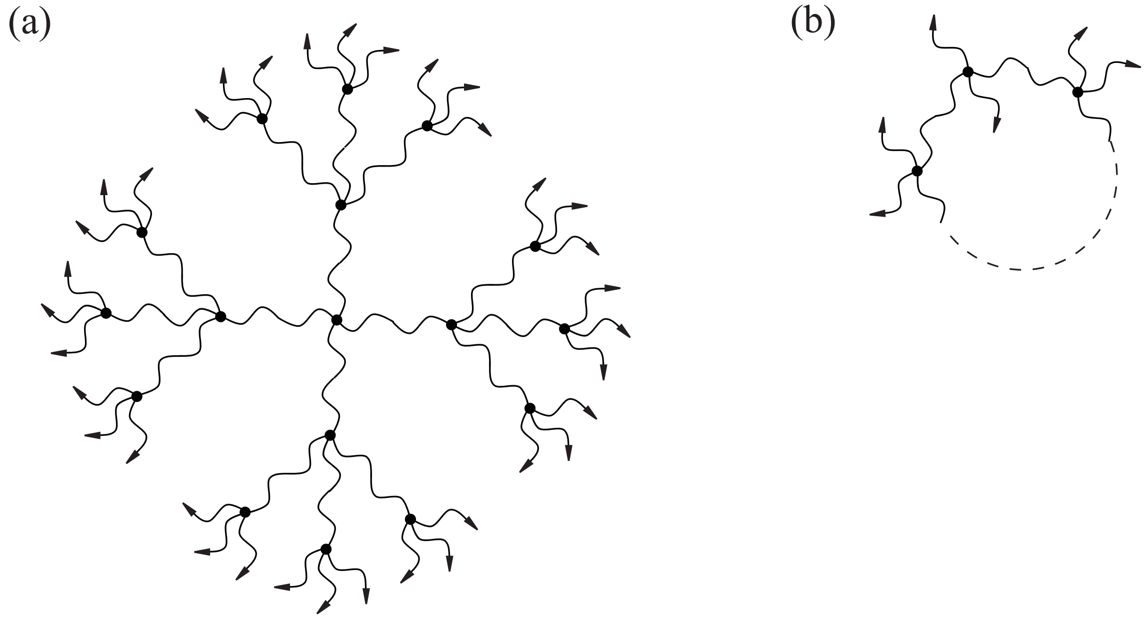

Figure 4.1: (a) Schematic picture of tree-like structure. Elastically effective cross-links are shown by filled circles. Arrows identify chains leading to infinity. (b) An example of a loop structure. Loops are not taken into consideration in the tree-like theory.

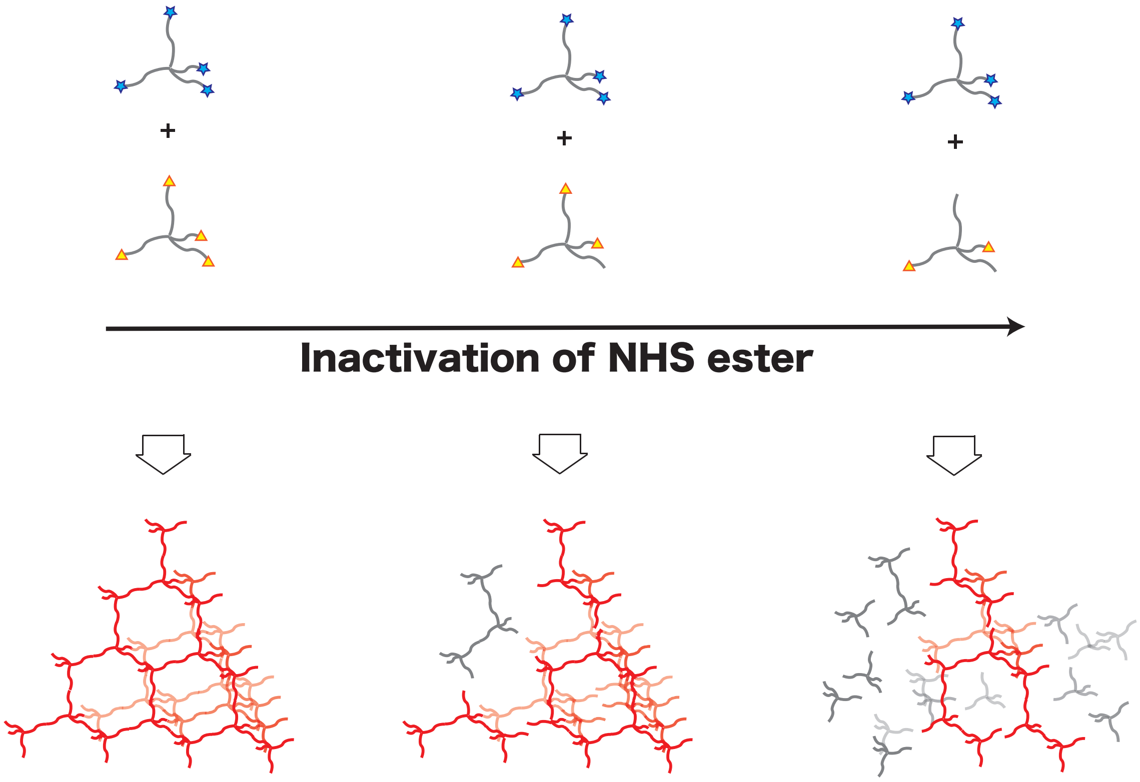

Figure 4.2: The schematic picture of sample preparation. The stars and triangles represent the amine and NHS ester terminal groups, respectively. The NHS ester on TNPEG was hydrolyzed in pre-gel solution for a given time in order to control the reaction conversion.

4.2 Theoretical Background

4.2.1 Classical theories of rubber elasticity

First, let us review the elasticity of a single polymer chain. One of the simplest idealizations of a flexible polymer chains consists in replacing it by a random walk on a periodic lattice. The walk is a succession of N steps, starting from one end ($\mathbf{r} = \mathbf{0}$) and ending at a lattice point $\mathbf{r}$. We define $W_N(\mathbf{r})$ as the number of distinct walks going from $\mathbf{0}$ to $\mathbf{r}$ in N steps. The length of one step will be called b. Under this circumstance, the probability that the walk ends at a lattice point $\mathbf{r}$ is calculated from central limit theorem.

$$p(\mathbf{r}) = \frac{W_N(\mathbf{r})}{\sum_{\mathbf{r}} W_N(\mathbf{r})} = \left(\frac{3}{2\pi N b^2}\right)^{\frac{3}{2}} \exp\left(-\frac{3\mathbf{r}^2}{2Nb^2}\right) \tag{4.1}$$

On the basis of the definition of the entropy : $S(\mathbf{r}) = k_{\mathrm{B}} \ln W_N(\mathbf{r})$ and the free energy : $F = E - TS$, the free energy of a polymer chain is given by

$$F(\mathbf{r}) = F(\mathbf{0}) + \frac{3k_{\mathrm{B}}T}{2Nb^2}\mathbf{r}^2 \quad . \tag{4.2}$$

Because the elastic energy of spring is proportional to the square of strain, this equation indicates that an ideal polymer can be regarded as a kind of elastic spring.

Next, we focus on the elasticity of a polymer network. Let us consider the case of a simple extension. This is defined by three principal extension ratios along three mutually perpendicular axes. Under such a strain, a unit cube (Figure 4.3) is transformed into a rectangular parallelepiped having three unequal lengths λ_x, λ_y and λ_z.Here we assumes the constancy of volume, $\lambda_x \lambda_y \lambda_z = 1$.

Let us consider an individual chain (Figure 4.3) having an end-to-end distance represented by the vector $\mathbf{r}_0$ with component (x_0, y_0, z_0) in the unstrained state of the network, and let (x, y, z) be the components of the vector length $\mathbf{r}$ of the same chain after deformation. The end-to-end vector is assumed to change in the same ratio as the macro deformation (Affine deformation); $(x, y, z) = (\lambda_x x_0, \lambda_y y_0, \lambda_z z_0)$. This model is firstly proposed by Kuhn[1] and called Affine model. The difference of the free energy between the unstrained and strained state is

$$\begin{aligned} \Delta F(\lambda_x, \lambda_y, \lambda_z) &= \frac{n}{V}\left(\int F(\mathbf{r})\, p(\mathbf{r}_0)\, d\mathbf{r}_0 - \int F(\mathbf{r}_0)\, p(\mathbf{r}_0)\, d\mathbf{r}_0\right) \\ &= \frac{n}{2V} k_{\mathrm{B}} T \left(\lambda_x^2 + \lambda_y^2 + \lambda_z^2 - 3\right) \quad . \end{aligned} \tag{4.3}$$

Here, n and V denote the number of elastically effective chain and the system volume. In the case of uniaxial deformation, $\lambda_x = \lambda, \lambda_y = \lambda_z = 1/\sqrt{\lambda}$, the stress σ can be obtained by differentiating partially ΔF by λ.

$$\sigma = \frac{\partial \Delta F}{\partial \lambda} = G\left(\lambda - \lambda^{-2}\right) \tag{4.4}$$

G is called the elastic modulus, and therefore, G is given by

$$G = \frac{n}{V} k_{\mathrm{B}} T \quad . \tag{4.5}$$

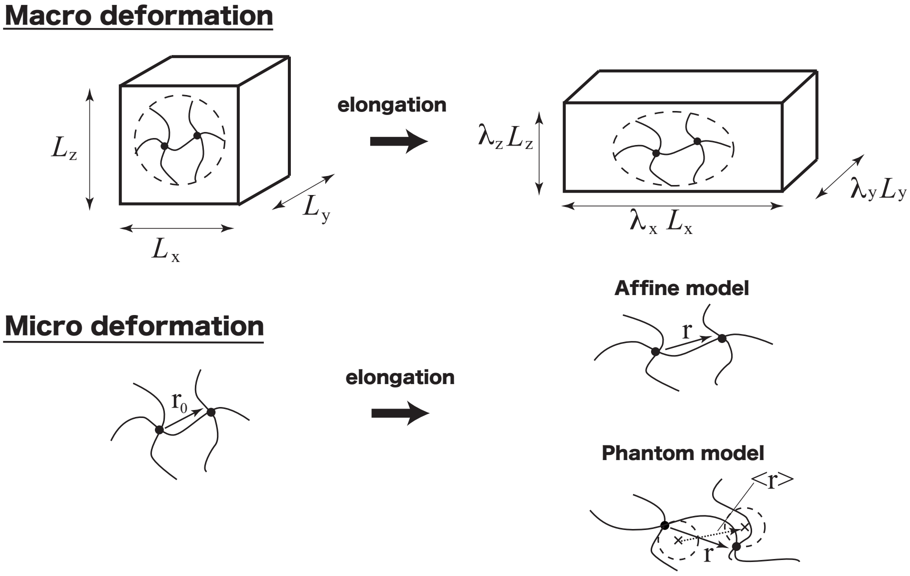

Figure 4.3: Schematic illustration of homogenous strain.

The most obvious objection to this theory in the form outlined above is that the network junction points are conceived of as fixed at particular points in space. The freedom of movement of the system is thus limited to the lengths of chain between these fixed points. However, in reality, the junction points are not fixed but take part in the micro-Brownian motion of the associated chain elements or links. In the very detailed and precise treatment given by James and Guth,[5,6] only junction points which are located on the boundary surfaces of the rubber are specified as fixed; all the other junction points are allowed to fluctuate. Therefore in this theory, they postulate that the mean end-to-end vector changes in the same ratio as the macro deformation; $\langle \mathbf{r} \rangle = (\lambda_x \langle x_0 \rangle, \lambda_y \langle y_0 \rangle, \lambda_z \langle z_0 \rangle)$ and that the fluctuations of position of any junction point in a network of Gaussian chains may be described by a Gaussian probability function. The mean value of the fluctuations of any given junction point is independent of the strain in the network. This model is called phantom model. When we define m as the number of elastically effective cross-links, the elastic modulus of phantom model is calculated as

$$G = (n - m)\, k_{\mathrm{B}} T \qquad . \tag{4.6}$$

It is of particular interest to observe that these equations relate the elastic modulus G to the structural parameters, such as n and m. In order to discuss the elasticity during the gelation process, we need to describe the network structure at a given p and specify which bond in the network is elastically effective. In the next section, we review a classical theory dealing with this relationship, i.e., the tree-like theory. From this point forward, following other studies,[12,19–21] we take the phantom network model in this work.

4.2.2 Tree-like theory

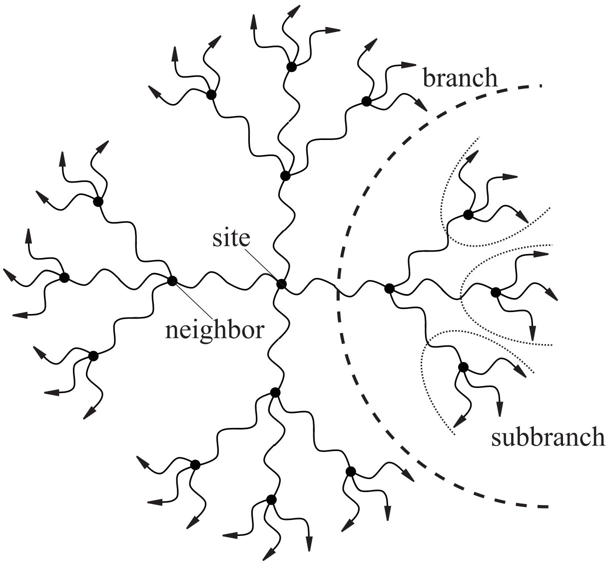

Figure 4.4: The surroundings of the origin of a tree-structure. This figure defines what we mean by neighbor, branch, and sub-branch in our derivation of the exact solution.

The tree-like theory treats polycondensation of f-functional precursor and puts the following assumptions.[12,22]

(i) An elastically effective cross-link is the site which is joined by at least three elastically effective chains.
(ii) All functional groups are equally reactive with the same reactivity throughout the gelation.
(iii) No intramolecular reaction occurs throughout the reaction process.

Here, we define a site, branch, neighbor, and sub-branch as depicted in Figure 4.4. In addition, we define a variable Q as the probability that an arbitrary site is not connected to infinity through one-fixed branch originating from this site. Q can be calculated as follows. One-fixed branch does not lead to infinity, either because the connection is already broken at first neighbor, or because this neighbor is occupied but not connected to infinity by any of its $f-1$ sub-branches. Therefore, p is related to Q by the following recursive equation according to assumptions (ii) and (iii),

$$Q = 1 - p + pQ^{f-1} \tag{4.7}$$

From assumption (i), the concentration of elastically effective chains and cross-links are given by

$$n = \frac{N}{2} \sum_{i=3}^{f} {}_{f}C_{i} \left(1 - Q\right)^{i} Q^{f-i} \tag{4.8}$$

$$m = N \sum_{i=3}^{f} {}_{f}C_{i} \left(1 - Q\right)^{i} Q^{f-i} \tag{4.9}$$

Here, N denotes the number of the precursors, respectively. The relationship between G and p is obtained from eqs. (4.7)-(4.9). For instance, in the case of $f = 4$, Q is given by

$$Q = \left(\frac{1}{p} - \frac{3}{4}\right)^{\frac{1}{2}} - \frac{1}{2} \quad . \tag{4.10}$$

Therefore, the relationship between G and p for the phantom model is given by

$$G_{\mathrm{Ph}} = \left(\left(1 - Q\right)^{4} + 2\left(1 - Q\right)^{3} Q^{1}\right) \frac{N}{V} k_{\mathrm{B}} T \tag{4.11}$$

A Taylor series of G around $p = 1$ is as follows:

$$G_{\mathrm{Ph}} = \left(2 + 2\left(p - 1\right) - 6\left(p - 1\right)^{2} + \cdots\right) \frac{N}{V} k_{\mathrm{B}} T \tag{4.12}$$

As mentioned above, this theory is unrealistic and open to criticism because it assumes no intramolecular reactions. (See Figure 4.1(b).)

4.3 Theory

4.3.1 Percolated Network law ("PN" law)

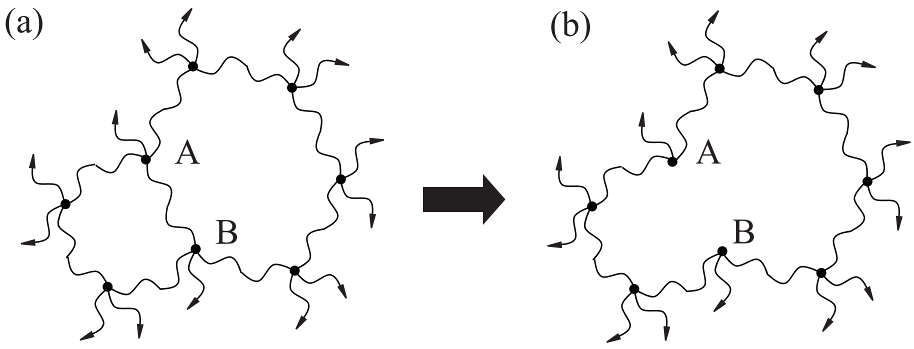

Figure 4.5: (a) A schematic picture of lattice for coordination number 4 at $p = 1$. (b) A schematic picture after cutting the bond that connects sites A with B. Sites A and B are connected with three elastically effective bonds. So the sites A and B are still elastically effective cross-links.

In order to allow loops, we change the assumption. Consider a lattice with the coordination number $f(\geq 4)$ and number of lattice point N. An example for $f = 4$ is depicted in Figure 4.5(a). Here, we put the following assumption.

(i) An elastically effective cross-link is the site which is joined by at least three elastically effective chains.
(ii) All functional groups are equally reactive with the same reactivity throughout the gelation.
(iii) All sites and chains are elastically effective at $p = 1$.

Note that we postulate any types of network structure in which all sites and chains are elastically effective at $p = 1$. So, this assumption can be applied not only to Bethe lattice but also to any other lattices including square and triangular lattice.

At $p = 1$, according to our assumption, the number of elastically effective bonds and cross-links are $n = \frac{f}{2}N$ and $m = N$, respectively. In the next step, let us cut the bond that connects site A with B (Figure 4.5(b)). As seen in Figure 4.5(b), sites A and B are connected with $f - 1$ elastically effective bonds. So, the number of elastically effective bonds and cross-links are expected to be $n = \frac{f}{2}N - 1$ and $m = N$, respectively. When x bonds are cut in a similar manner in the $p \ll p_c$ region, the number of elastically effective bonds and cross-links are expected to be $n = \frac{f}{2}N - x$ and $m = N$, respectively. Using $p = \frac{(fN/2) - x}{fN/2}$, the number of elastically effective bond and cross-links are expected to be $n = \frac{f}{2}Np$ and $m = N$, respectively. Therefore, the elastic modulus for the phantom model in the $p \gg p_c$ region is approximately given by

$$G_{\mathrm{Ph}} \approx \left(\frac{f}{2}p - 1\right) \frac{N}{V} k_{\mathrm{B}} T \quad . \tag{4.13}$$

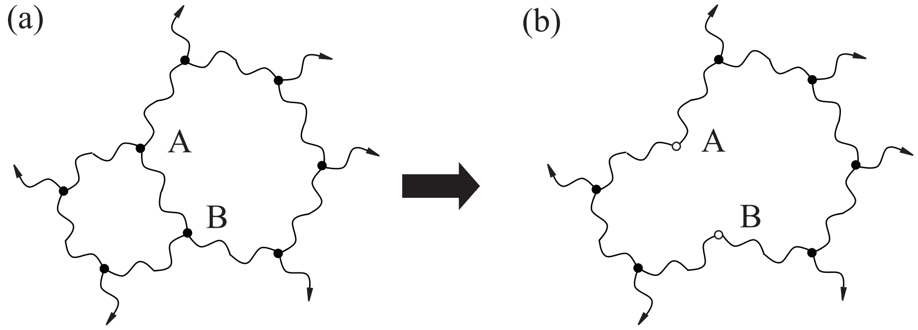

Figure 4.6: (a) A schematic picture of lattice for coordination number 3 at $p = 1$. Elastically ineffective cross-links are shown by open circles. (b) A schematic picture after cutting the bond that connects site A with B. Sites A and B are connected with only two elastically effective bonds. So the sites A and B are not elastically effective cross-links.

Next, let us consider a lattice with coordination number 3. An example for $f = 3$ is depicted in Figure 4.6(a). At $p = 1$, the number of elastically effective bonds and cross-links are $n = \frac{3}{2}N$ and $m = N$, respectively. In the next step, let us cut the bond that connects site A with B (Figure 4.5(b)). As seen in Figure 4.6(b), sites A and B are connected with only two elastically effective bonds. So, the sites A and B are not elastically effective cross-links. The numbers of elastically effective bonds and cross-links are expected to be $n = \frac{3}{2}N - 3$ and $m = N - 2$, respectively. When x bonds are cut in a similar manner in the $p \gg p_c$ region, the number of elastically effective bonds and cross-links are $n = \frac{3}{2}N - 3x$ and $m = N - 2x$, respectively. Using $p = \frac{(3N/2) - x}{3N/2}$, the numbers of elastically effective bonds and cross-links are given to be $n = \frac{9}{2}Np - 3N$ and $m = 3Np - 2N$, respectively. From these results, the elastic modulus for the phantom model in $p \gg p_c$ region is approximately given by

$$G_{\mathrm{Ph}} \approx \left(\frac{3}{2}p - 1\right)\frac{N}{V}k_{\mathrm{B}}T \quad . \tag{4.14}$$

Because eq. (4.14) can be regarded as eq. (4.13) when $f = 3$, eq. (4.13) is satisfied for $f \geq 3$.

The merits of this equation are simplicity and generality. Eq. (4.13) does not depend on the local topology of the network structure or on the existence of loops in the system (Figure 4.7). Moreover, this theory is considered as the first approximation of G around $p = 1$. So, the Taylor series of G of any lattices around $p = 1$ is expected to have a form

$$G_{\mathrm{Ph}} \approx \left\{\left(\frac{f}{2}p - 1\right) + O\left((p-1)^2\right)\right\}\frac{N}{V}k_{\mathrm{B}}T \quad . \tag{4.15}$$

Indeed, eq. (4.12) corresponds to this expression, supporting this prediction. Therefore, we can predict G in the $p \gg p_c$ region, even if we do not know a rigorous expression of G on the lattice, such as triangular lattice or diamond lattice. In addition, high order terms in eq. (4.15) reflect the characteristics of the network structure. Hence, the applicable region of the first approximation depends on the network structure.

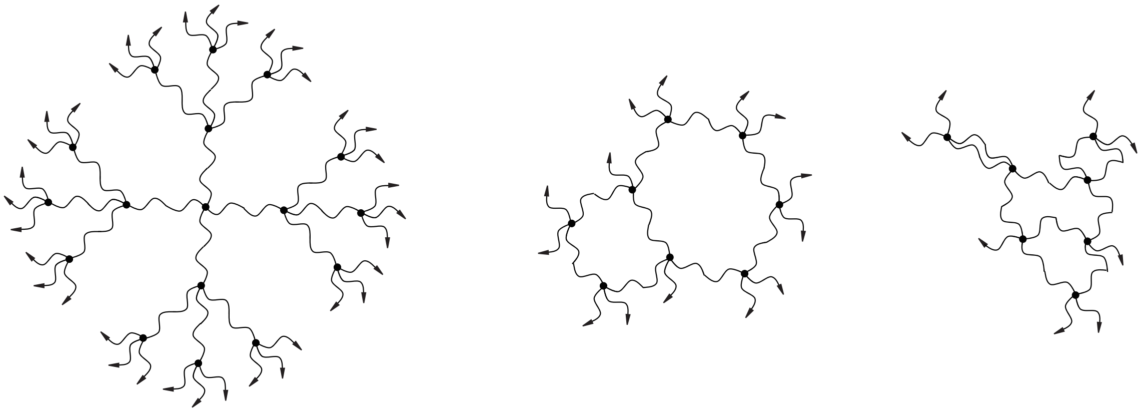

Figure 4.7: Schematic pictures of lattices for coordination number 4. The PN law can be applied to any kind of lattices when all bonds and sites are elastically effective at $p = 1$ as depicted above.

4.3.2 Analogy to electric conductivity of a resistor network

De Gennes proposed there is an analogy between the macroscopic elastic constant of the spring network and the macroscopic conductivity of the resistor network.[23] Let us check the relationship. By normalizing eq. (4.13) with G_0 (G at $p = 1$), we obtain the following equation:

$$\frac{G}{G_0} \approx \frac{p - \dfrac{2}{f}}{1 - \dfrac{2}{f}} \tag{4.16}$$

As for the resistor network, Kirkpatrick proposed the following result by using the effective medium approximation in $p \gg p_c$ region[24]

$$\frac{G^R}{G_0^R} \approx 1 - \frac{1 - p}{1 - \dfrac{2}{f}} \tag{4.17}$$

Here, G^R and G_0^R denote the conductivity of a resistor network with a given bond fraction p and the conductance at $p = 1$, respectively. Here, f is the coordination number of the registor network. Eq. (4.17) corresponds exactly to eq. (4.16). From this point of view, the approximation in this study is not only simple but also valid.

4.4 Methodology

4.4.1 Simulation

A gel is modeled by a network of elastic bonds. First, we construct a regular network on a triangular lattice and a diamond lattice, where each node (cross-link point) has six bonds and four bonds with length l_0, respectively. A periodic boundary condition is employed. The total number of nodes and bonds are $N_{\mathrm{node}} = 10000$ and $N_{\mathrm{bond}} = 30000$ for a triangular lattice and $N_{\mathrm{node}} = 8000$ and $N_{\mathrm{bond}} = 16000$ for a diamond lattice. To investigate the relationship between p and G, p is tuned by random removal of the bonds. For a triangular lattice, the network is percolated for the ratio of left bonds $p \geq 0.35$. We varied the bond ratio from $p = 0.36$ to 1. As for the diamond lattice, the network is percolated for the ratio of left bonds $p \geq 0.39$. Hence, we varied the bond ratio from $p = 0.45$ to 1.

The ith elastic bond is represented by a wormlike-chain (WLC) potential,

$$U_b\left(r_{\mathrm{i}}\right) = \frac{k_{\mathrm{B}} T r_{\mathrm{i}}^2}{4 l_{\mathrm{p}} l_{\max}}\left(\frac{3 l_{\max}-2 r_i}{l_{\max}-r_{\mathrm{i}}}\right) \tag{4.18}$$

$$f_b(r_{\mathrm{i}}) = \frac{k_{\mathrm{B}} T}{l_{\mathrm{p}}}\left(\frac{r_{\mathrm{i}}}{l_{\max}}+\frac{1}{4}\left(\frac{1}{\left(1-r_{\mathrm{i}}/l_{\max}\right)^2}-1\right)\right) \tag{4.19}$$

where $l_{\max}$ and l_p are contour and persistence lengths of the bond chain, respectively. The total energy is $U = \sum_i U_{\mathrm{b}}\left(r_i\right)$ and $k_{\mathrm{B}}T$ is the thermal energy. For $r_i \gg l_{\max}$, the force follows Hooke's law $f_{\mathrm{WLC}}\left(r_i\right) = \left(3 k_{\mathrm{B}} T / 2 l_{\mathrm{p}} l_{\max}\right) r_i$, while $f_{\mathrm{WLC}}\left(r_i\right) \rightarrow \infty$ at $r_i \rightarrow l_{\max}$. Here, $l_{\max} = 40$nm, $l_{\mathrm{p}} = 1.1$nm, and $l_0 = 5.6$nm are used to represent a tetra-PEG gel made from 10 kg/mol macro-monomers.[25] To measure the stress-strain curve of the gel, the gel is gradually stretched by the change of the aspect ratio of the simulation box with constant volume $V = L_x L_y L_z : L_x = \lambda L_0, L_y = L_z = \lambda^{-\frac{1}{2}} L_0$ where L_0 is the side length of the initial cubic simulation box. Since the lattice structure is symmetric, no difference is seen among the stretching in x, y, and z directions. After each step of small change of the ratio λ, the gel network is relaxed to the equilibrium state. The position of nth node is moved by the equation

$$\eta \frac{d \mathbf{r}_n}{d t} = \mathbf{f}_n \tag{4.20}$$

where $\mathbf{f}_n = -\partial U / \partial \mathbf{r}_n$ and η is the viscosity parameter. Eq. (4.20) is numerically solved by Euler method as $\mathbf{r}_n(t+\Delta t) = \mathbf{r}_n + f_n \Delta t / \eta$ until $|U(t+\Delta t)-U(t)| / U(t) <$

10^{-9}. The time step t/η is adjustably varied to keep $U(t+\Delta t) \geq U(t)$. The computation scheme and the relaxation process of triangular network are shown in Figures 4.8 and 4.9.

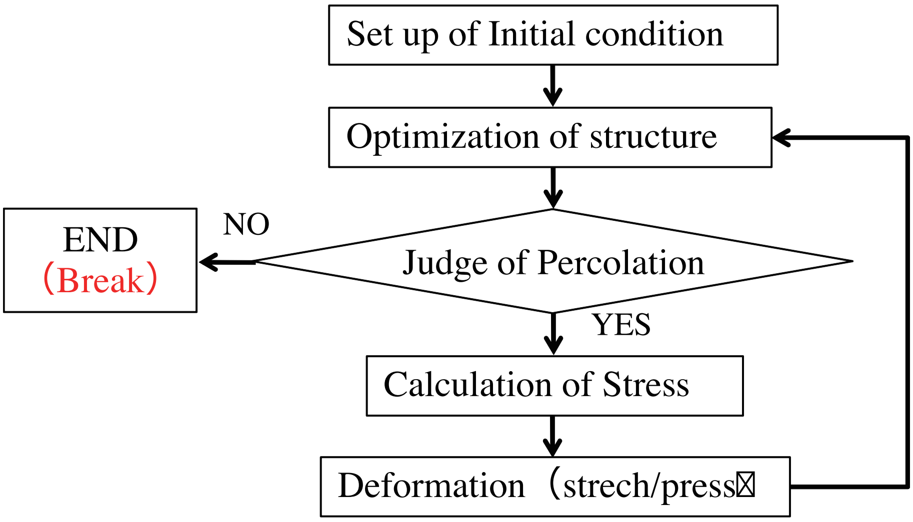

Figure 4.8: Computation scheme.

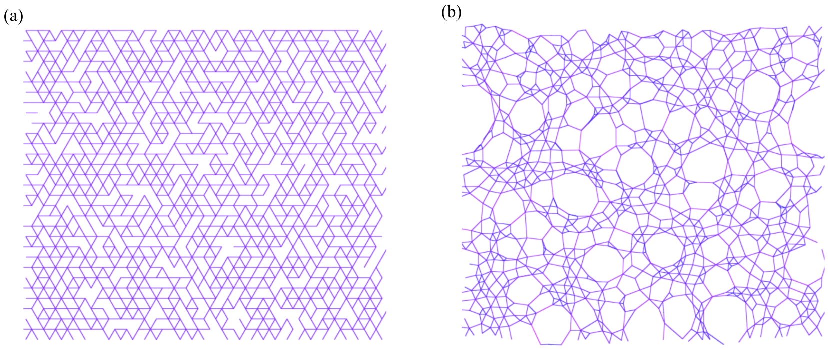

Figure 4.9: Triangular lattice at $p = 0.7$. (a) Initial network structure before the relaxation. (b) Network structure after the relaxation.

4.4.2 Experimental method

Fabrication of Tetra-PEG gels

The details of tetra-amine-terminated PEG (TAPEG) and tetra-NHS-glutarate-terminated PEG (TNPEG) preparation and characterization are reported.[17] The molecular weights (M_w) of TAPEG and TNPEG were matched to be 10 kg/mol. Constant amounts of TAPEG and TNPEG (100 g/L) were dissolved in 0.1 M phosphate buffer (pH 7.4) and incubated in constant-temperature bath at 25 °C. After 1, 5, 10, 20, 40, 60 min, two solutions were mixed rigorously, and the resulting solution was poured into the mold. It was allowed at least 24 h for the completion of the reaction before the following experiment was performed.

Reaction conversion

Tetra-PEG gels were prepared as cylinder shapes (height,10 mm; diameter, 20 mm). Thus, prepared gel samples were soaked in H_2O for 3 days at room temperature and then dried.Dried gel samples were cut into thin films (thickness, 20 μm) using a Microtome (SM2000R, Leica) and soaked in D_2O. IR spectra of swollen gel samples were obtained using an IR spectrophotometer.

Stretching measurement

The stretching measurement was carried out on the dumbbell-shaped films using a mechanical testing apparatus (Rheo Meter: CR-500DX-SII, Sun Scientific Co.) at a crosshead speed of 0.1 mm/s. The gel samples were used in the as-prepared state. Each specimen was stretched and released repeatedly two times, and the reproducibility of the results was confirmed. More than 5 samples were tested for each network concentration, and the observed moduli were arithmetically averaged.

4.5 Results and Discussion

4.5.1 Simulation

The simulation data of a triangular lattice and a diamond lattice, the tree-like theory, and the PN law are shown in Figure 4.10. As seen in Figure 4.10, the simulation data, the PN law, and the tree-like theory are numerically consistent for $p \gg p_c$. Although the tree-like theory has a serious problem that a cluster spanning the whole system cannot fit in the 3D space[13] and there is a significant difference of the network topology between this simulation and the tree like theory, the tree-like theory is a very good approximation for $p \gg p_c$. This is because any lattice including Bethe lattice satisfies eq. (4.13) in the $p \gg p_c$ region if all sites and chains are elastically effective at $p = 1$. This means that the first approximation of G around $p = 1$ does not depend on the local topology of the network structure or on the existence of loops in the system as discussed in the theoretical section.

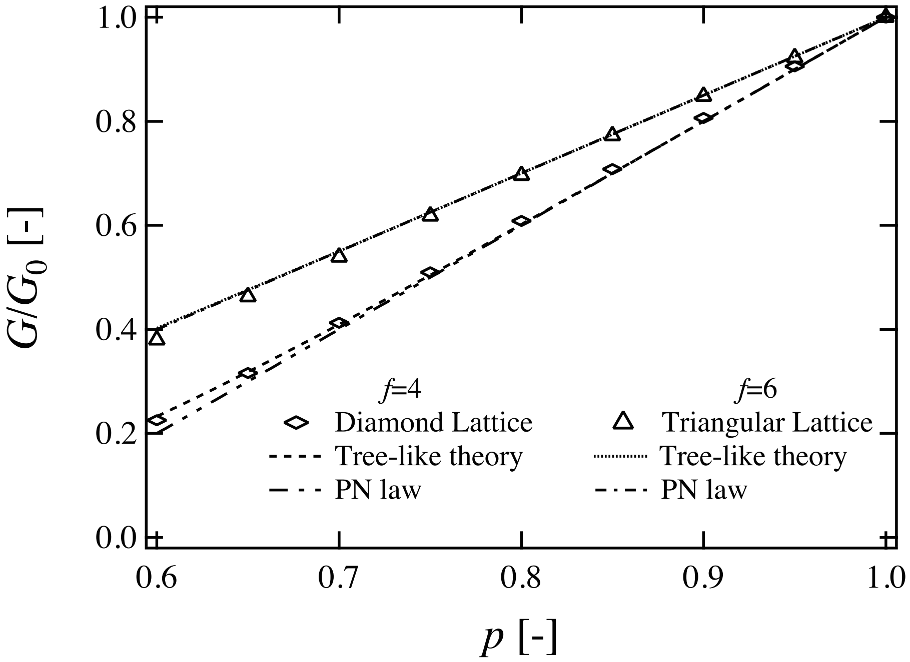

Figure 4.10: Elastic modulus of simulation data, tree-like theory, and PN law.

4.5.2 Evaluation of p

In order to examine the PN law, we conducted a real experiment with tetra-PEG gel. Tetra-PEG gel is formed by connecting two tetra-arm PEG units that have mutually reactive amine (TAPEG) and *N*-hydroxysuccinimidyl (NHS) ester (TNPEG) terminal groups through amide bond. The gelation reaction of tetra-PEG gel is as follows.[26] The important reaction of gelation in the tetra-PEG gel system is aminolysis reaction between the amine group within TAPEG and activated ester group within TNPEG.

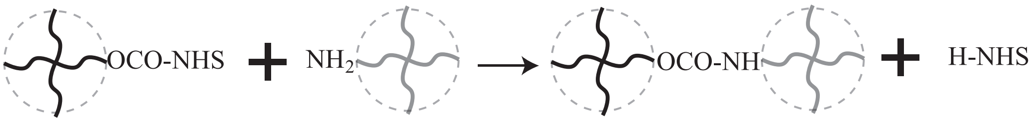

(2.1)

On the other hand, the activated ester group within TNPEG gradually dissociates in aqueous solution due to hydrolysis reaction as follows:

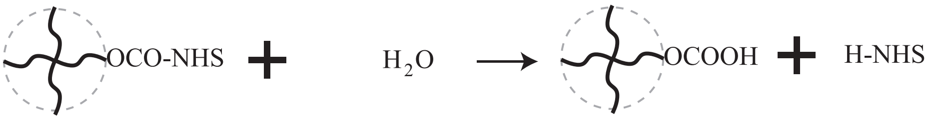

(2.2)

Some NHS esters react with amines forming amide bonds, and the others are hydrolyzed forming carboxylic acids. The reaction probability corresponds to the ratio of the concentration of amide bond to initial concentration of NHS ester.

In this study, we tuned the reaction probability by forming tetra-PEG gel with activity-tuned TNPEG. The activity of activated ester on TNPEG was tuned by hydrolyzing the activated ester prior to the initiation of gelation reaction. The experimental procedure is schematically depicted in Figure 4.2. Figure 4.11 shows the IR spectra of tetra-PEG gel obtained by subtracting those for buffer solutions. The peak intensity at 1620 cm^{-1} decreased and that at 1555 cm^{-1} increased with increasing the hydrolysis time, t. According to our previous work,[19] the former is assigned to amide bond and the latter to the ionized carbonyl group. As mentioned above, the reaction probability corresponds to the ratio of the concentration of amide bond to initial concentration of NHS ester

$$p = \frac{C_{\mathrm{amide}}}{C_{\mathrm{NHS}}} = \frac{A_{\mathrm{amide}}/\alpha_{\mathrm{amide}}}{A_{\mathrm{amide}}/\alpha_{\mathrm{amide}} + A_{\mathrm{COOH}}/\alpha_{\mathrm{COOH}}} \tag{4.21}$$

where C_{NHS}, C_{amide}, and C_{COOH} denote the initial concentration of terminal NHS ester, the concentration of the amide bond, and the carboxylic acid, respectively. In addition, α_{COOH}, α_{amide}, A_{COOH}, and A_{amide} are the molar absorbance coefficients of the carboxylic acid and the amide bond, and the absorbance of the ionized carbonyl group at 1555 cm $^{-1}$ and amide bond at 1620 cm $^{-1}$, respectively. The ratio α_{COOH} to α_{amide} was set to 1.03, following our previous study.[19] Figure 4.12 shows time course of p evaluated from IR results in Figure 4.11. p decreased with increasing degradation time, suggesting that the reaction probability was successfully and systematically tuned in the tetra-PEG gels.

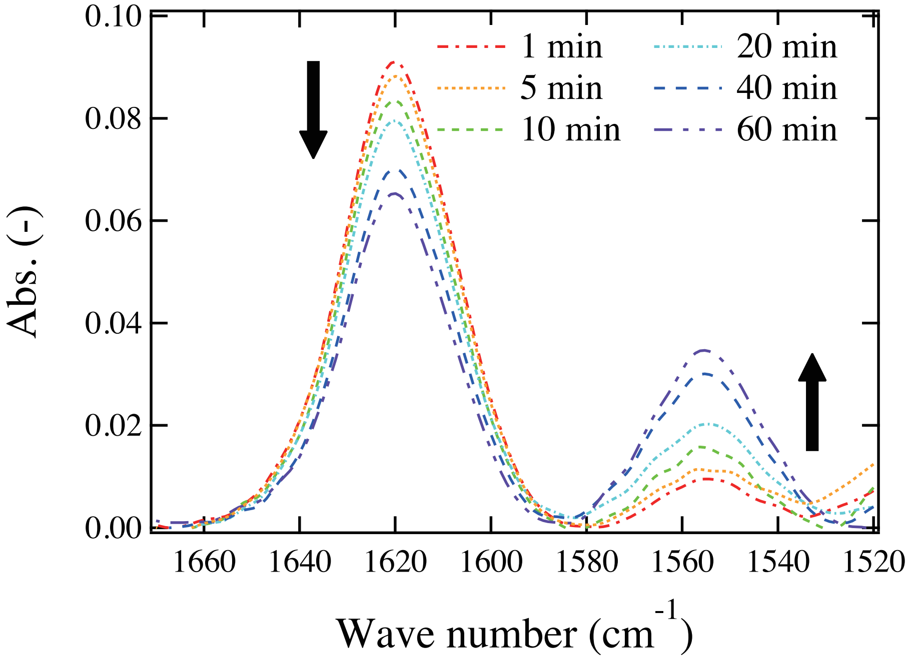

Figure 4.11: Elastic modulus of simulation data, tree-like theory, and PN law.

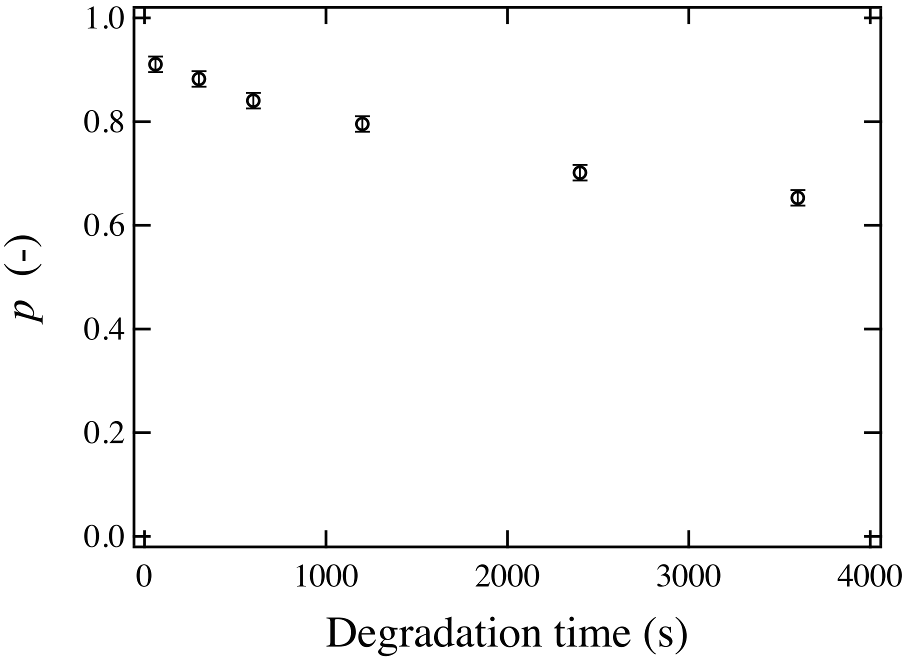

Figure 4.12: p as a function of degradation time.

4.5.3 Comparison of G predicted by the PN law with the experiment

The elastic modulus of p-tuned tetra-PEG gels and the predictions of the tree-like theory and the PN law are plotted against p (Figure 4.13). As seen in Figure 4.13, experimental data and predictions of the tree-like theory and the PN law are numerically consistent in $p \gg p_c$ region. This agreement between the experimental results and theoretical prediction strongly support the validity of the theories and the ideality of tetra-PEG gel. As mentioned above, although the tree-like theory is unrealistic because it assumes no loop, the tree-like theory is a very good approximation for $p \gg p_c$. This coincidence is not so obvious. However, it is revealed from PN law that this is because any lattice falls onto eq. (4.13) in the $p \gg p_c$ region if all sites and chains are elastically effective at $p = 1$. The difference of the network structure appears in the critical region ($p \approx p_c$), which will be discussed in our future work.

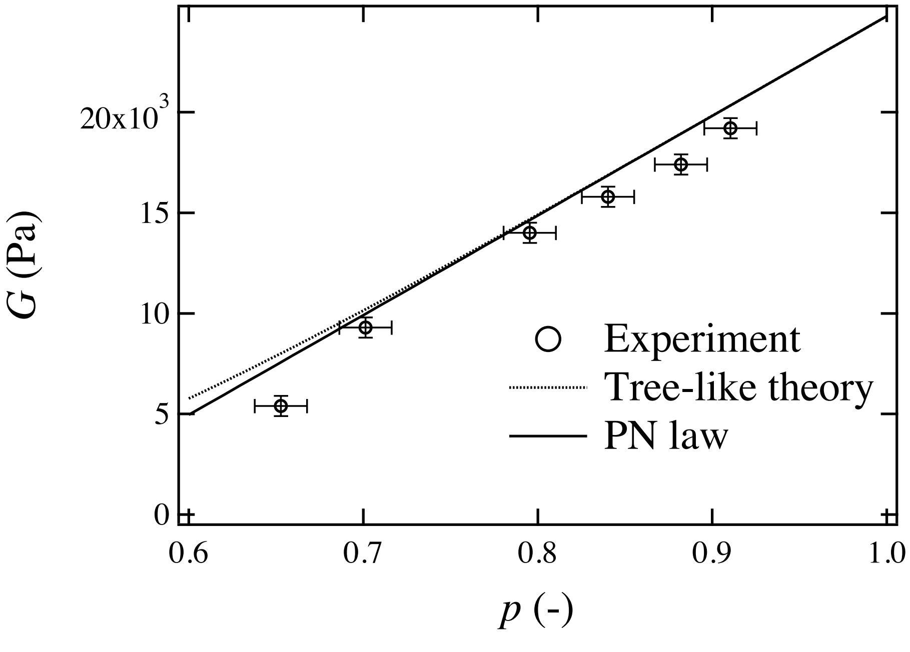

Figure 4.13: G as a function of p. Circles and line are the experimental data and the results of the PN law, respectively.

4.5.4 Applications to other systems

"PN" law can also be applied to the affine model. From the same argument as the theory section, we predict the following equations for the affine model.

$$G_{\mathrm{Af}} = \begin{cases} \left\{ \dfrac{f}{2}p + O\left((p-1)^2 \right) \right\} \dfrac{N}{V} k_{\mathrm{B}}T & (f \geq 4) \\ \left(\dfrac{9}{2}p - 3 \right) \dfrac{N}{V} k_{\mathrm{B}}T & (f = 3) \end{cases} \qquad \text{(Affine model)} \qquad (4.22)$$

These results also correspond to the first approximation around $p = 1$ for the tree-like theory. For instance, in the case of $f = 4$, the first approximation around $p = 1$ for the tree-like theory is given by

$$G_{\mathrm{Af}} = \left(2 + 2(p-1) - 6(p-1)^2 + \cdots \right) \frac{N}{V} k_{\mathrm{B}}T \quad , \qquad (4.23)$$

which correspond to eq(4.22). This agreement confirms the validity of "PN" law.

In addition, "PN" law can be also applied to networks formed by copolymerization f-functional cross-links with 2-functional polymers. For example, let us consider the case that the coordination number f is 4 and that the numbers of 4-functional precursors and 2-functional precursors per volume V are N and $2N$. An example for $f = 4$ is depicted in Figure 4.14(a). At $p = 1$, the number of elastically effective bonds and cross-links are $n = 2N$ and $m = N$, respectively. In the next step, let us cut the bond that connects site A with B (Figure 4.14(b)). As seen in Figure 4.14(b), site A is connected with 3 elastically effective bonds. So, the number of elastically effective bonds and cross-links are expected to be $n = 2N - 1$ and $m = N$, respectively. When x bonds are cut in a similar manner in the $p \geq p_c$ region, the number of elastically effective bonds and cross-links are expected to be $n = 2N - x$ and $m = N$, respectively. Using $p = \dfrac{4N - x}{4N}$, the number of elastically effective bond and cross-links are expected to be $n = 4Np - 2N$ and $m = N$, respectively. Therefore, the elastic modulus in the $p \gg p_c$ region is approximately given by

$$G_{\mathrm{Af}} \approx (4p - 2) \times \frac{N}{V} k_{\mathrm{B}}T \qquad \text{(Affine model)} \qquad (4.24)$$

$$G_{\mathrm{Ph}} \approx (4p - 3) \frac{N}{V} k_{\mathrm{B}}T \qquad \text{(Phantom model)} \quad . \qquad (4.25)$$

Here, I omit the details of calculation, but the Taylor series of the elastic modulus G around $p = 1$ for the tree-like theory is given by

$$G_{\mathrm{Af}} = \left(2 + 4(p-1) - 22(p-1)^2 + \cdots \right) \frac{N}{V} k_{\mathrm{B}}T \qquad \text{(Affine model)} \quad (4.26)$$

$$G_{\mathrm{Ph}} = \left(1 + 4\,(p-1) + 2\,(p-1)^2 + \cdots\right) \frac{N}{V} k_{\mathrm{B}} T \quad \text{(Phantom model)} \quad , \tag{4.27}$$

which correspond to eq (4.24) and (4.25). Thus these methods can be easily applied to networks formed by copolymerization f-functional cross-links with 2-functional polymers.

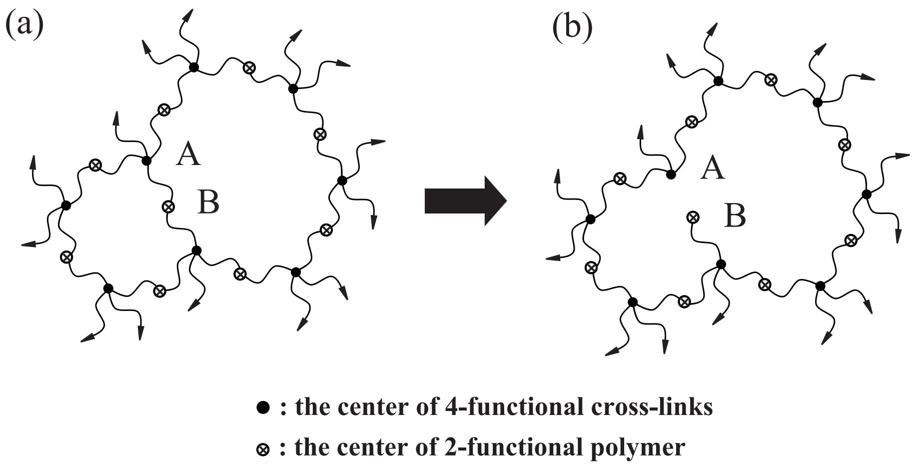

Figure 4.14: (a) A schematic picture of a network formed by copolymerization 4-functional cross-links with 2-functional polymers at $p = 1$. (b) A schematic picture after cutting the bond that connects site A with B. Sites A is connected with 3 elastically effective bonds. So the sites A is an elastically effective cross-link.

4.6 Conclusion

We investigated the relationship between G and p on polymer networks by theoretical consideration, simulation, and stretching measurement for tetra-PEG network gels. The tree-like theory was developed on an unrealistic structure, i.e., tree-like structure, where the loop is not allowed. Because of this assumption, the tree-like theory has a serious problem that a cluster spanning the whole system cannot fit in the 3D space. As a result, the tree-like theory has been open to criticism since it was proposed. In order to overcome this criticism, many studies on loops have been conducted, but a simple and general method is not well established. In this study, we try to overcome this problem and pointed out that the elastic modulus is expressed by $G = \left((fp/2-1) + O\left((p-1)^2\right)\right) N k_{\mathrm{B}} T / V$ (PN law), which does not depend on the local topology of the network structure or the existence of the loops.We confirmed the validity of the PN law from simulation and experiment. What is important in the PN law is not only that the approximate expression of G can be obtained, but also that the strong restriction put on the network structure in the tree-like theory is removed in a simple way.

References

[1] Kuhn, W., *Naturewiss.* **1936**, 24, 346.

[2] Wall, F. T., *J. Chem. Phys.* **1942**, 10, 132-134.

[3] Wall, F. T., *J. Chem. Phys.* **1942**, 10, 485-488.

[4] Wall, F. T., *J. Chem. Phys.* **1942**, 10, 527-530.

[5] James, H. M.; Guth, E., *J. Chem. Phys.* **1943**, 10, 455-481.

[6] James, H. M.; Guth, E., *J. Chem. Phys.* **1947**, 15, 669-683.

[7] Wall, F. T.; Flory, P. J., *J. Chem. Phys.* **1951**, 19, 1435-1439.

[8] Treloar, L. R. G., *The Physics of Rubber Elasticity.* Clarendon Press: Oxford, **1975**.

[9] Flory, P. J., *Principles of Polymer Chemistry.* Cornell Univ.: Ithaca, **1953**.

[10] Scanlan, J., *J. Polym. Sci.* **1960**, 43, 501-507.

[11] Case, L. C., *J. Polym. Sci.* **1960**, 45, 397-403.

[12] Miller, D. R.; Macosko, C. W., *Macromolecules* **1976**, 9, (2), 206-211.

[13] Rubinstein, M.; Colby, R. H., *Polymer Physics.* Oxford Univ. Press.: Oxford, **2003**.

[14] Stepto, R. F. T.; Cail, J. I.; Taylor, D. J. R., *Macromol. Symp.* **2000**, 159, 163-178.

[15] Dusek, K.; Gordon, M.; Ross-Murphy, S. B., *Macromolecules* **1978**, 11, (1), 236-245.

[16] Sarmoria, C.; Miller, D. R., *Computational and Theoretical Polymer Science* **2001**, 11, 113-127.

[17] Sakai, T.; Matsunaga, T.; Yamamoto, Y.; Ito, C.; Yoshida, R.; Suzuki, S.; Sasaki, N.; Shibayama, M.; Chung, U., *Macromoleules* **2008**, (41), 5379-5384.

[18] Sugimura, A.; Asai, M.; Matsunaga, T.; Akagi, Y.; Noguchi, H.; Shibayama, M., *Polymer J.*, **2011**, (45), 300-306.

[19] Akagi, Y.; Katashima, T.; Fujii, K.; Matsunaga, T.; Chung, U.; Shibayama, M.; Sakai, T., *Macromolecules* **2011**, 44, 5817-5821.

[20] Valles, E. M.; Macosko, C. W., *Macromolecules* **1979**, 12, (4), 673-679.

[21] Douglas, J. F. *Macromol. Symp.* **2010**, 291-292, 230-238.

[22] Stauffer, D.; Aharony, A., *Introduction to percolation theory.* Taylor & Fracis: **1994**; Vol. 2.

[23] de Gennes, P. G. *J. phys. lett. (Paris)* **1976**, 37, L1-L2.

[24] Kirkpatrick, S. *Rev. Mod. Phys.* **1973**, 45, (4), 574-588.

[25] Sakai, T.; Akagi, Y.; Matsunaga, T.; Kurakazu, M.; Chung, U.; Shibayama, M. *Macromol. Rapid Commun.* **2010**, 31, (22), 1954-1959.

[26] Nishi, K.; Fujii, K.; Chijiishi, M.; Katsumoto, Y.; Chung, U.; Sakai, T.; Shibayama, M. *Macromolecules* **2012**, 45, (2), 1031-1036.

Chapter 5

The approximate calculation of the elastic modulus for a entire p range

5.1 Introduction

Following Chapter 4, the aim of this chapter is to propose a new theory that approximately determines the absolute values of elastic modulus for polymer network by taking into account of loops. In Chapter 4, we theoretically pointed out the following: If the phantom network model can be applied to a polymer network and if all sites and chains in the network are elastically effective at $p = 1$, the elastic modulus of the network in the $p \gg p_c$ region can be expressed by $G/G_0 = (p - 2/f) / (1 - 2/f)$, which does not depend on the local topology of the network structure or the existence of loops. Here we define p as the bond probability, p_c being that at the gelation threshold, f as the functionality of the cross-linker, and G as the elastic modulus at a given p ($G = G_0$ for $p = 1$). We also confirmed the validity of this equation by simulations and experiments. However, there were two problems in the previous work: (1) the applicable region of the first approximation could not be defined and (2) the elastic modulus in the critical region could not be calculated.

In this study, in order to solve these problems, we propose an approximate equation to predict not only the gelation threshold, p_c, and the critical exponent but also the absolute values of elastic modulus G for $p \geq p_c$. We make comparisons of $G(p)$ between the theory and simulated results for square and cubic lattices, and between the theory and experimental results for diamond lattice, which are in good agreement.

5.2 Effective Medium Approximation

First, we focus on a region far above the gel point and apply the effective medium approximation (EMA) to bond-disordered polymer networks.[1,2] Consider a lattice with coordination number f, in which each bond is occupied with probability p. The bond is a polymer spring with elastic constant g_0. The potential under consideration is given by

$$V = \frac{g_0}{2} \sum_{\langle ij \rangle} p_{ij} [(\overrightarrow{u_i} - \overrightarrow{u_j})]^2 \quad , \tag{5.1}$$

where the angular brackets denote a sum over nearest neighbor pairs which are connected by springs with g_0 and p_{ij} is a random variable that is associated with each bond and is $0, 1$ with probability $1 - p, p$, respectively. In this study, the equilibrium state is assumed to be obtained by minimization of V with respect to $\overrightarrow{u_i}$. This assumption means the position of site can be determined so as to meet the force balance and corresponds to that of the phantom network model. According to Akagi et al.,[3] the phantom network model can be applied to polymer gels prepared at around C^*, while the affine network model to those prepared at more concentrated condition. Here, C^* is the so-called chain overlap concentration. From this point of view, this theory is applicable exclusively to polymer gels prepared at around C^* or polymer networks described by the phantom network theory.

In the EMA approach, this disordered network is replaced by a uniform effective medium of elastic constant g_m and lattice constant u_m. Consider a model shown in figure 5.1, in which we define several constants. When all the springs have elastic constant g_m, g_eff is defined as the effective spring constant of all the connections between nodes 1 and 2, including the direct connection in the uniform system, and a^* is the proportionality constant defined by $g_\mathrm{eff} = g_\mathrm{m}/a^*$. We will calculate a^* later, but let us treat it as a known constant. If the spring with constant g_m between nodes 1 and 2 is removed, then the new effective constant g'_m between nodes 1 and 2 is $g'_\mathrm{m} = g_\mathrm{m}/a^* - g_\mathrm{m}$.

Under these circumstances, let us discuss the relation between g_m and p. In order to evaluate g_m, a single bond between nodes 1 and 2 is replaced by the original bond, i.e. g_0 and 0 with probabilities p and $1 - p$, respectively. For now, a single bond between nodes 1 and 2 is replaced by the bond of the elastic constant g as an alternative to the

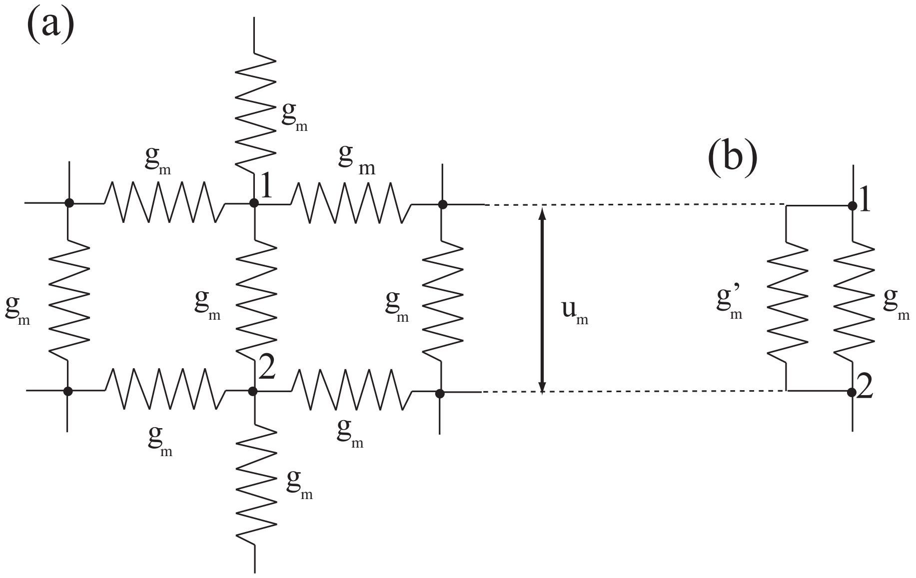

Figure 5.1: Schematic picture of the effective medium approximation. (a) The disordered network is replaced by an uniform effective medium, having the same conductance g_m between all neighboring nodes. (b) We show an equivalent circuit for the bond joining nodes 1 and 2 as described in the text.

two cases shown in figure 5.2(b). After introducing this original bond, the average distance between neighboring nodes changes to $u_{\rm m} + \delta u$. When this procedure is applied to all bonds, the ensemble average of the fluctuations δu is equal to zero. From this condition $g_{\rm m}$ is obtained.

In order to calculate δu, F is applied to nodes 1 and 2 as shown in figure 5.2(c), so as to restore their positions before g was substituted by $g_{\rm m}$. Comparing figure 5.2(a) and (c), F is given by

$$F = u_{\rm m}(g_{\rm m} - g) \quad . \tag{5.2}$$

Next, F is removed and the average distance between neighboring nodes changes by δu (see figure 5.2(b)). Comparing figure 5.2(b) and (c), F is given by

$$F = \delta u(g'_{\rm m} + g) \quad , \tag{5.3}$$

or

$$\delta u = u_{\rm m}\frac{g_{\rm m} - g}{g'_{\rm m} + g} = u_{\rm m}\frac{g_{\rm m} - g}{g_{\rm m}/a^* - g_{\rm m} + g} \quad . \tag{5.4}$$

As mentioned above, g is equal to g_0 and 0 with probabilities p and $1-p$, respectively,

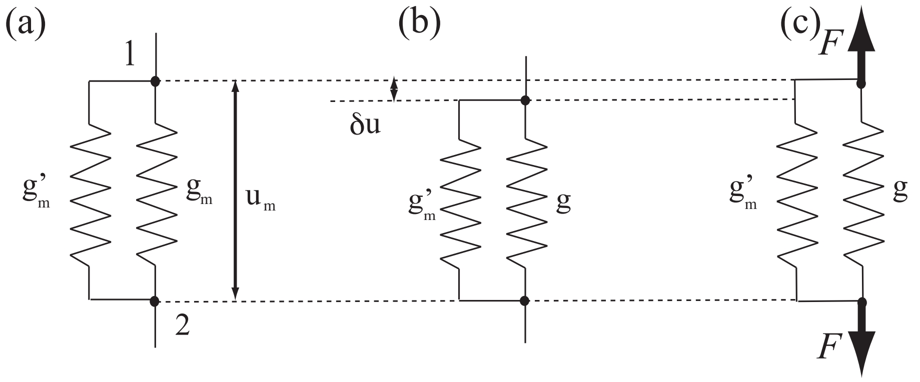

Figure 5.2: (a) Initial state (b) A single bond between nodes 1 and 2 is replaced to the bond of the elastic constant g. (c) The extra external force F is applied to keep their position at the initial state.

and the fluctuations of δu averages to zero.

$$\begin{aligned} \langle \delta u \rangle &= u_{\mathrm{m}} \int \frac{g_{\mathrm{m}} - g}{g_{\mathrm{m}}/a^* - g_{\mathrm{m}} + g} P(g) dg = 0 \ , & (5.5) \\ P(g) &= p\delta(g - g_0) + (1-p)\delta(g) \quad . & (5.6) \end{aligned}$$

By solving these equations, g_m is obtained. Here we define G as the elastic modulus at a given p (At $p = 1$, $G = G_0$). Because the ratio of g_m to g_0 is equal to the ratio of G to G_0, the elastic modulus is given by

$$\frac{G}{G_0} = \frac{g_m}{g_0} = \frac{p - a^*}{1 - a^*} \quad . \tag{5.7}$$

Here we describe two different methods to calculate a^* for polymer networks. The first is based on theories of the rubber elasticity. Note that each cross-link is allowed to move freely in this model, so the phantom network model can be applied. From Chapter 4, when all nodes and chains are elastically effective at $p = 1$ and the phantom network model can be applied to polymer networks, the elastic modulus near $p = 1$ is given by

$$\frac{G}{G_0} = \frac{p - \frac{2}{f}}{1 - \frac{2}{f}} \quad . \tag{5.8}$$

Comparing Eq.(5.7) and Eq.(5.8), we obtain $a^* = 2/f$.

The second involves applying the calculation procedure of the central-force elastic network to the polymer network.[2] Following situations of this study, a potential is expressed as

$$V = \frac{g_m}{2} \sum_{\langle ij \rangle} [(\overrightarrow{u_i} - \overrightarrow{u_j})]^2 \quad . \tag{5.9}$$

The force on the site i is given by

$$\overrightarrow{F_i} = -\frac{\partial V}{\partial \overrightarrow{u_i}} = -\sum_j D_{ij} \cdot \overrightarrow{u_j} \quad , \tag{5.10}$$

where we define the dynamical matrix D_{ij} as

$$D_{ij} = \begin{cases} -g_m & i \neq j \\ f g_m & i = j \end{cases} \quad . \tag{5.11}$$

It is easier to deal with this equation in reciprocal space. $\overrightarrow{u_i}$ can be converted by Fourier transformation to give

$$\overrightarrow{u_i} = \sum_{\overrightarrow{k}} \overrightarrow{u_k} \exp\{i \overrightarrow{k} \cdot \overrightarrow{r_i}\} \quad , \tag{5.12}$$

$$\overrightarrow{u_k} = \frac{1}{N} \sum_i \overrightarrow{u_i} \exp\{-i \overrightarrow{k} \cdot \overrightarrow{r_i}\} \quad . \tag{5.13}$$

In a similar way, the Fourier transformation of $\overrightarrow{F_i}$ is given by

$$\overrightarrow{F_i} = \sum_{\overrightarrow{k}} \overrightarrow{F_k} \exp\{i \overrightarrow{k} \cdot \overrightarrow{r_i}\} \quad , \tag{5.14}$$

$$\overrightarrow{F_k} = \frac{1}{N} \sum_i \overrightarrow{F_i} \exp\{-i \overrightarrow{k} \cdot \overrightarrow{r_i}\} \quad , \tag{5.15}$$

where $\overrightarrow{r_i}$ is the position vector of the site i in equilibrium. By using these expressions, Eqs. (5.10) can be transformed to give

$$\overrightarrow{F_k} = -D(\overrightarrow{k}) \cdot \overrightarrow{u_k} \quad . \tag{5.16}$$

Here, the dynamical constant $D(\overrightarrow{k})$ is defined as

$$\begin{aligned} D(\overrightarrow{k}) &= \sum_j D_{ij} \exp\{i \overrightarrow{k} (\overrightarrow{r_j} - \overrightarrow{r_i})\} \\ &= g_m \sum_{\hat{\delta}} [1 - \exp\{i a \overrightarrow{k} \cdot \hat{\delta}\}] \quad , \end{aligned} \tag{5.17}$$

where $\hat{\delta}$ is a unit vector in the direction of one of the f nearest neighbors and a is the lattice constant.

In order to caluculate a^*, let us apply an externally force on the bond connecting site i and j. The external force is given by

$$\vec{F_j} = F\hat{r_{12}}(\delta_{j1}-\delta_{j2}) \tag{5.18}$$

or

$$\begin{aligned}\vec{F_k} &= \sum_i \vec{F_i}\exp\{-i\vec{k}\cdot\vec{r_i}\} \\ &= F\hat{r_{12}}[\exp\{i\vec{k}\cdot\vec{r_1}\}-\exp\{i\vec{k}\cdot\vec{r_2}\}] \quad . \end{aligned} \tag{5.19}$$

From these expressions, we find

$$\begin{aligned}\vec{u_i} &= \sum_{\vec{k}} \vec{u_k}\exp\{i\vec{k}\cdot\vec{r_i}\} \\ &= -\sum_{\vec{k}} D^{-1}(\vec{k})\cdot\vec{F_k}\exp\{i\vec{k}\cdot\vec{r_i}\} \\ &= \frac{F}{N}\sum_{\vec{k}}[\exp\{i\vec{k}\cdot(\vec{r_i}-\vec{r_2})\} \\ &\qquad\qquad -\exp\{i\vec{k}\cdot(\vec{r_i}-\vec{r_1})\}]D^{-1}(\vec{k})\cdot\hat{r_{12}}\end{aligned}$$

and

$$\begin{aligned}\vec{u_2}-\vec{u_1} &= \frac{F}{N}\sum_{\vec{k}}[2-\exp\{ia\vec{k}\cdot\hat{r_{12}}\} \\ &\qquad -\exp\{-ia\vec{k}\cdot\hat{r_{12}}\}]D^{-1}(\vec{k})\cdot\hat{r_{12}} \quad . \end{aligned} \tag{5.20}$$

a^* was defined as

$$\frac{g_m}{a^*}(\vec{u_2}-\vec{u_1})\cdot\hat{r_{12}} = F \quad . \tag{5.21}$$

Therefore we obtain

$$\begin{aligned}a^* &= \frac{g_m}{N}\sum_{\vec{k}}[2-\exp\{ia\vec{k}\cdot\hat{r_{12}}\} \\ &\qquad -\exp\{-ia\vec{k}\cdot\hat{r_{12}}\}]D^{-1}(\vec{k}) \quad . \end{aligned} \tag{5.22}$$

As all bonds are equivalent, we can replace $\hat{r_{12}}$ by any of the nearest-neighbor bonds $\hat{\delta}$, sum over all bonds, and divide by Nf to give

$$a^* = \frac{2g_m}{fN^2}\sum_{\vec{k}}\sum_i\sum_{\hat{\delta}}[1-\exp\{ia\vec{k}\cdot\hat{\delta}\}]D^{-1}(\vec{k})$$

$$= \frac{2}{fN}\sum_{\overrightarrow{k}} 1$$

$$= \frac{2}{f} \quad . \tag{5.23}$$

Last, we discuss the applicable region of EMA. Following the Gintzburg criterion, the square of the fluctuations of g_{m} around the mean value is required to be sufficiently smaller than the square of the mean value itself, in order to apply the mean field approximation.

$$\left\langle (g_{\mathrm{m}} - g)^2 \right\rangle = \int (g_{\mathrm{m}} - g)^2 P(g) dg \ll g_{\mathrm{m}}^2 \tag{5.24}$$

$$\therefore \quad p \gg \frac{1}{2} + \frac{1}{f} \tag{5.25}$$

This condition corresponds to the applicable region of the first approximation. For instance, the condition is $p \gg \frac{3}{4}$ for square lattice, and $p \gg \frac{2}{3}$ for cubic lattice. Conversely, because the fluctuations of g_m is large outside this criterion, the assumption that all sites are connected with the same elastic constant g_m is not valid and EMA cannot be used.

Note that the value a^* of the central force elastic network is different from that of the polymer network, i.e., a^* for the central force elastic network equals to $2d/f$, where d is the space dimension.[2] As discussed above, the potential of the central force elastic network is proportional to the square of the displacements from equilibrium.

$$V = \frac{g_0}{2} \sum_{\langle ij \rangle} [(\overrightarrow{s_i} - \overrightarrow{s_j}) \cdot \hat{r_{ij}}]^2 p_{ij} \tag{5.26}$$

Here, $\overrightarrow{s_i}$ is the displacement from equilibrium and $\hat{r_{ij}}$ is a unit vector connecting nearest-neighbor pairs in equilibrium. Because the potential is propotional to the square of the scalar projection of the displacement vector of the cross-links after deformation onto the unit vector connecting nearest-neighbor pairs in equilibrium, a^* is dependent on the space dimension. In the case of polymer networks, since it is unnecessary to use the inner products, a^* is independent of the space dimension.

The elastic moduli of the square network and the cubic network predicted by EMA are shown in figure 5.3. We also conducted simulations to confirm the validity of this theory. Since the details of simulations are reported elsewhere,[5] we briefly show the outline of the simulations. We developed a network model of worm-like chains and introduced defects into the polymer network by randomly cutting network chains. To measure the stress-extension ratio curve of the gel, the gel is gradually stretched by the change of the aspect ratio of the simulation box with constant volume. After a small change of the aspect ratio, the gel network is relaxed to an equilibrium state. We also conducted simulations with a Gaussian chain network and obtained the same results (The data is not shown.). The results of simulation are also plotted in figure 5.3. As shown in figure 5.3, EMA gives good results when Eq.(5.25) is satisfied. However, deviation from the simulation are seen near the gel point. Because fluctuations in the effective medium become large near p_c, the assumption that all the spring have the same elastic constant g_m is not valid. This problem will be solved by a real-space renormalization transformation described in the next section.

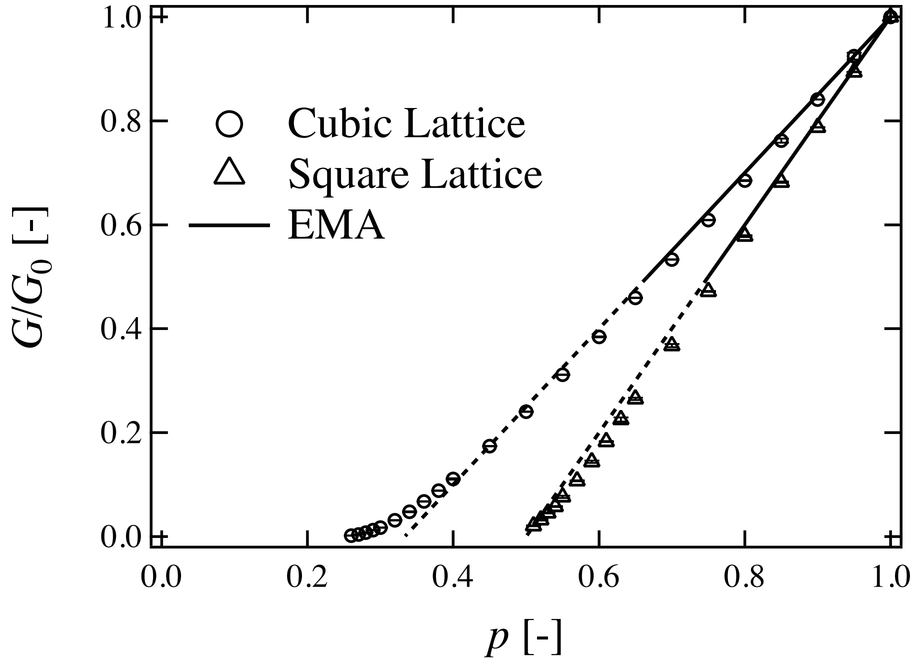

Figure 5.3: Elastic modulus of a square and cubic lattice of random polymer network.

5.3 Real-space renormalization and Effective Medium Approximation (REMA)

As a next step, we propose an approximate expression for entire range of p by following the studies of the percolation conductivity problem.[6] The main assumption of EMA is that fluctuations in the effective medium are small. If these fluctuations are large, EMA cannot be applied. In such cases, a real-space renormalization group transformation is more appropriate because this method takes into account the properties of the pre-averaged medium. Following the studies of the percolation conductivity problem,[7] the new distribution function, after one rescaling from a network having the distribution in (5.6), becomes

$$\tilde{P}(g) = [1 - R(p)]\delta(g) + \sum_{i=1}^{N} a_i(p)\delta(g - g_i) \quad . \tag{5.27}$$

Here, N is the number of possible nonzero values of g_i, the elastic constant of the cell that is chosen for renormalization transformation, and $a_i(p)$ is the probability that the value g_i occurs, $\sum_{i=1}^{N} a_i(p) = R(p)$, where $R(p)$ is the transformed probability. To calculate the elastic constant g_i of the cell, we use the phantom network model because each cross-link is allowed to move freely. Thus the spring constant of the cell g is given by

$$g = (n - m)g_0 \quad , \tag{5.28}$$

where n and m are defined as the number of elastically effective chains and elastically effective cross-links, respectively.

In principle, if one repeats the transformation several times, the network goes further and further away from criticality and we finally obtain the fixed-point distribution $\tilde{P}(g)$, the shape of which does not change under further rescaling. The elastic constant of the network can then be calculated as an average of this distribution. However, in such a case, one cannot obtain analytical expressions and it becomes necessary to employ numerical calculation. Because of these reasons, renormalization transformation is executed only once in REMA. An important merit of REMA is that one can obtain the absolute value of the elastic modulus analytically and explicitly. Moreover, as shown in the following chapters, REMA gives excellent results, including for critical behavior, simply by using a one-time renormalization transformation.

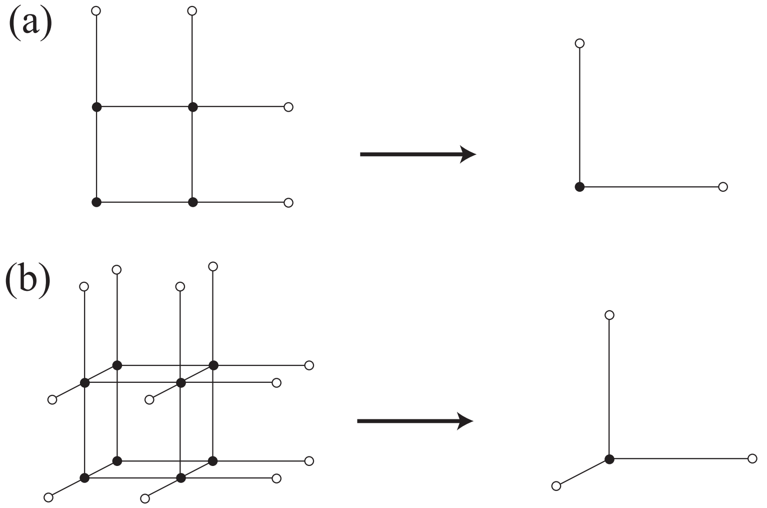

Figure 5.4: Transformation of renormalization-group cells of (a) square and (b) cubic lattice.

Because the bonds of the rescaled network are longer than the old bonds by a factor of b (where b is the scaling factor of the transformation), it is necessary to rescale of the elastic constants for the new network to replicate those in the old network. However, because we focus on the the ratio of the elastic constant at p to that at $p = 1$, the effect of the rescaling is cancelled out and is not seen explicitly. Additionally, REMA predicts a bond percolation threshold p_c as $R(p_\mathrm{c}) = 2/f$, which is a point of $g_m = 0$. As concrete examples of REMA, we consider a square and a cubic lattice, described below.

5.3.1 Square Lattice

For the square lattice, we used the cell originally proposed by Reynolds et al.[8](see figure 5.4(a)), which has been used by several authors. It preserves the self-duality of the square lattice and thus $p_\mathrm{c} = \frac{1}{2}$ is the fixed point of this transformation. If we start with the binary conductance distribution for individual bonds, the rescaled distribution $\tilde{P}(g)$ and $R(p)$ are given by

$$R(p) = p^5 + 5p^4q + 8p^3q^2 + 2p^2q^3 \tag{5.29}$$

$$\begin{aligned}\tilde{P}(g) = &\left[1 - (p^5 + 5p^4q + 8p^3q^2 + 2p^2q^3)\right]\delta(g)\\ &+p^5\delta(g-3g_0) + +5p^4q\delta(g-2g_0)\\ &+(8p^3q^2 + 2p^2q^3)\delta(g-g_0),\end{aligned} \tag{5.30}$$

where $q = 1 - p$. Figure 5.5 shows the simulation and REMA results on the square lattice. As seen in the figure, the REMA results are in good agreement with the simulation data. REMA predicts $p_{\mathrm{c}} = 1/2$, which corresponds to the exact value of the critical point for a square lattice.[9] As Sahimi et al. pointed out,[2] it is possible to use REMA to estimate the exponent by analyzing the elastic modulus curve, even for small renormalization cells. Regarding critical behavior, the elastic modulus scales as $G \sim (p - p_{\mathrm{c}})^{1.16}$ for simulation and $G \sim (p - p_{\mathrm{c}})^{1.17}$ for REMA from the fitting analysis. These results are close enough to the simulation results of Feng et al., where $G \sim (p - p_{\mathrm{c}})^{1.2}$.[10] Therefore, it is confirmed that REMA gives good absolute values of the elastic modulus, including in the critical region.

5.3.2 Cubic Lattice

Figure 5.4(b) shows the cell we used for the simple cubic calculation, also used by Bernasconi.[11] It is a three-dimensional version of the cell used for the square lattice. The renormalization transformation for this cell is given by

$$\begin{aligned}
R(p) &= p^{12} + 12p^{11}q + 66p^{10}q^2 + 220p^9q^3 + 493p^8q^4 \\
&+ 776p^7q^5 + 856p^6q^6 + 616p^5q^7 + 238p^4q^8 \\
&+ 48p^3q^9 + 4p^2q^{10} \qquad (5.31)
\end{aligned}$$

$$\begin{aligned}
\tilde{P}(g) &= [1 - R(p)]\,\delta(g) + p^{12}\delta(g - 8g_0) \\
&+ 12p^{11}q\delta(g - 7g_0) + 66p^{10}q^2\delta(g - 6g_0) \\
&+ (220p^9q^3 + 4p^8q^4)\delta(g - 5g_0) \\
&+ (481p^8q^4 + 32p^7q^5)\delta(g - 4g_0) \\
&+ (8p^8q^4 + 696p^7q^5 + 116p^6q^6 + 4p^5q^9)\delta(g - 3g_0) \\
&+ (40p^7q^5 + 652p^6q^6 \\
&\qquad + 212p^5q^9 + 22p^4q^{10})\delta(g - 2g_0) \\
&+ (8p^7q^5 + 88p^6q^6 + 400p^5q^9 + 216p^4q^{10} \\
&\qquad + 48p^3q^{11} + 4p^2q^{12})\delta(g - g_0). \qquad (5.32)
\end{aligned}$$

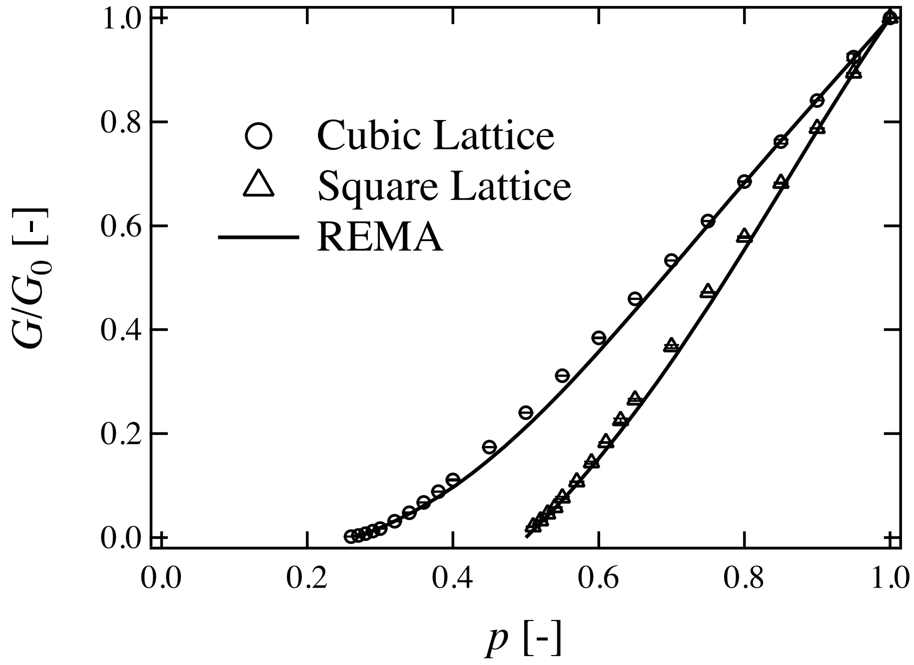

Figure 5.5: Elastic modulus of a square and a cubic lattices of random polymer network.

Figure 5.5 shows the simulation and REMA results on the cubic lattice. As seen in the figure, the REMA method gives good results. REMA yields $p_c \simeq 0.265$ in good agreement with the exact value $p_\mathrm{c} \simeq 0.249$.[9] From the fitting analysis, the elastic modulus scales as $G \sim (p - p_\mathrm{c})^{1.60}$ for simulation and $G \sim (p - p_\mathrm{c})^{1.58}$ for REMA around the critical point. These exponents are sufficiently close to the simulation results of Feng et al.[10] From these results, it is ascertained that REMA predicts good absolute values of the elastic modulus for the entire p region.

5.4 Comparison with experimental data

Finally, let us examine the theory with experimental results. We carried out mechanical testing experiments on a p-tuned Tetra-PEG gel. Here, p-tuned Tetra-PEG gels are Tetra-PEG gels, in which the reation probability p was precisely tuned. Tetra-PEG gels are formed by A-B type cross-end coupling of two tetra-arm poly(ethylene glycol) (PEG) units that have mutually reactive amine (TAPEG) and activated ester (TNPEG) terminal groups.[4] The details of experiments are reported elsewhere.[14] In this experiment, we prepare a series of p-tuned tetra-PEG gel networks by forming Tetra-PEG gel with activity-tuned TNPEG. Here, TNPEG has activated ester group, i.e., N-hydroxysuccinimidyl (NHS) ester (TNPEG) at chain end. The activity of the activated ester on TNPEG was tuned by partial hydration prior to the initiation of gelation reaction. The experimental data on a p-tuned Tetra-PEG gel were taken from our previous study.[14] Since Tetra-PEG gels are considered to have an ideal diamond structure, we also conducted simulations and made equations for the diamond lattice. As far as we know, there is no real space renormalization approach for a diamond lattice. Therefore, we used cluster approximation in reference to Yuge[12] and Vogel et al.[13] as shown in figure 5.6 with second best. In order to describe the elastic modulus at p's much closer to the critical point, we may need to select a bigger cell or conduct renormalization transformation several times. However, we avoid getting involved in this problem at this time because this cell gives a good result as seen in figure 5.7.

The elastic moduli of p-tuned Tetra-PEG gels and the diamond lattice are plotted against p in figure 5.7 and 5.8 together with the predictions of EMA and REMA. As seen in figure 5.7 and 5.8, the predictions of EMA and REMA well reproduce the results of experimental and simulation data. This agreement strongly supports the validity of the theories and ideality of Tetra-PEG gels. As shown in figure 5.7, we cannot conduct experiments near the critical point because of the experimental uncertainty. In order to examine the critical exponents and the gelation point, we need to conduct another experiment, which will be discussed in our future work.

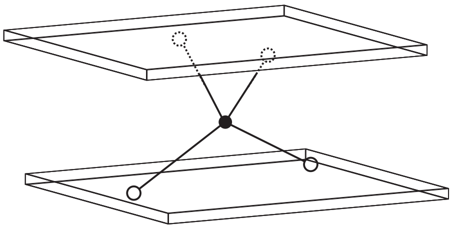

Figure 5.6: Transformation of a renormalization-group cell of a diamond lattice.

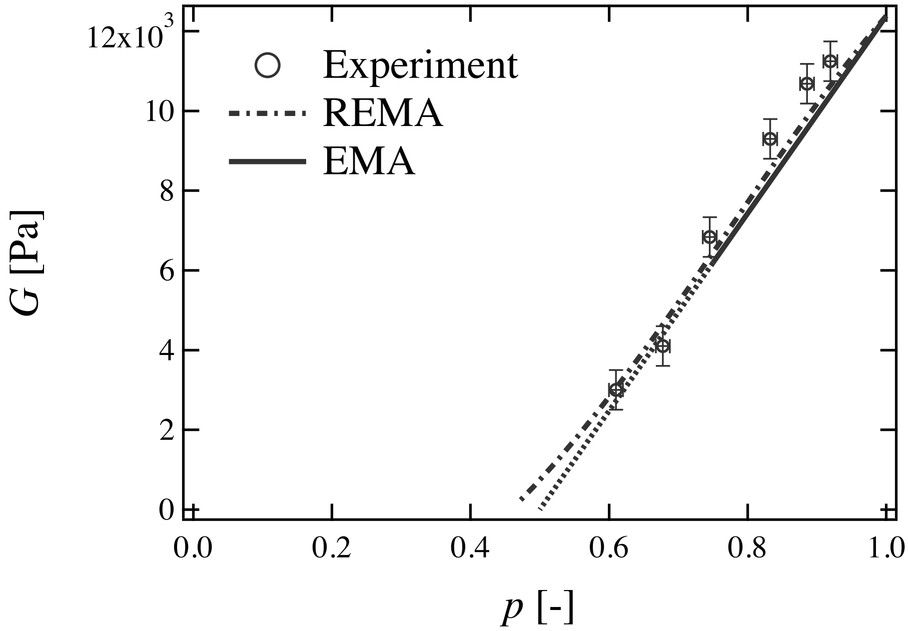

Figure 5.7: Elastic modulus of Tetra-PEG gel.[14] The solid line satisfies the Gintzburg criterion.

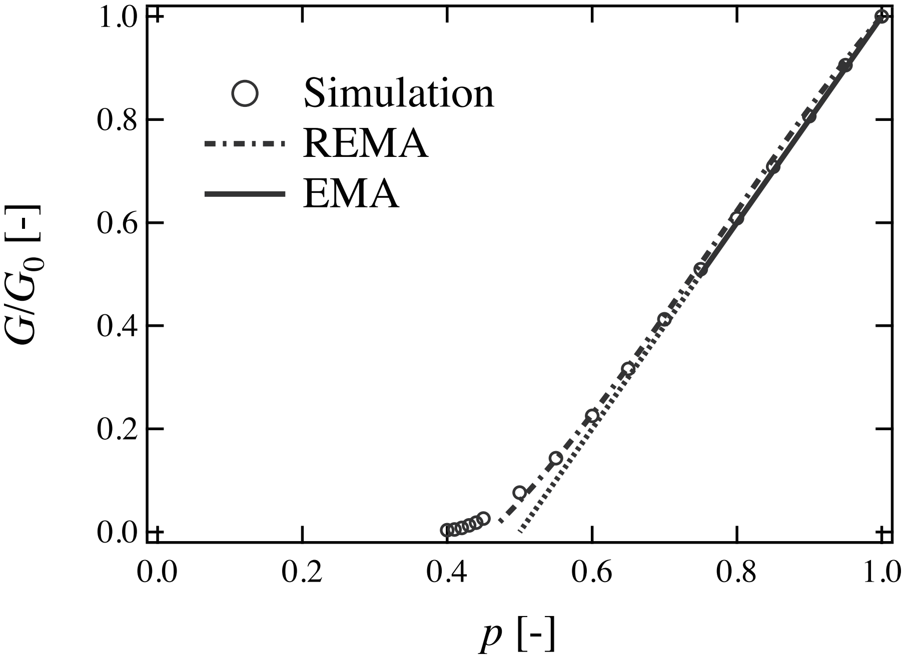

Figure 5.8: Elastic modulus of diamond lattice. The solid line satisfies the Gintzburg criterion.

5.5 Conclusion

We developed new methodologies to relate the elastic modulus of polymer networks with their structures for a given reaction probability. The results are summarized as follows.

(1) We apply the effective medium approximation (EMA) to the polymer network and predict the theoretical elastic modulus. In addition, the applicable region of the first approximation is determined from the Gintzburg criterion, i.e., $p \gg 1/2 + 1/f$.The prediction of EMA gives an an excellent agreement with those obtained by simulations of square and cubic lattices for p's satisfyng the Gintzburg criterion.

(2) In order to predict the behavior near p_c, we combine the real space renormalization and EMA, i.e., REMA. The predicted elastic modulus by REMA is also in excellent agreement with simulation results for square and cubic lattices not only in the exponents but also in the absolute values for $p \geq p_c$.

(3) We further carried out mechanical testing experiments on p-tuned Tetra-PEG gels. A comparison with experimental results of p-tuned Tetra-PEG gels was made and it confirmed the validity of this theory.

It should be noted that these theories could predict not only the critical gelation point and the scaling laws of the critical behavior but also the absolute values of the elastic modulus. Moreover, the predicted values precisely correspond to the experimental results. These methodologies are robust and applicable to any types of lattices.

References

[1] Kirkpatrick, S., *Rev. Mod. Phys.*, **1973**, 45, (4), 574-588.

[2] Feng, S.; Thorpe, M. F.; Garboczi, E., *Phys. Rev. B*, **1985**, 31, (1), 276-280.

[3] Akagi, Y.; Katashima, T.; Fujii, K.; Matsunaga, T.; Chung, U. I.; Shibayama, M.; Sakai, T.; *Macromolecules*, **2011**, 44, 5817-5821.

[4] Sakai, T.; Matsunaga, T.; Yamamoto, Y.; Ito, C.; Yoshida, R.; Suzuki, S.; Sasaki, N.; Shibayama M.; Chung, U. I., *Macromolecules*, **2008**, 41, 5379-5384.

[5] Sugimura, A.; Asai, M.; Matsunaga, T.; Akagi, Y.; Noguchi, H.; Shibayama, M., *Polymer Jounal*, **2011**, (45), 300-306.

[6] Sahimi, M.; Hughes, B. D.; Scriven, L. E.; Davis, H. T., *Phys. Rev. B*, **1983**, 28, (1), 307-311.

[7] Stinchcombe, R. B.; Watson, B. P., *J. Phys. C : Solid State Phys.*, **1976**, 9, 3221-3247.

[8] Reynolds, P. J.; Stanley, H. E.; Klein, W. *J. Phys. C: Solid State Phys.*, **1977**, 10, L167-L172.

[9] Stauffer, D.; Aharony, A., *Introduction to percolation theory.* Taylor & Fracis: **1994**; Vol. 2.

[10] S. Feng, and P. N. Sen, Phys. Rev. Lett. **52** (3), 216 (1984).

[11] Bernasconi, J. *Phys. Rev. B*, **1978**, 18, (5), 2185-2191.

[12] Yuge, Y., $J.Phys.A : Math.Gen.$, **1979**, 12, 2509.

[13] Vogel, E. E.; Lebrecht, W.; Valdes, J. F., $PhysicaA$, **2010**, 389, 1512.

[14] Akagi, Y.; Katashima, T.; Sakurai, H.; Chung, U. I.; Sakai, T., $RSCAdvavces$, **2013**, 3, 13251-13258.

Chapter 6

Structural analysis of static inhomogeneity in Tetra-PEG gel

6.1 Introduction

The existence of large-scale polymer concentration fluctuations in polymer gels has been brought to attention by small-angle light and neutron scattering, because it is a clear distinction from polymer solution and influence physical properties of gels and rubbers.[1–6] However, large-scale inhomogeneities have not been well understood because systematical data about large-scale inhomogeneities have not been obtained. In general, there are various types of inhomogeneities, such as spatial, topological, connectivity, and mobility inhomogeneities, as classified by one of the authors, and these inhomogeneities complicatedly affect the scattering function.[7] In order to understand the inhomogeneities, it is necessary to prepare homogeneous network and introduce the inhomogeneities systematically into the network.

There has been no success in preparing defect-free networks so far. One of the typical examples of a model network was end-coupling of telechelic polymer having a sharp molecular weight distribution by multifunctional cross-linker, which is called "end-linked network".[8–12] Mendes et al.[13] prepared the end-linked polystyrene network and compare SANS profiles of the gels to the corresponding semidilute solutions of linear chains. It was shown from the SANS results that gels scatter a signal at small angles much stronger than the equivalent solutions, which indicates the presence of large heterogeneities in the gel. In addtion, Shibayama et al.[14–17] conducted SANS measurement on the end-linked poly(tetrahydrofuran) gel and also observed an upturn in the scattering intensity at low q region, where q is the magnitude of the scattering vector.

Sakai et al.[18] developed a novel class of hydrogels by "cross-end coupling" of two types of tetra-arm polyethylene glycol (PEG) units that have mutually reactive amine (TetraPEG-NH_2) and activated ester (TetraPEG-NHS) terminal groups, respectively. These gels, hereafter called TetraPEG gels, have various advantages, namely, high mechanical strength and toughness, easy preparation, and biocompatibility. it was found from SANS measurement on Tetra-PEG gel that upturns in low q regions ($q < 0.01\text{Å}^{-1}$) are weak, and thus Tetra-PEG gels have a near-ideal network.[19–21,31] Furthermore, as presented in our previous section, the important thing is that we can systematically introduce the inhomogeneities into homogeneous networks.[23]

The aim of this study is to understand inhomogneities in polymer networks by using Tetra-PEG gel. Here, we systematically introduced two types of inhomogeneieties into the Tetra-PEG gel, and carried out detailed SANS studies on these gels. Firstly, we prepared defect-rich networks by reducing primary molecular concentration, and conducted a time-resolved SANS measurement to monitor the evolution of polymer network structure. Secondly, we prepared a series of p-tuned Tetra-PEG gel networks by forming Tetra-PEG gel with activity-tuned TNPEG. In both cases, we introduce a parameter p for the reaction probability ($0 \leq p \leq 1$) that indicates the degree of connectivity defects. The activity of the activated ester on TNPEG is tuned by partial hydration prior to the initiation of gelation reaction (Figure 6.1). After the p-tuned gels were swollen and sol components were removed from the gels, we conducted SANS measurement. The SANS results were discussed from various viewpoints.

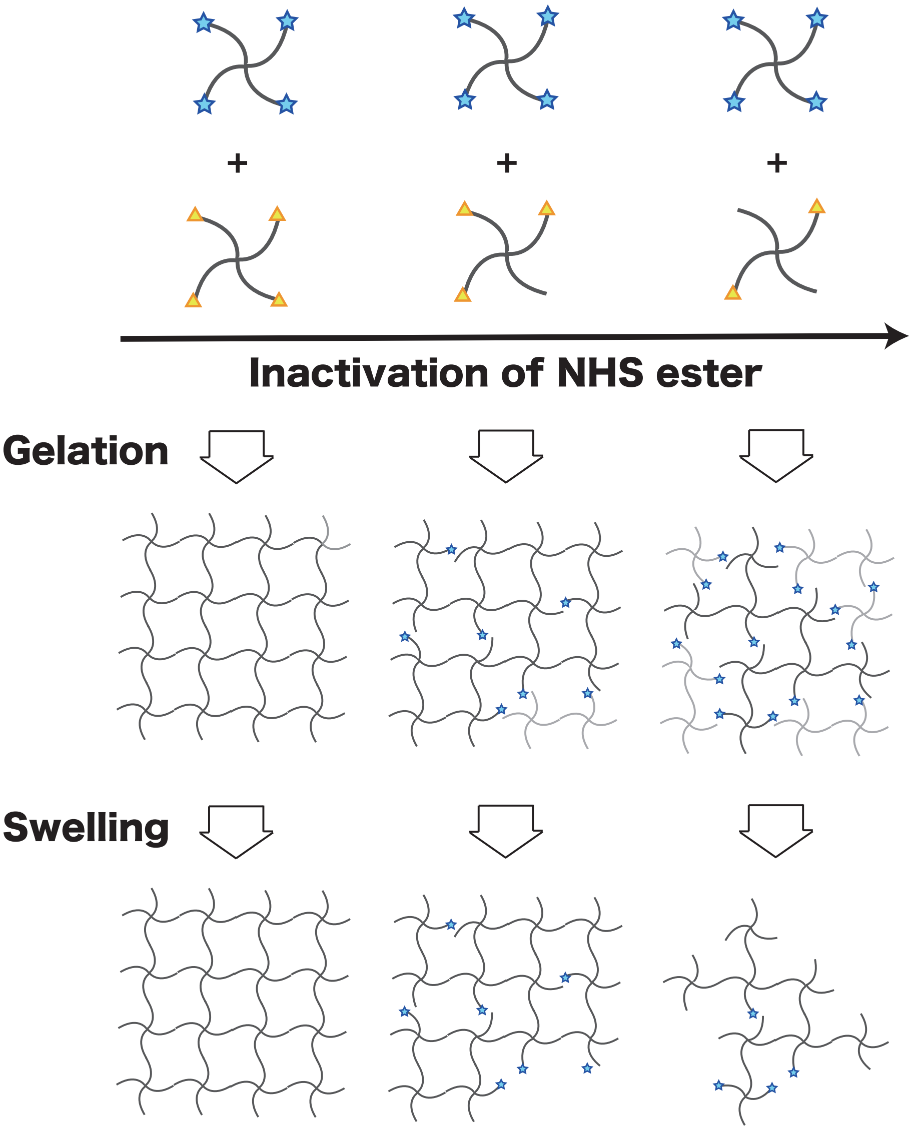

Figure 6.1: The schematic of sample preparation for *p*-tuned gels. Two kinds of tetra-arm PEG prepolymers, TAPEG and TNPEG (top). The stars and triangles represent the amino and NHS ester terminal groups, respectively. By dissolving TNPEG in water, the NHS ester groups on TNPEG were hydrolyzed progressively with time. By controlling the time for hydrolysis, the number of reactive sites is tuned. Then, TAPEG was added to prepare *p*-tuned gels (middle). After completion of gelation, the gels are swollen for the experiments (bottom).

6.2 Experiment

6.2.1 Fabrication of p-tuned Tetra-PEG gels

The details of tetra-amine-terminated PEG (TAPEG) and tetra-NHS-glutarate-terminated PEG (TNPEG) preparation and characterization are reported elsewhere.[18] The molecular weights (M_w) of TAPEG and TNPEG were matched to be 10 kg/mol. Constant amounts of TAPEG and TNPEG (100 g/L) were dissolved in 0.1 M phosphate buffer (pH 7.4) and incubated in constant-temperature bath at 25 °C. After 1, 5, 10, 20, 40, 60 90 min, two solutions were mixed rigorously, and the resulting solution was poured into the mold. It was allowed at least 24 h for completion of the reaction before the following experiments were performed.

6.2.2 Reaction conversion for p-tuned Tetra-PEG gel

Tetra-PEG gels were prepared as cylinder shapes (height, 10 mm; diameter, 20 mm). Thus prepared gel samples were soaked in H_2O for 3 days at room temperature and then dried. Dried gel samples were cut into thin films (thickness, 20 μm) using a Microtome (SM2000R, Leica) and soaked in D_2O. IR spectra of swollen gel samples were obtained using an IR spectrophotometer.

6.2.3 UV measurement for gelation reaction.

The reaction rate for gelation reaction was estimated by UV spectromether (JASCO V-630, Nihon-bunko, Japan). The ATR cell was kept at 20 °C throughout the entire experiment. From this point forward, the Tetra-PEG gels formed from primary polymers with M_w = 10 kg/mol and 20 kg/mol are named Tetra10K and Tetra20K, respectively. We carried out measurements at 120 seconds intervals on two different samples, i.e. Tetra10K and Tetra20K. A constant amount of TAPEG and TNPEG (180 mg) were dissolved in 3 mL of phosphate buffer solution (PB; 0.2 M, pH 7). The two solutions thus obtained were mixed in a 50 mL Falcon tube for 30 s at 20 °C and poured into the UV cell. As Miron reported,[26] there is the absorbance of dissociated NHS at around 260 nm. In our experiments, because the peak tops are saturated, the absorbance of the solution is read at 290 nm for Tetra10K (60 g/L) and 283 nm for Tetra20K (60 g/L), respectively.

6.2.4 Small-Angle Neutron Scattering (SANS)

We conducted SANS experiments at two different facilities. Gelation experiments were carried out on a 2D SANS instrument, SANS-U, at the University of Tokyo, located at JRR-3 Research Rector, Japan Atomic Energy Agency, Tokai, Ibaraki, Japan. A monochromated cold neutron beam with an average neutron wavelength of 7.00 Å and 10% wavelength distribution was irradiated to the samples. The scattered neutrons were counted with a 2D position detector (Ordela 2660N, Oak Ridge). The sample-to-detector distances were chosen to be 4 m. We carried out SANS measurements on two different samples, i.e. Tetra10K and Tetra20K. Constant amounts of TAPEG and TNPEG (60 g/L) were dissolved in 0.2 M phosphate buffer (pH 7.0). The gelation reaction was started by mixing each of 3 mL TAPEG and TNPEG primary polymer solutions in a sample cell, and time-resolved SANS (TR-SANS) measurements were performed during gelation process. Each measurement time was 120 s for Tetra10K (60 g/L) and 60s for Tetra20K (60 g/L), respectively. After necessary corrections for open beam scattering, transmission, and detector inhomogeneities, the corrected scattering intensity functions were normalized to the absolute intensity scale with a polyethylene secondary standard. The details of the instrument are reported elsewhere.[27]

SANS experiments on *p*-tuned Tetra-PEG gels were carried out on High-flux Advanced Neutron Application Reactor (HANARO) located at Korea Atomic Energy Research Institute (KAERI), Korea. A monochromated cold neutron beam with an average neutron wavelength 6.00 Å was irradiated to the samples. The scattered neutrons were counted with a 2D detector. The sample-to-detector distances were chosen to be 3 m and 17.5 m. We prepared two pieces of gels for each degradation time. We conducted SANS measurement on one sample at as-prepared state, and the other sample at equilibrium-swollen state with D_2O. After necessary corrections for open beam scattering, transmission, and detector inhomogeneities, corrected scattering intensity functions were normalized to the absolute intensity scale.

6.3 Results and Discussion

6.3.1 Gelation process

As describe in Experimental section, the Tetra-PEG gels formed from primary polymers with M_w = 10 kg/mol and 20 kg/mol are named Tetra10K and Tetra20K, respectively. In order to estimate the time evolution of reaction extent during the gelation process, UV measurements are conducted. Figure 6.2(a) and (b) show the time evolution of dissociated NHS for Tetra10K (60g/L) and Tetra20K (60 g/L), respectively. It was found that the concentration of dissociated NHS increases as the gelation proceeds. The fit result using eqs (2.6) and (2.7) is also shown in Figure 6.2. Here, we set k_{deg} as a fixed parameter obtained by the degradation analysis as discussed in our previous work.[25] The fit worked well from the initiation to nearly completion of reaction. By using k_{gel} obtained from fitting analysis, the concentration of amide bonds is calculated, the result of which is also dotted in Figure 6.2. From these results, the time variation of reaction extents is estimated.

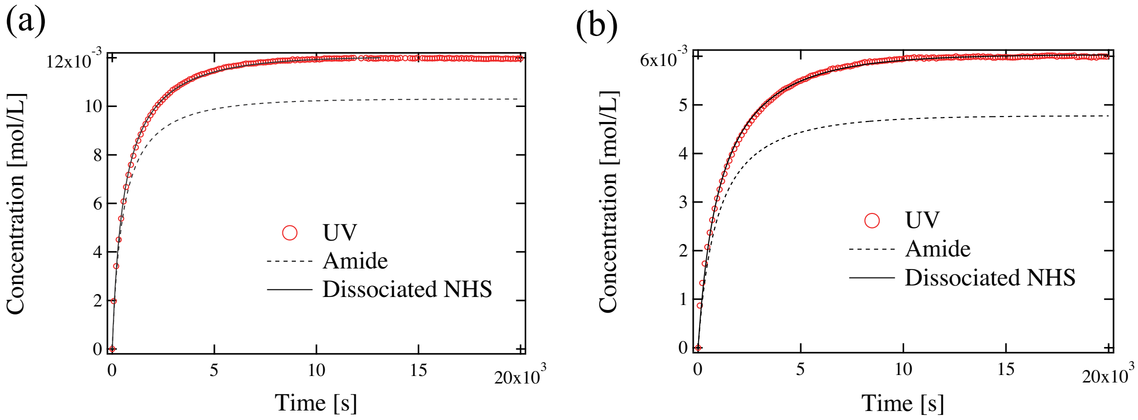

Figure 6.2: Kinetic trace obtained for the gelation of (a) Tetra10K (60 g/L) and (b) Tetra20K (60 g/L) as a function of t. The dashed and solid lines are fit for amide and dissociated NHS groups with eqs (2.6) and (2.7).

Figure 6.3 shows the time evolution of SANS curves during the gelation process for (a) Tetra10K (60 g/L) and (b) Tetra20K (60 g/L). (In terms of polymer volume fraction, the concentration equals to $\phi = 0.050$.) Because overlapping polymer volume fractions (ϕ^*) for primary polymers with M_w = 10 kg/mol and 20 kg/mol are estimated to be 0.062 and 0.035 from the previous work by Akagi et al.,[29] $\phi = 0.050$

is below ϕ^* for 10 kg/mol primary polymer, and above ϕ^* for 20 kg/mol primary polymer. As shown in Figure 6.3(a), the scattering intensity increased as the reaction proceeds. On the other hand, the scattering function scarcely changed in Figure 6.3(b). To evaluate the network structure quantitatively, we carried out curve fitting analysis for the observed SANS functions. We used the following Ornstein-Zernike function as a fitting function.

$$I\left(q\right) = \frac{I_0}{1+\xi^2 q^2} + I_{\mathrm{inc}} \quad . \tag{6.1}$$

Here, ξ is the correlation length and I_{inc} is the incoherent scattering intensity. The incoherent scattering intensity is fixed during the gelation process at 0.1 cm^{-1}, which was obtained from fitting analysis for the data at 120 s in Figure 6.3(a). The solid lines in Figure 6.3(a) and (b) represent fitting curves with OZ functions (eq 6.1). All the curves for gels are nicely fitted with the function.

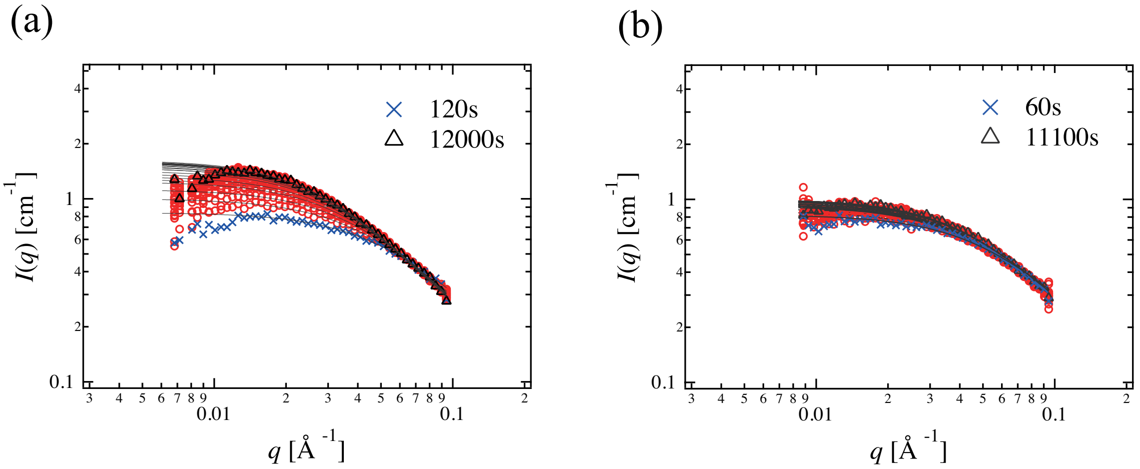

Figure 6.3: The time evolution of SANS results during the gelation process of Tetra-PEG gel of (a) Tetra10K (60 g/L) for every 480 s and (b) Tetra20K (60 g/L) for every 600 s. The solid lines denote the results of curve fit with OZ function. In order to avoid overlap, only a few sets of data together with the first (crosses) and last data (triangles) are shown.

The obtained ξ and I_0 are shown in Figure 6.4. Note that the reaction extent, which is calculated from Figure 6.2, is set as the x-axis of Figure 6.4. As shown in Figure 6.4, ξ and I_0 for $\phi < \phi^*$ (Tetra10K, 60 g/L) increases, but ξ and I_0 for $\phi > \phi^*$ (Tetra20K, 60 g/L) are constant with increasing the reaction extent. The gelation mechanisms conjectured from the SANS results are schematically shown in Figure 6.5. Because primary polymers do not overlap in $\phi < \phi^*$ region, sparse polymer networks are formed with some primary polymer aggregates as depicted in Figure 6.5. Because the segment density fluctuations increase with increasing the degree of aggregation, ξ and I_0 are considered to increase. On the other hand, in $\phi > \phi^*$ region, because gels are formed by simply connecting neighbor primary polymers, the SANS profiles do not change during the gelation process. In addition, although the correlation length ξ diverges at the transition point in the case of a critical phenomenon of gas-liquid phase transition, such behavior was not observed in the gelation process. This is because the voids around an infinite cluster are filled with the sol component, i.e., finite clusters, and the concentration fluctuations are suppressed by the sol component. A similer phenomenon was also observed from DLS measurement by J. E. Martin.[30] As shown in their DLS results on the gelation process of TMOS, the cooperative diffusion, which is related to the correlation length through $D_{\text{coop}} = k_B T / 6\pi\eta\xi$, is not sensitive to the connectivity divergence, either. In cooperative diffusion, the derivative of the osmotic pressure Π with respect to the concentration c, $\partial\Pi/\partial c$, provides the restoring force, and the sedimentation coefficient s, due to the viscous flow of the solvent through the incipient network, provides the friction; thus $D_{\text{coop}} = s\partial\Pi/\partial c$. Since neither of these terms is sensitive to the long-range connectivity that develops at the sol-gel transition, it is reasonable to expect the cooperative diffusion coefficient to vary smoothly throughout the sol-gel transition.

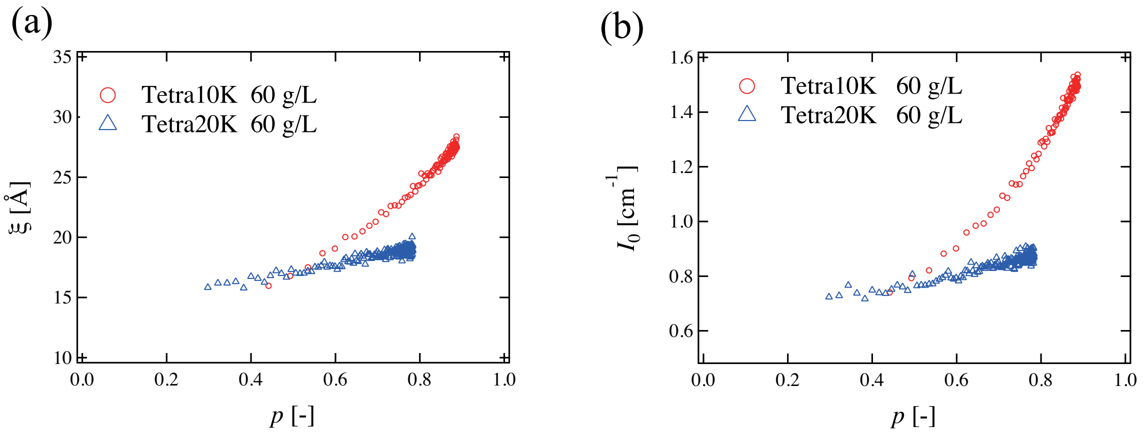

Figure 6.4: p dependence of (a) the correlation length, ξ and (b) the zero-angle extrapolated intensity $I(0)$ estimated from fitting analysis of OZ function for Tetra10K (circles) and Tetra20K (triangles).

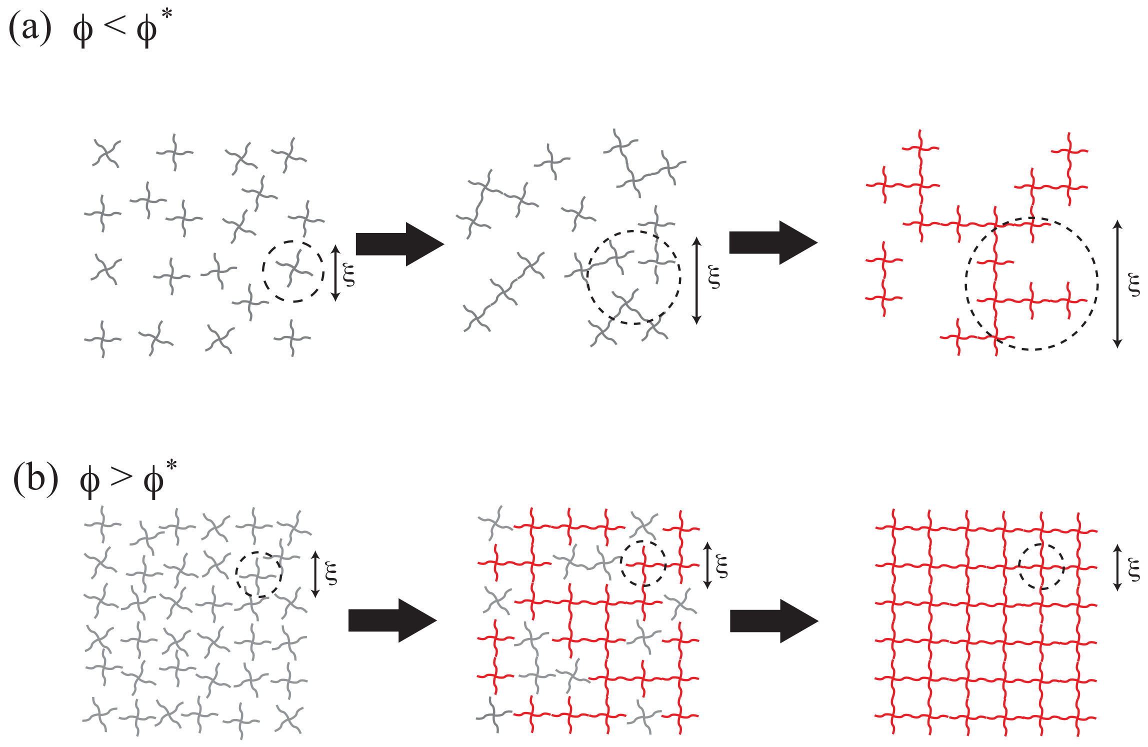

Figure 6.5: Schematical representation of the structure of Tetra-PEG gels for (a) the $\phi < \phi^*$ region and (b) the $\phi > \phi^*$ region.

6.3.2 p-tuned gels

In the previous section, we reported that the voids of an infinite cluster cannot be observed and the correlation length ξ does not diverge at the gelation point because the voids of an infinite cluster are filled with the sol component and the concentration fluctuations of polymers are suppressed. So, we prepare p-tuned gels and remove finite clusters by soaking in water as a next step. We prepared a series of p-tuned Tetra-PEG gel networks by forming Tetra-PEG gel with activity-tuned TNPEG. The activity of the activated ester on TNPEG is tuned by partial hydration prior to the initiation of gelation reaction (Figure 6.1). After the p-tuned gels are swollen and sol components are removed from the gels, we conducted SANS measurement.

SANS profiles for p-tuned gels at as-prepared state and at swollen state are shown in Figure 6.6(a) and (b). Incoherent scattering subtraction was made by fitting the observed scattering functions with OZ functions in Figure 6.6(a) and (b). The reaction propbability, p, is estimated from IR measurement as described in section In Figure 6.6(a), SANS profiles do not vary at as-prepared state though p varies from 91 % to 56 %. As for Figure 6.6(b), as p decreases, the "shoulder" at about $q = 0.03 - 0.04\text{Å}^{-1}$ shifts to the lower q-range and a strong increase of intensity can be observed at about 10^{-2}Å^{-1}. To evaluate the network structure quantitatively, we made Kratky plots in Figure 6.7, and carried out curve fitting analysis for middle and high-q region by using OZ function. The solid lines in Figure 6.7(a) and (b) are fitting results of OZ function. As seen in Figure 6.7, Kratky plots were well-represented by the fitted OZ function. By using these fitting parameters for Kratky plots, OZ functions were reconstructed in Figure 6.6 (solid lines). As shown in Figure 6.6, SANS functions were also well-represented by OZ function for middle and high-q region except for upturns in low-q region. This issue will be discussed in a later section.

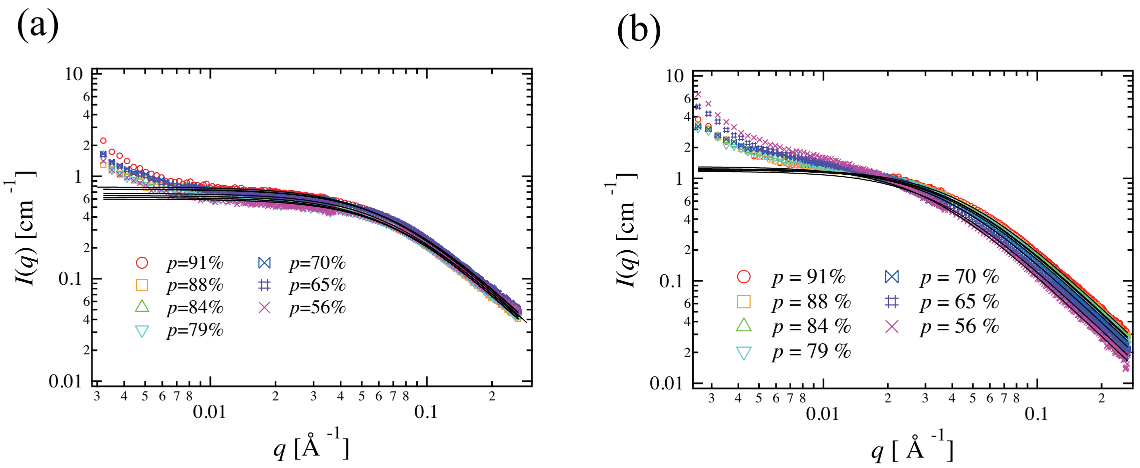

Figure 6.6: SANS intensity functions of the p-tuned Tetra-PEG gels for (a) as-prepared gels and (b) the corresponding swollen gels. The solid lines are fitting results of Orstein-Zernike function evaluated from Kratly plots in Figure 6.7

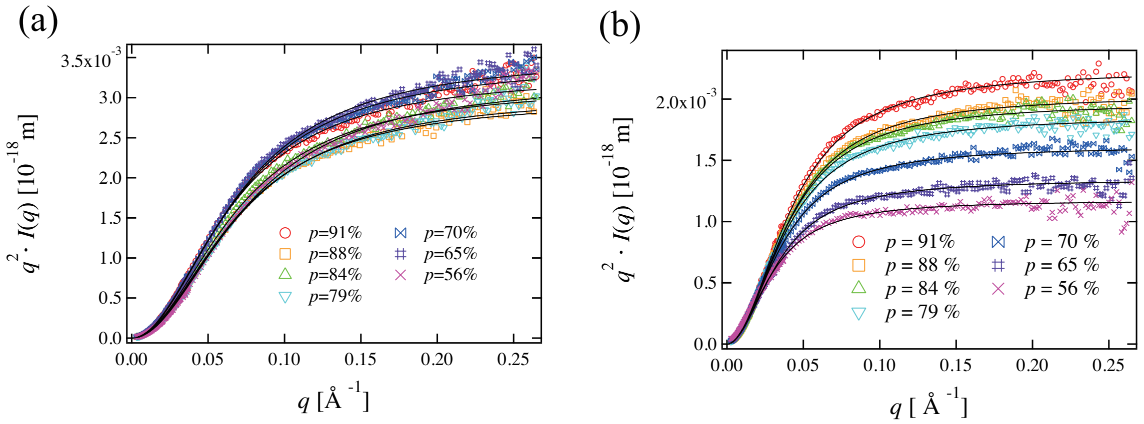

Figure 6.7: Kratky polts of the p-tuned Tetra-PEG gels for (a) as-prepared gels and (b) the corresponding swollen gels. The solid lines are fitting results of Orstein-Zernike function.

The fitting parameters of OZ function are shown in Figure 6.8. As shown in Figure 6.8(a), I_0 at as-prepared state and swollen state are constant. In Figure 6.8(b), ξ at as-prepared state is constant irrespective of p, while that at swollen state increases with decreasing p. By considering the experimental results shown in Figure 6.8, we propose a schematic picture of the network structure with respect to p, which is shown in Figure 6.9. As discussed in the previous section, the scattering function does not change though the reaction probability decreases and the voids in infinite clusters increase. The reason is that the voids of an infinite cluster are filled with sol component and the concentration fluctuations of polymers are suppressed. (See Figure 6.9(a) and (b).) As for I_0 at swollen state, the variation of I_0 is relatively small. This is because in view of $I_0 \sim \phi^2\xi^3$,[31–33] ϕ decreases and ξ increases as decreasing p and increasing swelling ratio, leading to compensation of the two opposite tendency. On the other hand, after the sol component was subtracted from gels by equilibrium swelling, ξ increases with the decrease in p because finite clusters resident in voids in an infinite cluster are removed and the voids are expanded (See Figure 6.9(c) and (d)).

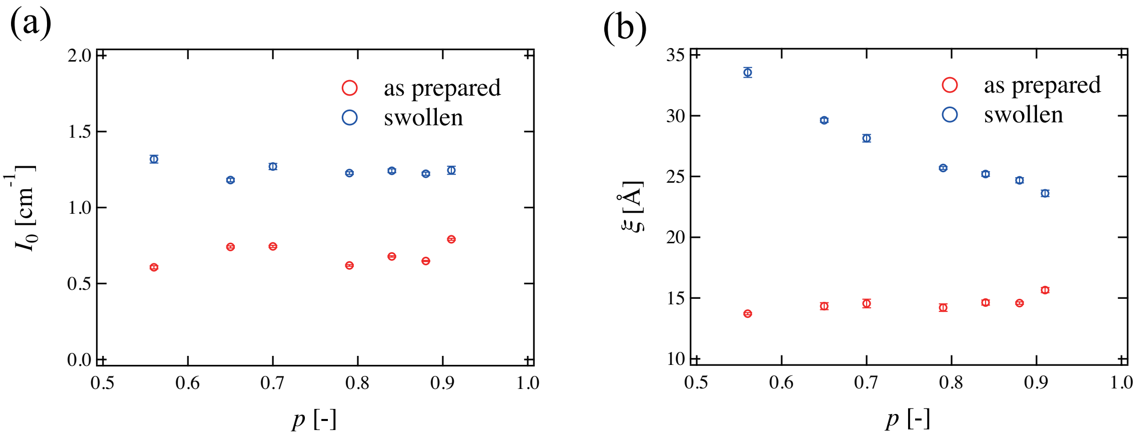

Figure 6.8: Variation of (a) I_0 and (b) ξ as a function of p for as-prepared (red circles) and swollen gels (blue circles).

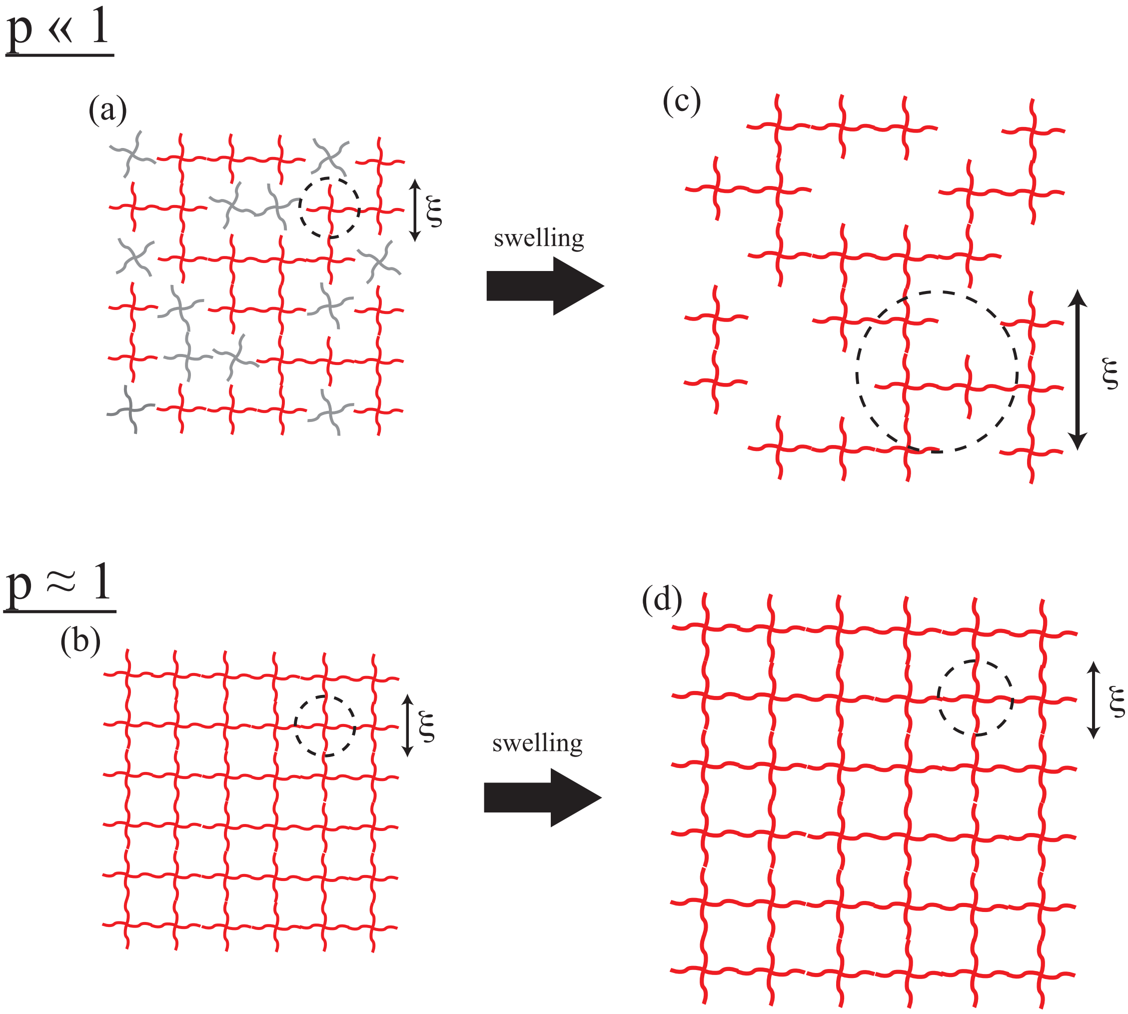

Figure 6.9: Schematical picture of the structure of the p-tuned Tetra-PEG gels for (a) $p \ll 1$ and (b) $p \simeq 1$ in as-prepared state. By swelling, these networks are expanded inomogeneously (c; for $p \ll 1$) and uniformly (d; for $p \simeq 1$)

When we return to Figure 6.6(a) and (b), the upturns of the scattering intensity at low-q region can be observed. It can be deduced that the origin of the upturns is ascribed to the inhomogeneities of the network. In order to evaluate the intensity increase, the sum of OZ function, $I_{\mathrm{OZ}}(q)$ and the excess scattering, $I_{\mathrm{ex}}(q)$ is frequently used.[6,7,32,34,35]

$$I\,(q) = I_{\mathrm{OZ}}(q) + I_{\mathrm{ex}}(q) \quad , \tag{6.2}$$

Several functional forms of $I_{\mathrm{ex}}(q)$ have been proposed phenomenologically. For example,

$$I_{\mathrm{ex}}(q) = \frac{I_{\mathrm{ex}}(0)}{(1+\Xi^2 q^2)^2} \quad , \tag{6.3}$$

$$I_{\mathrm{ex}}(q) = I_{\mathrm{ex}}(0)\exp[-(q\Xi)^x] \quad , \tag{6.4}$$

where, Ξ is the characteristic length of inhomogeneity and x is an exponent in the range of 0.7 - 2.[38] Eqs (6.3) and (6.4) is the so-called Debye-Bueche function[38,39] and the extended Guinier equation,[32,40–45] respectively. However, because upturns in low-q region are weak in Figure 6.6, the fitting analysis is unreliable. Thus, we calculate the invariant of excess scattering, Q_{ex}, as follows.

$$Q_{\mathrm{ex}} = \int \left(I_{\mathrm{obs}}(q) - I_{\mathrm{OZ}}(q)\right) q^2 dq \quad . \tag{6.5}$$

Here, $I_{\mathrm{obs}}(q)$ and $I_{\mathrm{OZ}}(q)$ are experimental value of scattering intensity and the fitting results of OZ function shown in Figure 6.6, respectively. Figure 6.10 shows the p dependence of Q_{ex}. At as-prepared state, Q_{ex} is small and constant, and concentration fluctuations from inhomogeneity are suppressed. On the other hand, as p decreases, Q_{ex} increases at swollen state. In order to explain this tendency, we show the schematic picture based on "blob percolation model" proposed by Bastide and Leibler[?] in Figure 6.11. When the network is randomly cross-linked, large-scale cross-linking density fluctuations much larger than the correlation length ξ exists in the network. When this network is swollen, we have a subtle interspersion of two media: the frozen blob cluster with “high” cross-linking densities and the “interstitial” medium with low cross-linking densities. When p is high, because connectivity-defects are few and fluctuations of cross-linking density are small, one scarcely observes above interspersion at swollen state. On the other hand, when p is low, fluctuations of cross-linking density are large. Thus, the inhomogeneity is enhanced at swollen state. For this reason, the invariant of the inhomogeneity increases with decreasing p when the gel is swollen.

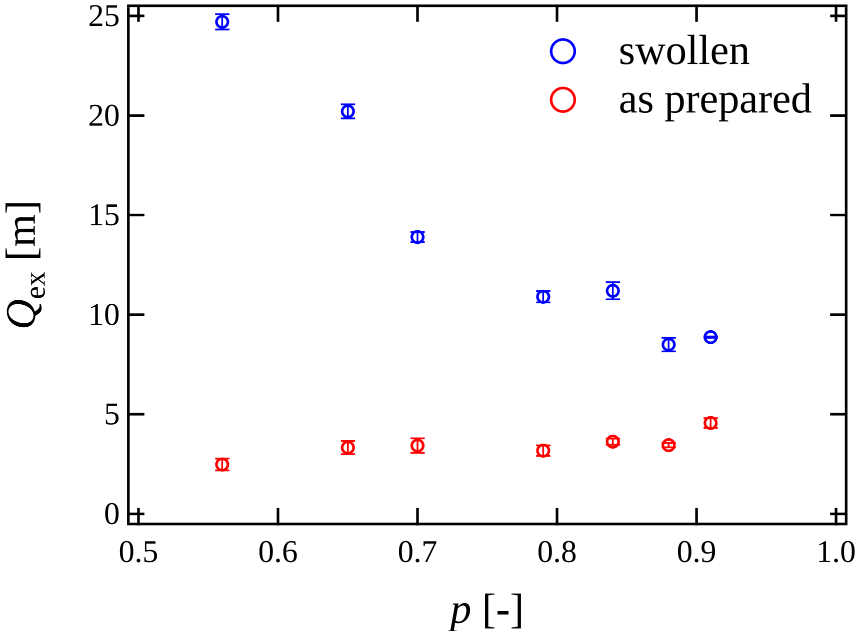

Figure 6.10: Invariants of excess scattering of the p-tuned Tetra-PEG gels for as-prepared gels (red circles) and the corresponding swollen gels (blue circles)

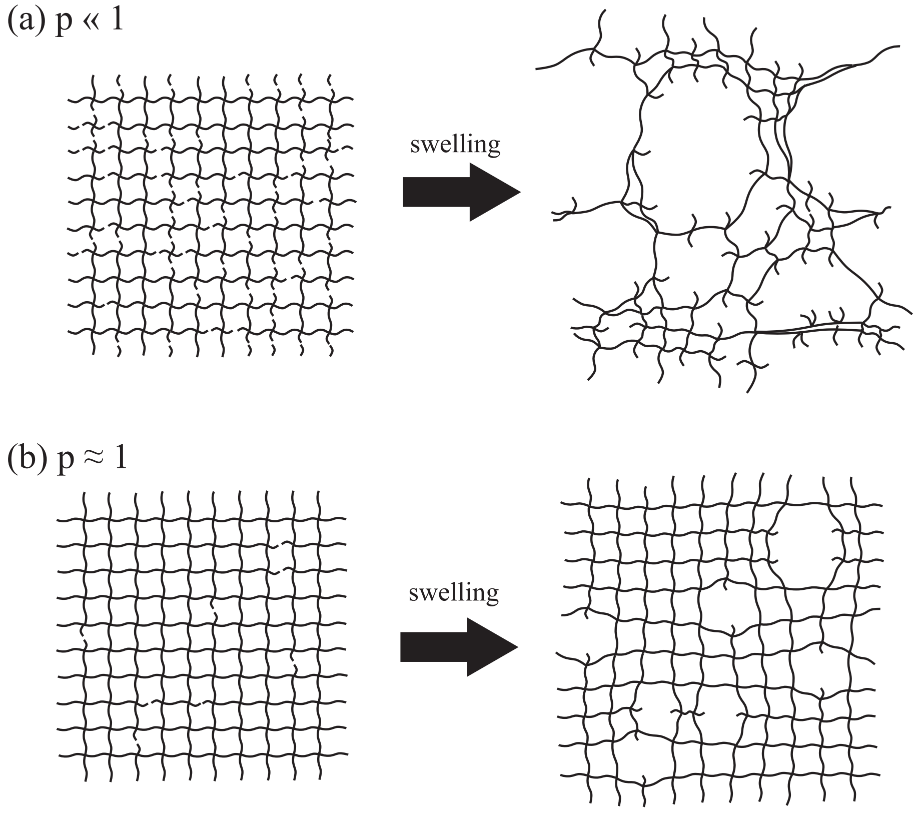

Figure 6.11: Schematic representations of the network structures of the p-tuned gel for (a) $p \ll 1$ and (b) $p \simeq 1$. Large scale inhomogeneities are more pronounced in swollen gels as decreasing p.

6.4 Conclusion

We conducted two series of SANS experiment on the Tetra-PEG gel. First, we conducted time-resolved SANS on the gelation process in $\phi < \phi^*$ region and observed the increase of the correlation length and the scattering intensity. This indicates that, because primary polymers do not overlap in $\phi < \phi^*$ region, a sparse network are formed as primary polymers aggregate during the gelation process.

Secondly, we prepared p-tuned Tetra-PEG gels and soaked them in water to expose the inhomogeneieties. From the SANS measurement, scattering profiles do not vary for as-prepared state though the reaction probability varies. On the other hand, in the swollen state, a systematical increase in the correlation length was observed with decreasing p. The reason is that the voids in an infinite cluster are filled with sol component and the concentration fluctuations of polymers are suppressed at as-prepared state, while in the swollen state sol components are removed and the voids are expanded. Furthermore, an upturn in the scattering intensity in low-q region was also observed with decreasing p. This tendency is ascribed to a fluctuation of the cross-linking density, which is much larger than the correlation length ξ.

References

[1] Stein, R. S., *J. Polym. Sci.*, **1969**, B7, 657-660.

[2] Pines, E.; Prins, W., *J. Polym. Sci., Polym. Phys. Ed.*, **1972**, B10, 719-724.

[3] Candau, S.; Bastide, J.; Delsanti, M., *Adv. Polym. Sci.*, **1982**, 44, 27.

[4] Panyukov, S.; Rabin, Y., *Macromolecules*, **1996**, 29, 7960-7975.

[5] Bastide, J.; Candau, S. J., Structure of Gels as Investigated by Means of Static Scattering Techniques. In The Physical Properties of Polymer Gels, Cohen Addad, J. P., Ed. John Wiley: NY, **1996**; Vol. Chapt. 9, p 143.

[6] Shibayama, M., *Macromol. Chem. Phys.*, **1998**, 199, 1-30.

[7] Shibayama, M.; Norisuye, *T. Bull. Chem. Soc. Jpn.*, **2002**, 75, 641-659.

[8] Mark, J. E.; Sullivan, J. L., *J. Chem. Phys.*, **1977**, 66, 1006-1011.

[9] Jong, L.; Stein, R. S., *Macromolecules*, **1991**, 24, (9), 2323-2329.

[10] Sullivan, J. L.; Mark, J. E.; Hampton, P. G.; Cohen, R. E., *J. Chem. Phys.*, **1978**, 68, 2010-2012.

[11] Mark, J. E.; Rahalkar, R. R.; Sullivan, J. L., *J. Chem. Phys.*, **1979**, 70, 1794-1797.

[12] Llorente, M. A.; Mark, J. E., *J. Chem. Phys.*, **1979**, 71, 682-689.

[13] Mendes, E.; Girard, B.; Picot, C.; Buzier, M.; Boue, F.; Bastide, J., *Macromolecules*, **1993**, 26, 6873-6877.

[14] Takahashi, H.; Shibayama, M.; Fujisawa, H.; Nomura, S., *Macromolecules*, **1995**, 28, 8824-8828.

[15] Takahashi, H.; Shibayama, M.; Hashimoto, M.; Nomura, S., *Macromolecules*, **1995**, 28, 5547-5553.

[16] Shibayama, M.; Takahashi, H.; Nomura, S.; Imai, M., *Polymer*, **1998**, 39, 3759.

[17] Shibayama, M.; H., T.; Yamaguchi, H.; Sakurai, S.; Nomura, S., *Polymer*, **1994**, 35, 2944-2951.

[18] Sakai, T.; Matsunaga, T.; Yamamoto, Y.; Ito, C.; Yoshida, R.; Suzuki, S.; Sasaki, N.; Shibayama, M.; Chung, U. I., *Macromolecules*, **2008**, 41, (14), 5379-5384.

[19] Matsunaga, T.; Sakai, T.; Akagi, Y.; Chung, U.; Shibayama, M., *Macromolecules*, **2009**, 42, (4), 1344-1351.

[20] Matsunaga, T.; Sakai, T.; Akagi, Y.; Chung, U. I.; Shibayama, M., *Macromolecules*, **2009**, 42, (16), 6245-6252.

[21] Matsunaga, T.; Asai, H.; Akagi, Y.; Sakai, T.; Chung, U.; Shibayama, M., *Macromolecules*, **2011**, 44, 1203-1210.

[22] Asai, H.; Fujii, K.; Ueki, T.; Sakai, T.; Chung, U.; Watanabe, M.; Han, Y. S.; Kim, T. H.; Shibayama, M., *Macromolecules*, **2012**, 45, 3902-3909.

[23] Nishi, K.; Chijiishi, M.; Katsumoto, Y.; Nakao, T.; Fujii, K.; Chung, U.; Noguchi, H.; Sakai, T.; Shibayama, M., *J. Chem. Phys.*, **2012**, 137, 224903.

[24] Kurakazu, M.; Katashima, T.; Chijiishi, M.; Nishi, N.; Akagi, Y.; Matsunaga, T.; Shibayama, M.; Chung, U.; Sakai, T., *Macromolecules*, **2010**, 43, 3935-3940.

[25] Nishi, K.; Fujii, K.; Chijiishi, M.; Katsumoto, Y.; Chung, U.; Sakai, T.; Shibayama, M., *Macromolecules*, **2012**, 45 (2), 1031-1036.

[26] Miron, T.; Wikchek, M., *Anal. Biochem.*, **1982**, 126, 433-435.

[27] Ornstein, L. S.; Zernike, F., *Proc. Acad. Sci.*, Amsterdam **1914**, 17, 793.

[28] Okabe, S.; Karino, T.; Nagao, M.; Watanabe, S.; Shibayama, M., *SANS-U. Nuclear Inst. and Methods in Physics Research, A*, **2007**, 572, 853-858.

[29] Akagi, Y.; Gong, J. P.; Chung, U. I.; Sakai, T., *Macromolecules*, **2013**, 46 (3), 1035-1040.

[30] Martin, J. E.; Wilcoxon, J.; Odinek, J., *Phys. Rev. A* , **1991**, 43, 858-871.

[31] Asai, H.; Fujii, K.; Ueki, T.; Sakai, T.; Chung, U.; Watanabe, M.; Han, Y. S.; Kim, T. H.; Shibayama, M. Macromolecules 2012, 45, 3902-3909.

[32] Mallam, S.; Horkay, F.; Hecht, A. M.; Rennie, A. R.; Geissler, E. Macromolecules 1991, 24, 543.

[33] Mendes, E. J.; Lindner, P.; Buzier, M.; Boue, F.; Bastide, J. Phys. Rev. Lett. 1991, 66, 1595.

[34] Horkay, F.; Hecht, A. M.; Geissler, E. Macromolecules 1994, 27, 1795.

[35] Horkay, F.; McKenna, G. B.; Deschamps, P.; Geissler, E. Macromolecules 2000, 33, 5215-5220.

[36] Shibayama, M., Multiphases in Polymeric Gels. In Structure and Properties of Multi-Phase Polymeric Materials, Araki, T.; Tran-Cong, Q.; Shibayama, M., Eds. Marcel Dekker: New York, 1998; Vol. Chapt. 6, pp 195-231.

[37] Shibayama, M.; Ikkai, F.; Shiwa, Y.; Rabin, Y. J. Chem. Phys. 1997, 107, 5227-5235.

[38] Wu, W.; Shibayama, M.; Roy, S.; Kurokawa, H.; Coyen, L. D.; Nomura, S.; Stein, R. S. Macromolecules 1990, 23, 2245-2251.

[39] Debye, P.; Bueche, A. M. J. Appl. Phys. 1949, 20, (20), 518-525.

[40] Hecht, A. M.; Duplessix, R.; Geissler, E. Macromolecules 1985, 18, 2167.

[41] Mallam, S.; Hecht, A. M.; Geissler, E. J. Chem. Phys 1989, 91, 6447.

[42] Mallam, S.; Horkay, F.; Hecht, A. M.; Geissler, E. Macromolecules 1989, 22, 3356.

[43] Horkay, F.; Hecht, A. M.; Mallam, S.; Geissler, E.; Rennie, A. R. Macromolecules 1991, 24, 2896.

[44] Cohen, Y.; Ramon, O.; Kopelman, I. J.; Mizrahi, S. J. Polym. Sci., Polym. Phys. Ed. 1992, 30, 1055-1067.

[45] Shibayama, M.; Tanaka, T.; Han, C. C. J. Chem. Phys. 1992, 97, 6829-6841.

[46] Bastide, J.; Leibler, L., *Macromolecules*, **1988**, 21, 2647.

Chapter 7

Summary

Gelation process of model network was investigated from the view point of gelation kinetics (Chapter 2 and 3), elasticity (Chapter 4 and 5), and network structure (Chapter 6). Through these investigation, we clearly elucidate (i) gelation mechanism, (ii) calculation procedure for elastic modulus, and (iii) formation process of inhomogeneighties. These data are important for practical use of Tetra-PEG gel. In addition, I want to emphasize that these results on model network are common feature of gel system. The details of the respective chapters are summarized below.

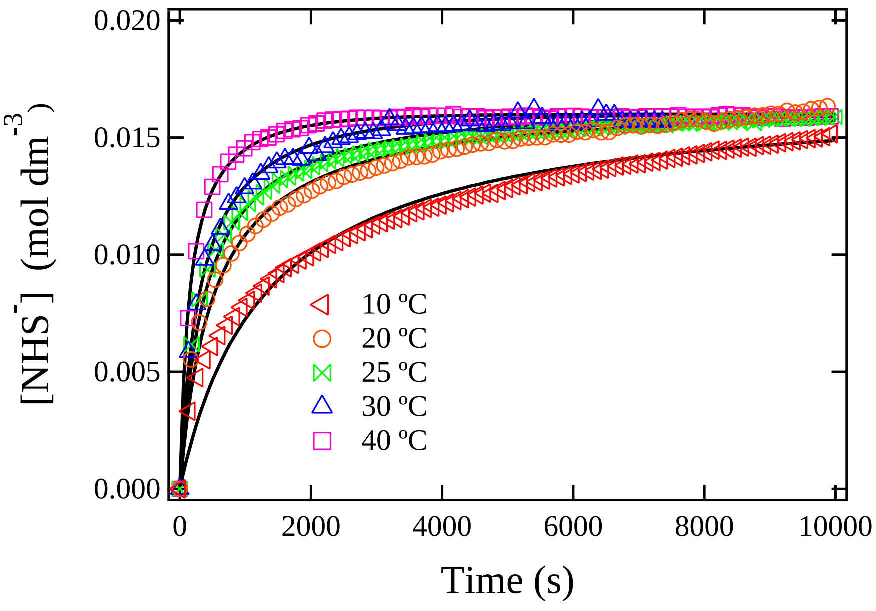

Figure 7.1: Kinetic trace obtained for dissociated NHS as a function of time. Solid lines represents the fitting results with second-order kinetics.

In Chapter 2, the reaction rate for the polycondensation in the Tetra-PEG gel system has been studied by ATR-IR spectroscopy. It was found that (1) the polycondensation kinetics of Tetra-PEG gel can be simply treated as a chemical reaction between mutually reactive end-groups in solution, (2) the reaction undergoes as a simple second-order reaction from beginning to end regardless of gelation threshold, and (3) the gelation mechanism was predicted from the thermodynamic enthalpy and entropy at the transition state estimated by temperature dependence of rate constants. The reason of smooth second-order kinetics is suspected to be that the reactivity of terminal groups on Tetra-PEGs is not affected by the steric hindrance, substitution effect, and gelation threshold.

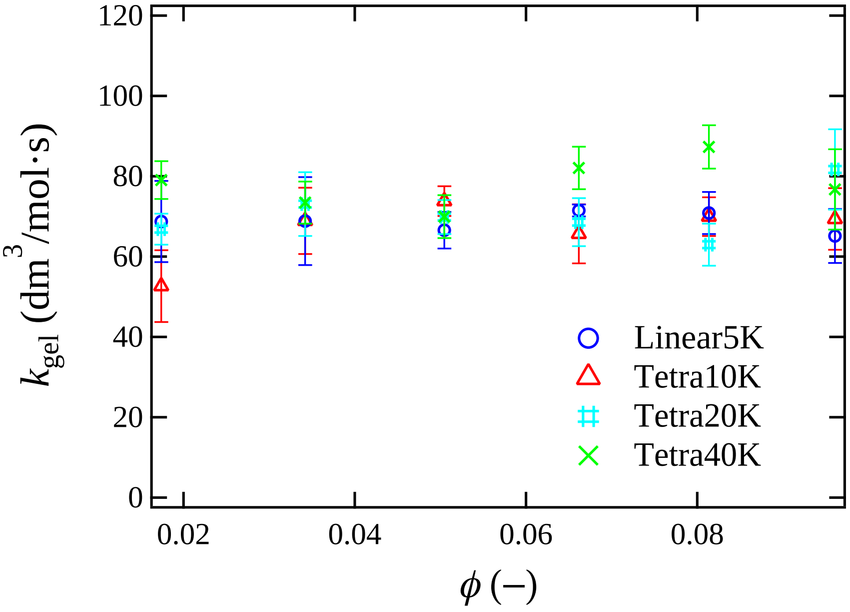

Figure 7.2: The gelation rate constant plotted against polymer concentration ϕ for Linear5K, Tetra10K, Tetra20K, and Tetra40K.The TetraPEG gels formed from primary molecule with $M_w = 10$, 20, and 40 kg/mol are named Tetra10K, Tetra20K, and Tetra40K, respectively.In addition, a mixed solution of LinearPEG-NH$_2$ and Linear-PEG-NHS is named Linear5K.

In Chapter 3, we report the kinetic study on the gelation reaction of Tetra-PEG gel system studied by ATR-IR and spectrophotometry. The reaction rate constant for the gelation of Tetra-PEG was determined in the aqueous solutions with varying both polymer concentration and primary molecular weight. It was clearly found that the no dependence of both factors is observed in the estimated rate constants in the

Tetra-PEG system, which is applied to analogous linear-PEG system with AB-type coupling of two linear PEG functionalized with amine and activated ester. From these results, we concluded that the gelation reaction of Tetra-PEG gel is not a diffusion-limited but a reaction-limited, i.e., reactive groups encounter and/or separate each other frequently, while the reaction rate of the amide-bond formation is low. It is thus expected that polymers can diffuse and are homogeneously mixed in the solution during the gelation process to lead to the homogeneity and high-strength of Tetra-PEG gel.

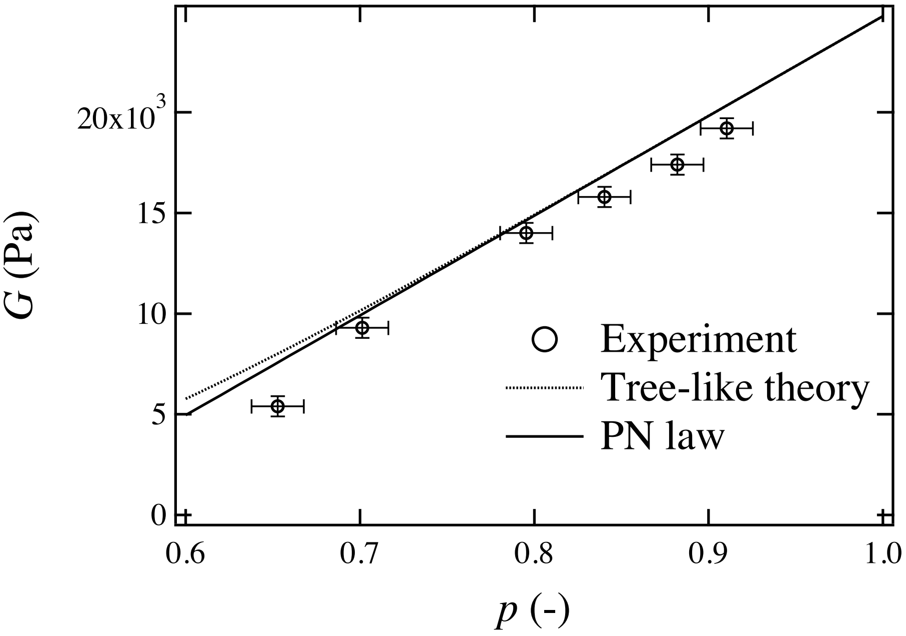

Figure 7.3: The elastic constant G as a function of p. Circles and line are the experimental data and the results of the PN law, respectively.

In Chapter 4, we investigated the relationship between the elastic modulus, G and the reaction probability, p for polymer networks. First, we pointed out that the elastic modulus is expressed by $G = [(fp/2 - 1) + O((p-1)^2)]\, Nk_{\mathrm{B}}T/V$ (Percolated Network law ; PN law), which does not depend on the local topology of the network structure or the existence of the loops. Here, N is the number of lattice point, V is the system volume, f is the functionality of the cross-link, k_{B} is the Boltzmann constant, and T is the absolute temperature. We also conducted simulations for polymer networks with triangular and diamond lattices, and mechanical testing experiments on Tetra-PEG gel with systematically tuning the reaction probability. Here, the Tetra-PEG gel was confirmed to be a potential candidate for ideal polymer networks consisting of unimodal strands free from defects and entanglements. From the results of simulations and experiments, it was revealed, for the first time, that the elastic modulus obeys this law in the wide range of p ($p_c \gg p \geq 1$), where p_c is the reaction probability at gelation threshold.

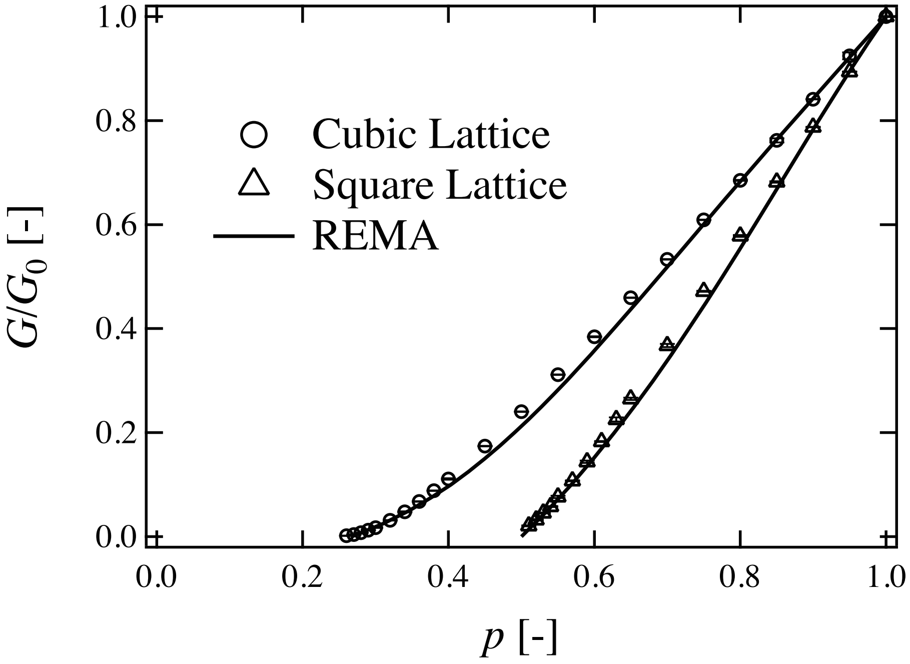

Figure 7.4: Elastic modulus of a square and a cubic lattices of random polymer network.

In Chapter 5, we propose a theory that approximately determines the elastic modulus of bond-disordered polymer networks over the entire range of bond probability p. This theory overcomes unsolved problems of (i) the assumption of no-loop formation in tree-like theory and (ii) incapability of determination of the absolute value of elastic modulus in percolation/scaling theories. The predicted elastic modulus of the theory is in excellent agreement with the results of simulations not only in the scaling exponents of the critical behavior but also in the absolute values for $p \geq p_c$, where p_c is p at the gelation threshold. We also conducted mechanical testing experiments on Tetra-poly(ethylene glycol) (PEG) gel with systematically tuning p. Here, the Tetra-PEG gel is considered to have an ideal diamond lattices and consists of unimodal strands free from defects and entanglements. We find, for the first time, that this theory provides good agreement with the experimental data.

Gelation process

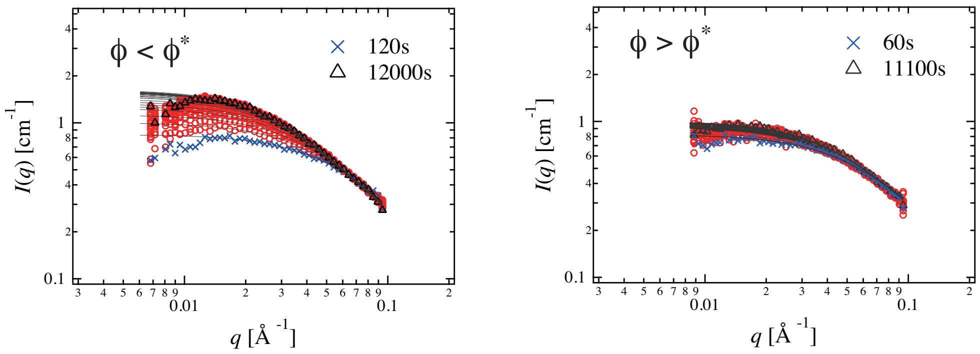

p-tuned gel

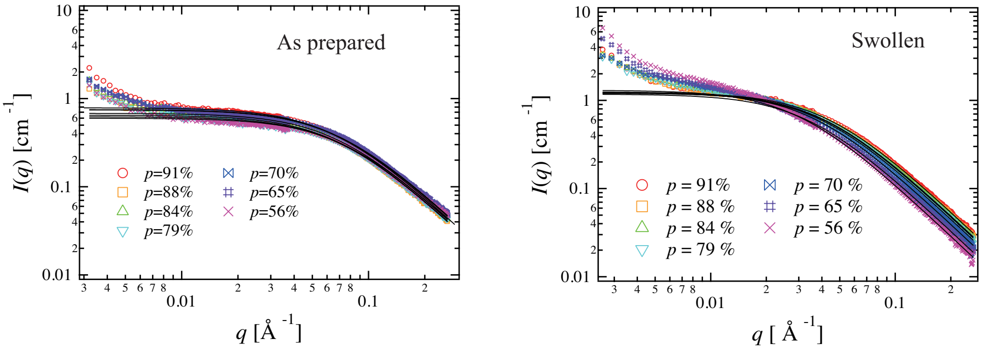

Figure 7.5: SANS curves for gelation process and p-tuned gels.

In Chapter 6, we systematically introduced two types of defects into Tetra-PEG gels and investigated effects of defects on inhomogeneities. Firstly, we prepared defect-rich networks by simply reducing primary polymer concentration, and observed the evolution of network structure by time-resolved SANS during gelation process. In this case, both the scattering intensity and the correlation length increased with reaction time in the $\phi < \phi^*$ region , while they scarcely changed in the $\phi > \phi^*$ region. Here, ϕ and ϕ^* is the polymer volume fraction and that at chain-overlap concentration. Secondly, we prepared Tetra-PEG gels by tuning the reaction probability, p, and soaked the p-tuned gels in water to expose the inhomogeneieties. It was revealed that SANS profiles of as-prepared gels did not change noticeably, while those of swollen gels systematically increased with decreasing p. On the basis of these results, we discuss the relationship between the defects of polymer network and inhomogeneities by using simple schematic pictures of polymer network.

Appendix

A.1 SANS and DLS Study of Tacticity Effects on Hydrophobicity and Phase Separation of Poly(*N*-isopropylacrylamide).

A.1.1 Summary

The tacticity effect on phase separation process of poly (*N*-isopropylacrylamide) (PNiPAM) aqueous solutions was investigated by dynamic light scattering (DLS) and small angle neutron scattering (SANS) measurements. SANS measurement revealed that hydrophobicity of PNiPAM consisting of meso- and racemo-isomers increased with increasing the meso-content. This result is in accordance with the result of the previous experimental and simulation study on NiPAM dimers (DNiPAM) and trimers (TNiPAM) [Katsumoto, Y. et al., *J. Phys. Chem. B* **2010**, 114, 13312-13318, and Autieri, E. et al., *J. Phys. Chem. B*, **2011**, 115, 5827-5839.], i.e. meso-diad is more hydrophobic than racemo-diad. In addition, a series of scattering experiments revealed that the ratio of meso-diad does not affect the static structure or the shrinking behavior of a single chain, but strongly affects the aggregation behavior. The PNiPAM with low meso-content suddenly associate around the phase separation temperature, while that of the high meso-content gradually aggregate with increasing temperature. We propose that phase transition behavior of PNiPAM aqueous solutions can be controlled by changing the stereoregularity of the polymer chain.

A.1.2 Introduction

Stimuli-responsive polymers have been attracted keen interests due to their industrial, medical and scientific interests.[1,2] Because stimuli-responsiveness is a common feature for biopolymers in living organisms, synthetic stimuli-responsive polymers have been explored to understand the unique properties of biopolymers. One of the most efficient designs for stimuli-responsive polymers is to utilize lower critical solution temperature (LCST)-type phase behavior of polymer solutions. Below the cloud point temperature (T_c), LCST-type thermo-responsive polymer chains and solvent molecules are well-interacted in one phase by hydrophobic solvation, i.e., hydrogen-bonding between water and polymer chains. Above T_c, on the other hand, the interaction energy among the polymer chains overcomes the hydration energy of the polymer chains. These stimuli-responsive polymers have potential to be used as an intelligent material especially in the biomedical field.[2,3]

For the molecular design of LCST-type thermo-responsive polymers, we have to consider at least two aspects: (i) the interaction between water and polymer chain and (ii) that among polymer chains. The former must be focused on at the first step of the design, and many chemical structures of side chains, which have a desirable hydrophobic and hydrophilic balance, are proposed such as amide groups,[1] ether groups,[4] and ester groups.5 Although the former plays a major role on the solubility, the latter, i.e., interactions among polymer chains, is also very important to tune the properties of the materials. Some of LCST-type thermo-responsive polymers undergo a coil-to-globule transition of single chains in the vicinity of T_c,[6] while there are also several polymers that only aggregation occurs at T_c without changing the radius of gyration of a single coil.[7] Thus, it is crucial for molecular design of stimuli-responsive polymers to reveal how the primary structure of the polymers affects hydration and aggregation behavior of the system.

One of typical systems is an aqueous solution of poly(N-isopropylacrylamide) (PNiPAM), which undergoes an LCST type phase separation.[1,2,8–10] Due to its sharp and reversible transition behavior at 32 - 34 °C, this phenomenon has attracted much attention of scientists and engineers. On the basis of experimental evidence obtained by calorimetry,[1,8,11–16] infrared spectroscopy,[17–19] dielectric relaxation,[20] and fluorescence studies,[21–23] it is believed that macroscopic LCST phase separation of PNiPAM solution is ascribed to disruption of the structured water molecules around the hydrophobic iso-propyl group at T_c to give a large freedom of motion (entropy), which is a driving force for phase separation. Light scattering experiments on PNiPAM dilute solutions revealed that single chain exhibits a coil-to-globule transition[9,24] and neutron scattering on semi-dilute solutions showed divergence of the correlation length by approaching T_c[25,26]

Recently, it has been revealed that the phase separation behavior strongly depends on the tacticity of PNiPAM.[27–30] Here, we focus on two types of the tacticity, i.e., meso-diad (m) and racemo-diad (r), which are shown in Figure A.1. From transmittance measurements, it was revealed that the cloud-point temperature tends to decrease, while the steepness of the transmittance curve is decreased with increasing meso-diad content of PNiPAM.[29] We have pointed out from the water/chloroform distribution coefficient of NIPAM-dimer (DNiPAM) that DNiPAM with r configuration (r-DNiPAM) is more soluble to water than that with m (m-DNiPAM).[30] The molecular mechanics (MM) calculations revealed that r-DNiPAM in water is more stable than m-DNiPAM because r-DNiPAM is advantageous in terms of the hydration free energy and conformational entropy.[30] This result indicates that the stereosequence of polymer chain plays an important role on the physical properties of polymer-aqueous systems. There is also a report for investigating the conformation of PNiPAm trimers in water, indicating that the stability of the syndiotactic configuration arises from the conformational entropy.[31] Although these previous papers clarify the hydrophobic character of short origomers, the tacticity dependence of the transmittance curve has not been clearly understood at the molecular level, which is related to aggregation behavior for the PNiPAM with varying the m/r ratio. In order to elucidating it, we conducted dynamic light scattering (DLS) and small-angle neutron scattering (SANS) experiments on PNiPAM solutions having different meso-contents. We discuss the tacticity effect on collapsing behavior of single polymer chain by DLS measurement for dilute solutions and on aggregation process of polymer chains based on SANS results.

A.1.3 Experimental Section

Materials

PNiPAM with various meso-diad ratios ranged from 46 to 58 % were synthesized by using established techniques. PNiPAM samples were prepared by stereospecific living radical polymerization using a reversible addition-fragmentation chain transfer (RAFT) agent and a Lewis acid catalyst.[27] 1-Phenylethyl phenyldithioacetate (PEPD) was used as the RAFT agent, which was synthesized according to the liter-

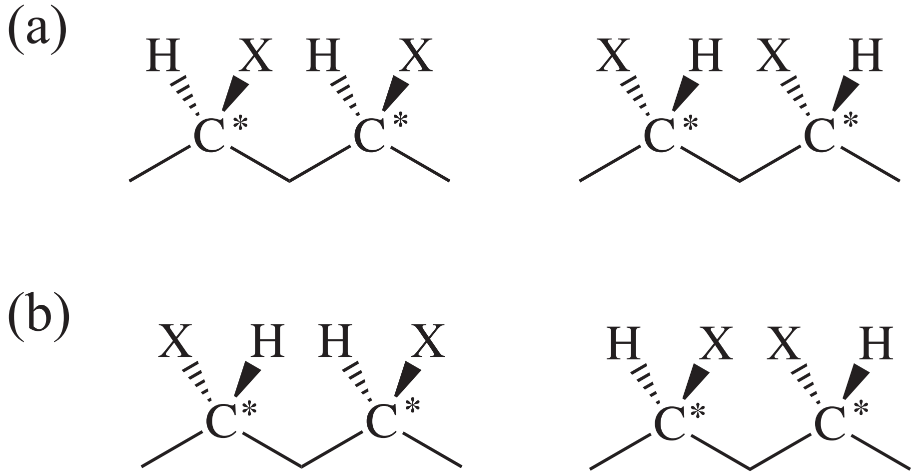

Figure A.1: Two types of diads for vinyl polymers ($-\mathrm{CH_2}-\mathrm{CHX}-$): (a)meso diad; (b) racemo diad.

ature.[32] NiPAM and α,α-azobisisobutyronitrile (AIBN), the monomer and initiator, were recrystallized from a benzene/hexane solution. The impurities were removed from the polymer solution through dialysis to yield the final product obtained as a fluffy white solid by freeze-drying. The number-averaged molecular weight (M_n) and polydispersity (M_w/M_n) of the prepared samples were determined by size exclusion chromatography (SEC; Intelligent HPLC system) made by Jasco (Tokyo, Japan) equipped with a Shodex (Tokyo, Japan) SB-807 HQ guard column, two linear poly(hydroxy methacrylate) beads columns (Shodex SB-802.5 HQ and SB-806M), and a Jasco RI-2031 differential refractive-index detector. The eluent was *N,N*-dimethylformamide (LiBr 10 mM) at 60 °C with a flow rate of 0.35 mL/min. SEC chromatogram was calibrated by using the standard polystyrene samples. ^{1}H NMR spectra were recorded on a JEOL (Tokyo, Japan) JNM-LAMBDA spectrometer (500 MHz). The tacticity of the samples was represented by the diad ratio (m:r), which was determined from the methylene proton peaks of the polymer measured in DMSO-d6 at 145 °C.[27] SEC data are shown in Figure A.2 and the recipe of the sample preparation and characterization results with a sample ID are compiled in Table A.1.

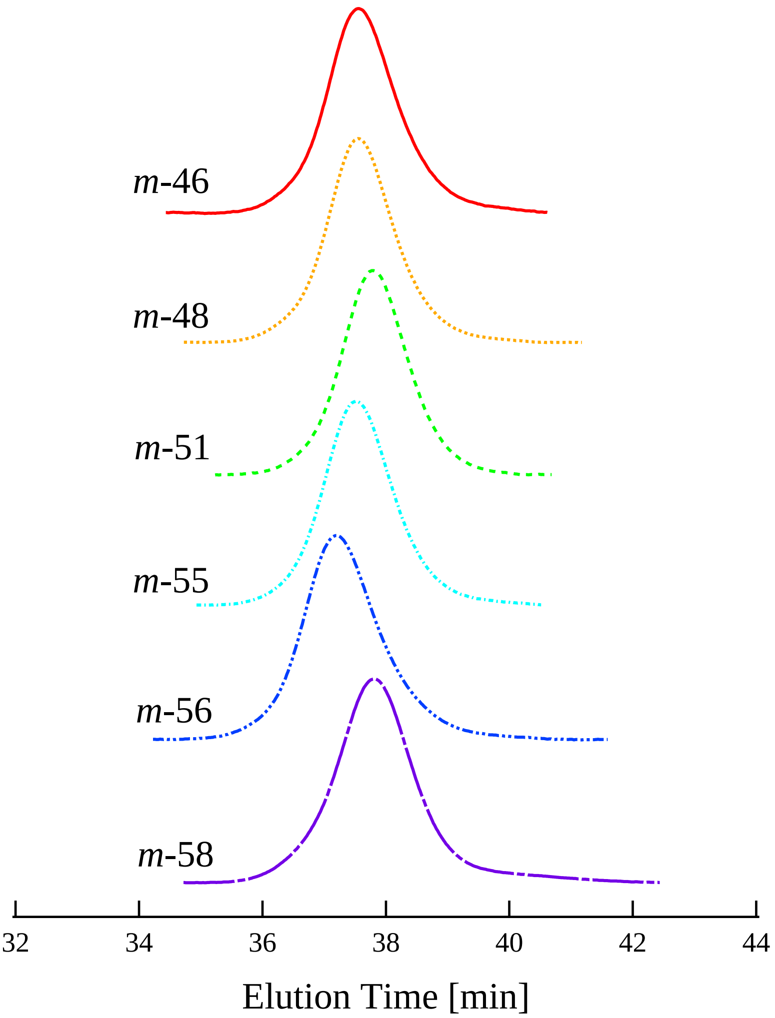

Figure A.2: SEC charts of PNiPAM samples with m-46, m-48, m-51, m-55, m-56, and m-58.

sampleID	m	M_n/ g mol^{-1} M_w/M_n	metal(OTf)$_3$/M	M	
m-46	46	3.6×10^4	1.20	-	
m-48	48	3.7×10^4	1.20	0.016	Sc
m-51	51	3.3×10^4	1.17	0.035	Sc
m-55	55	3.8×10^4	1.20	0.057	Sc
m-56	56	4.3×10^4	1.25	0.007	Y
m-58	58	2.9×10^4	1.37	0.10	Sc

Table A.1: Characterization of Stereocontrolled PNiPAMs. [NiPA] = 2.23 M, [AIBN] = 0.8 mM, and [PEPD] = 8.94 mM in methanol/toluene(1/1, v/v) mixture. Polymerization at 60 °C. Metal (OTf)$_3$: Metal trifluoromethanesulfonate. Sc and Y are scandium and yttrium, respectively.

Dynamic Light Scattering (DLS)

DLS measurements were carried out by using DLS/SLS-5000 compact goniometer (ALV, Langen) coupled with an ALV photon correlator. A 22mW helium-neon laser (wavelength, $\lambda = 632.8$ nm) was used as incident beam, and the scattering angle θ was 90°. Each measurement time was 30 s. The measurement temperature was monitored at sample position by a thermocouple. We conducted two series of experiments; (1) concentration and (2) temperature dependence of R_h for dilute solutions. In the former, we prepared polymer solutions with concentrations from 0.1 to 6 wt%, and DLS measurements were performed at 10 °C. In the latter, on the other hand, DLS measurements were performed on the 0.2 wt% solution with increasing temperature from 10 °C to 35 °C at a rate of 0.1 °C/min. The interval of successive measurements was 30 s.

Small-Angle Neutron Scattering (SANS)

SANS experiments were carried out on High-flux Advanced Neutron Application Reactor (HANARO) located at Korea Atomic Energy Research Institute (KAERI), Korea. A monochromated cold neutron beam with an average neutron wavelength 6.00 Å was irradiated to the samples. The scattered neutrons were counted with a 2D detector. The sample-to-detector distances were chosen to be 9.5 m. The polymer concentration of PNiPAM solution was set to 2 wt%. Each sample was equilibrated at 15 °C and then heated stepwise to 19 °C, 23 °C, 25 °C, 27 °C, 29 °C 31 °C, 33 °C, and 35 °C. The samples were equilibrated for at least 15 min at each temperature before measurement. After necessary corrections for open beam scattering, transmission, and detector inhomogeneities, corrected scattering intensity functions were normalized to the absolute intensity scale.

A.1.4 Results and Discussion

Observation of phase separation process

Figure A.3 shows the temperature dependence of time-averaged intensities, $\langle I \rangle_T$, at the scattering angle of 90° for the PNiPAM solutions with various diad ratios to clarify the macroscopic character, i.e., turbidity, for each sample. It was found that the intensity drastically increases at the cloud point (T_c), and the T_c decreases in a systematic way with increasing m. The result is in good accordance with the transmittance results reported elsewhere.[28,29] In addition, we found there is another systematic change in the steepness of intensity change with temperature. The m-46 sample shows steeper change of scattered intensity in comparison with those of higher m samples. To elucidate the reasons for this gradual intensity change, we thus extended our study to structural investigation at the microscopic level, as described below.

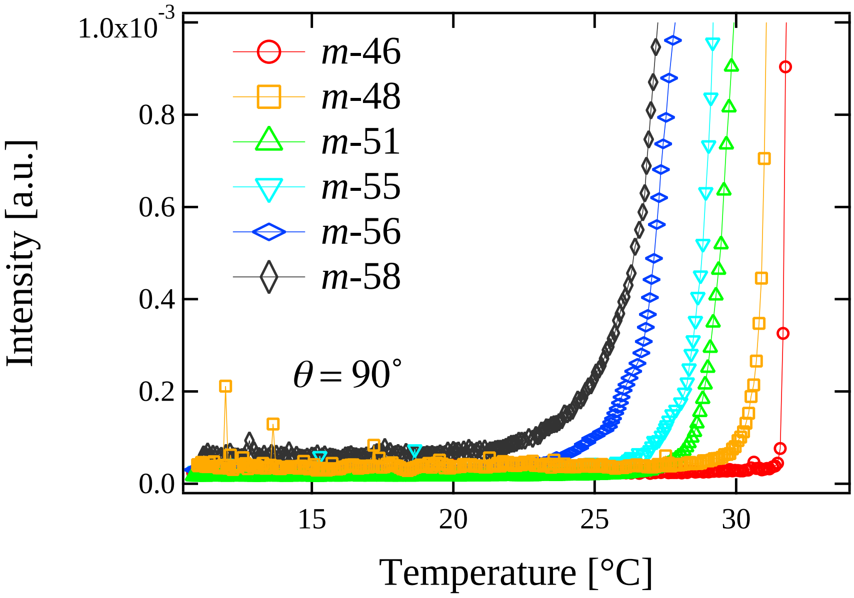

Figure A.3: Temperature dependence of scattering intensities of PNiPAM solutions with m-46, m-48, m-51, m-55, m-56, and m-58.

Shrinking Process of a single chain

DLS measurements were carried out for each sample at various concentrations to see the state of coils. Figure A.4(a) shows the concentration dependence of normalized auto correlation function for m-46 PNiPAM solutions at 10 °C. In the dilute region, a single relaxation mode ($\Gamma^{-1} \sim 0.1$ ms^{-1}) is observed, which is ascribed to Brownian motion of single coils. As the concentration increases, the slow mode (Γ^{-1}=1$\sim$ 10 ms^{-1}) appears. Similar phenomena were often observed in other works.[33,34] This mode is ascribed to the translational mode of polymer clusters as discussed in previous studies.[33,34] Figure A.4(b) and (c) show a typical result of ICFs and characteristic decay time distribution functions for aqueous PNiPAM solutions with various diad

(m/r) ratios. We calculated R_h from the fast relaxation mode of these data as shown below.

Figure A.5 shows the polymer concentration dependence on the single coil size, R_h calculated from the fast mode of CONTIN data for m-46 and m-56 as representative of various meso-content samples. It was found in both figures that there is a plateau region in R_h below 0.5 wt% and R_h decrease with polymer concentration above 1 wt%. This fact implies that the solution below 0.5 wt% is in dilute region ($< C^*$) and the solution over 1 wt% is in the transition region ($\approx C^*$) from dilute to semi-dilute solution, where C^* is the chain overlap concentration. By considering these results, we prepared 0.2 wt% solutions to observe the shrinking process of a single chain and 2 wt% ($\approx C^*$) solutions to observe clustering effects of polymers.

Figure A.6 shows R_h values with varying temperature for the PNiPAM solutions with m-46 $\sim$ m-58 at 0.2 wt% below T_c. It was found that the R_h value monotonically decreases for all the solutions, i.e., the coil shrinks in the size with increasing temperature independent of the diad ratio. This result indicates that the behavior of a single coil is little influenced by the m content at least in the temperature range before the sample solutions become opaque. On the other hand, the slow mode, which corresponds to the translational mode of polymer clusters, became faster with increasing temperature, and the decays of the fast and slow modes finaly merged into a single decay around T_c (data is not shown). Note that a similar behavior is observed for the other aqueous solutions of thermo-responsive polymers.[33] As a result, the single-coil size of PNiPAM is no longer characterized above the temperatures marked with the arrows in the figure A.6.

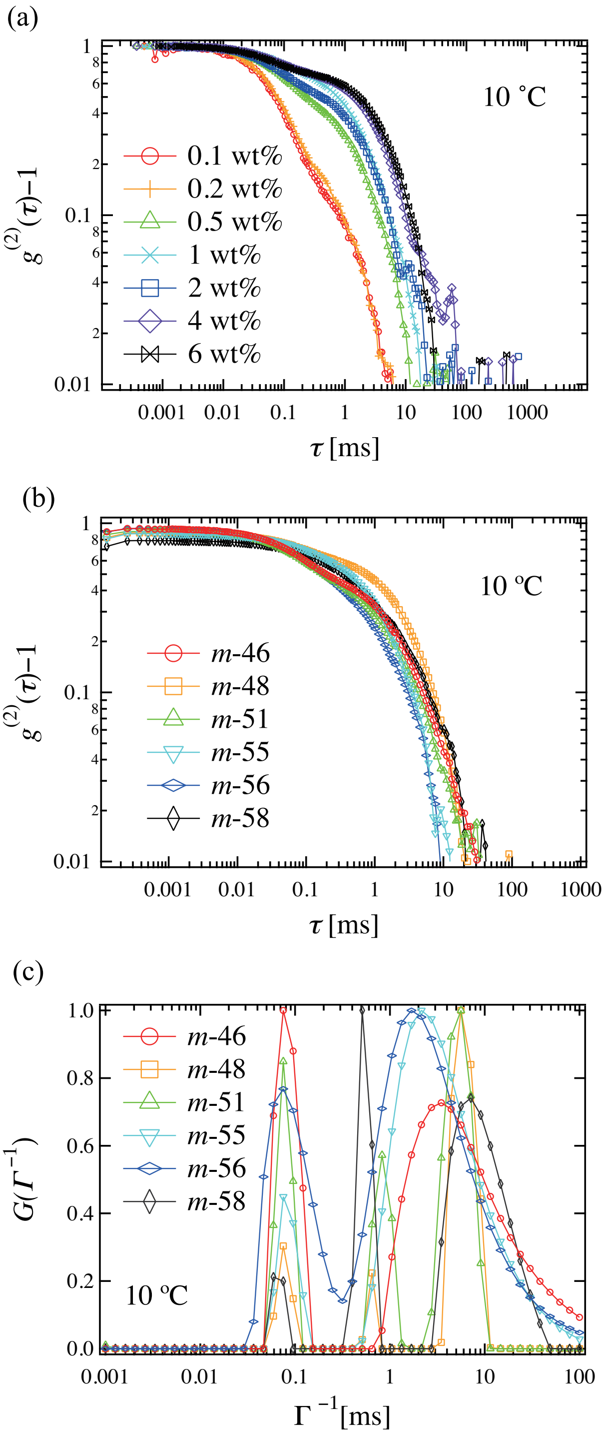

Figure A.4: (a) Normalized auto correlation functions for m-46 PNiPAM solutions with the various concentrations at 10 °C. Typical results of (b) ICFs and (c) characteristic decay time distribution functions, $G(\Gamma^{-1})$ of PNiPAM solutions with the various content of meso-diad at 2 wt%.

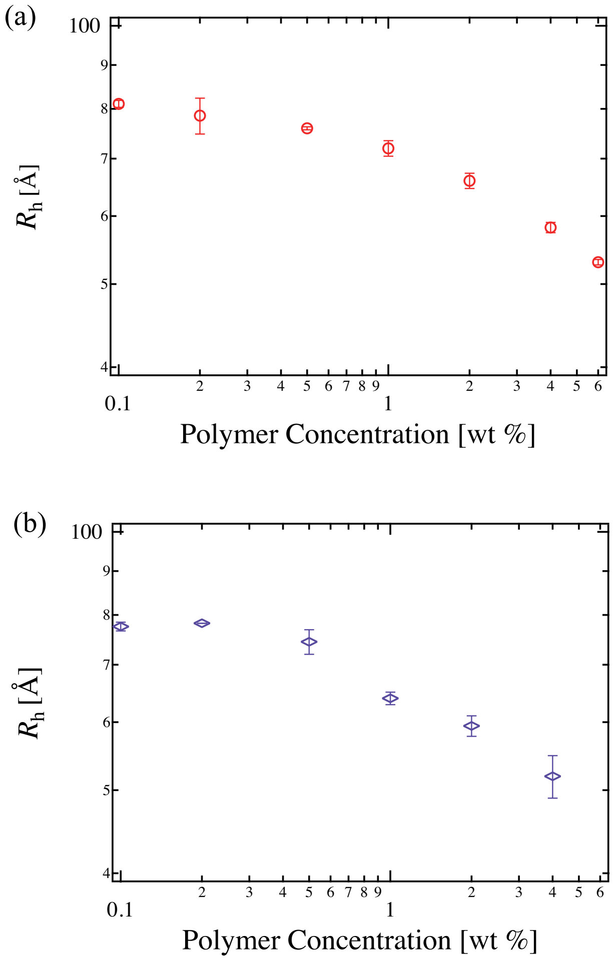

Figure A.5: Concentration dependence of R_h of PNiPAM solutions: (a) m-46; (b) m-56.

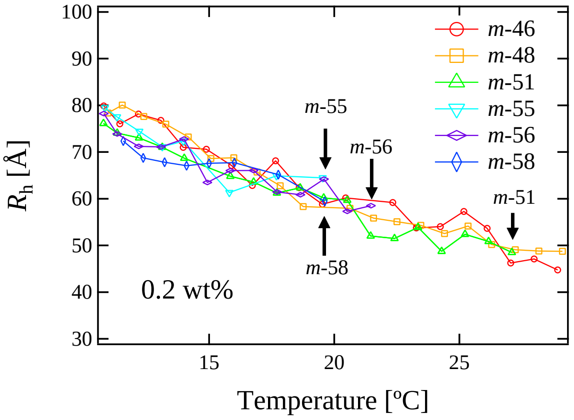

Figure A.6: Concentration dependence of R_h of PNiPAM solutions: (a) m-46; (b) m-56.

Aggregation Process

Temperature-resolved SANS measurements have been performed to investigate the tacticity effects on the phase separation with 2 wt% solution of stereo-controlled PNiPAMs. Figure A.7 (a)-(f) shows SANS curves observed for the PNiPAM solutions with m-46 $\sim$ m-58. In Figures A.7(a) and (b), at temperatures below T_c (15 - 29 °C), the scattering curves showed an intensity plateau (0.01-0.03 Å^{-1}) and the intensity decayed for $q > 0.03\text{Å}^{-1}$, which is a characteristic curve for polymer solutions. As temperature increased above 31 °C, the SANS curves changed dramatically with additional strong scattering for $q < 0.01\text{Å}^{-1}$, indicating phase separation. Figures (c) $\sim$ (f), on the other hand, the scattering intensity increased gradually, indicating a gradual domain formation. This tendency, i.e., a gradual transition, is more pronounced for the samples with larger m.

To quantitatively evaluate the size of domain (or aggregation) in the solutions, we carried out curve fitting analysis for the observed SANS functions. For high-q region, we used the following Debye function with a single contact theory (eq (A.1)) as fitting functions.[35]

$$I_1\left(q\right) = \frac{(\Delta\rho)^2}{N_A}\frac{V_2\phi P_D(q)}{1+(1-2\chi)\left(\dfrac{V_2}{V_1}\right)\phi P_D(q)} \tag{A.1}$$

$$P_D(q) = Z\frac{2}{u^2}\left(e^{-u}-1+u\right), \quad u = R_g^2 q^2 \tag{A.2}$$

Here, N_A is the Avogadro's number, χ is the Flory-Huggins's interaction parameter, ϕ is the polymer volume fraction, Z is the degree of polymerization, V_1 and V_2 is the molar volume of the water and PNiPAM, and $\Delta\rho$ is the difference of scattering length densities between the PNiPAM monomer and D_2O, 5.4×10^{10} cm^{-2}. Eq (A.1) is a well known scattering function to describe an interacting polymer chain in dilute solutions. For low-q region, we mainly used the following Debye-Bueche function to describe the formation of domains with interfaces between water-rich and PNiPAM-rich domain.[36]

$$I_2\left(q\right) = V\left\langle\rho^2\right\rangle\frac{8\pi l_p^3}{\left(1+l_p^2q^2\right)^2} \tag{A.3}$$

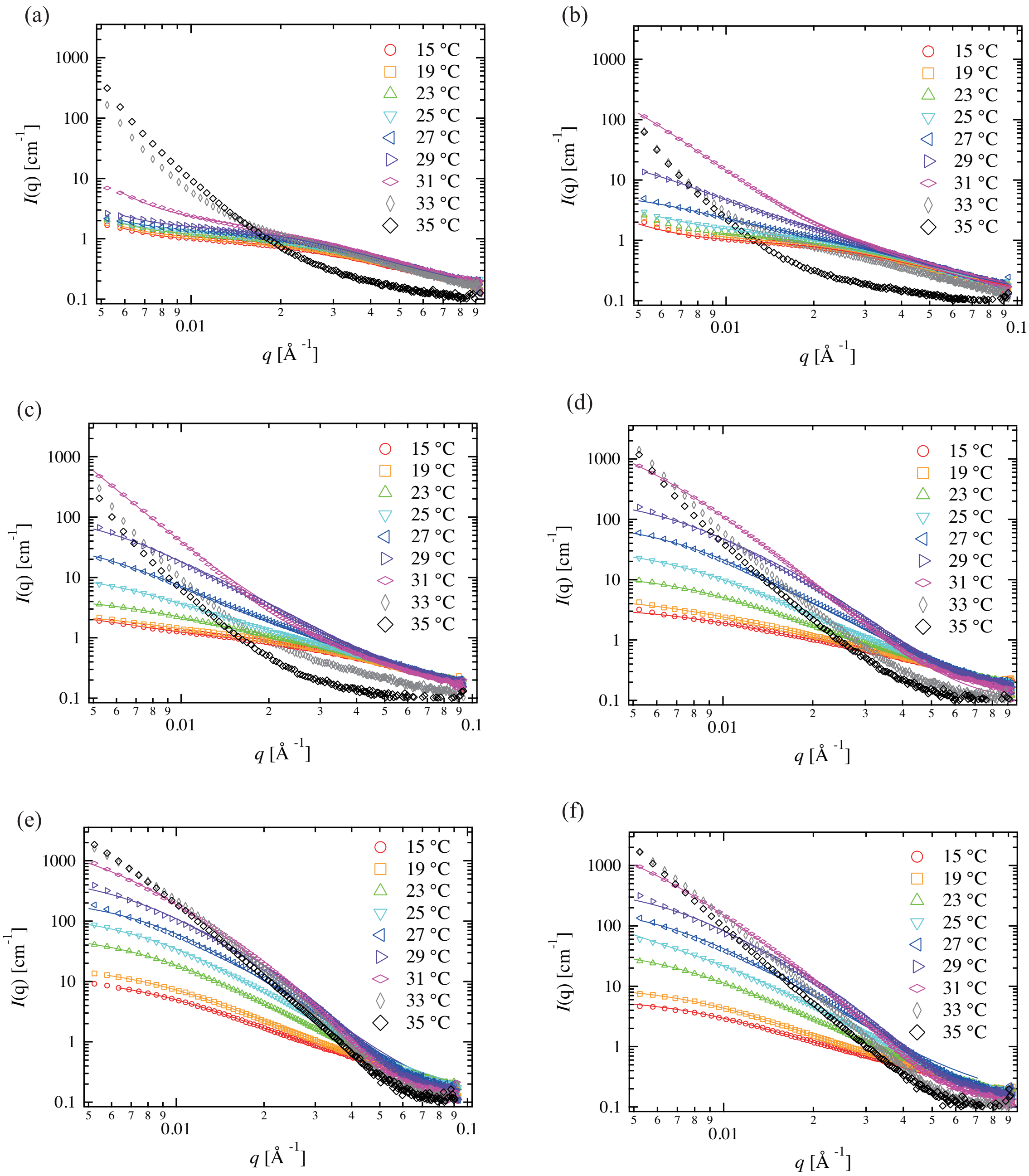

Figure A.7: Temperature dependence of SANS profiles for 2 wt% PNiPAM solutions, (a) m-46, (b) m-48, (c) m-51, (d) m-55, (e) m-56, and (f) m-58. The solid lines indicate the fitting results by eq (A.1) and eq (A.3) or eq (A.1) and eq (A.5).

Here, l_p is

$$l_p = 4\frac{V}{S}\frac{\langle\rho^2\rangle}{\langle\Delta\rho^2\rangle} \tag{A.4}$$

S/V is the interface area per volume, and $\langle\rho^2\rangle = \rho_A^2\phi_A + \rho_B^2\phi_B$, where ρ_j and ϕ_j are the scattering length density and the volume fraction of the component j. However, an additional scattering is relatively weak for m-46 at 15~31 °C and m-48 at 15~23 °C, so the fitting results lack reliability. For these SANS curves, we used the Porod law, which is the $q \to \infty$ limit of the Debye-Bueche function.[36]

$$I_2(q) \to 2\pi\left\langle\rho^2\right\rangle\frac{S}{V}\frac{1}{q^4} \tag{A.5}$$

Hence, we use a model

$$I(q) = I_1(q) + I_2(q) + I_{\mathrm{inc}} \tag{A.6}$$

Here, I_{inc} is the incoherent scattering intensity. The observed $I(q)$s are well reproduced by both eq (A.6), as shown with solid lines in Figure A.7.

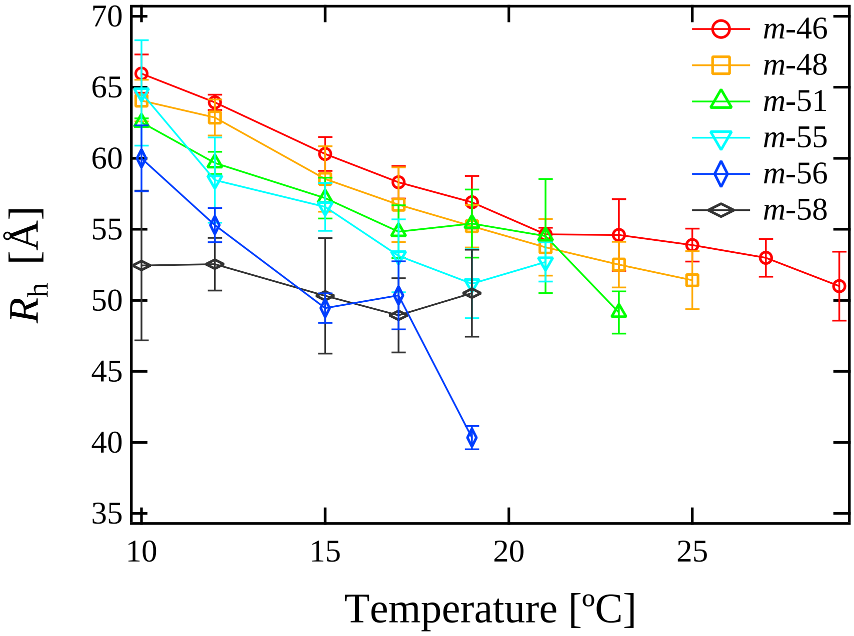

Figure A.8: Temperature dependence of the R_h of PNiPAM solutions with the various content of meso diad at 2 wt%.

DLS measurements were conducted on the 2 wt% PNiPAM solutions with various meso content in order to calculate R_g/R_h ratio. Each samples were equilibrated at

10 °C and changed to 12 °C, 15 °C, 17 °C, 19 °C, 21 °C, 23 °C, 25 °C, 27 °C, 29 °C in a stepwise. The samples were equilibrated for at least 30 min at each temperature before measurement. Figure A.8 shows temperature dependence of the R_h of PNiPAM solutions with the various content of meso diad at 2 wt%. As depicted in figure A.8, R_hs are monotonically decreased with increasing temperature. As well as in figure A.6, a clear difference between the different ratio of meso-diad cannot be observed in figure A.8.

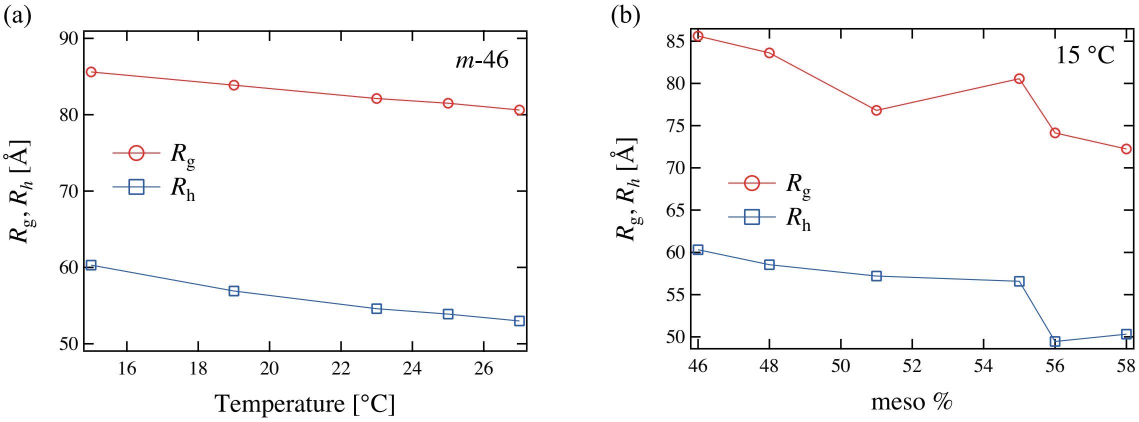

Figure A.9: (a) Variation of R_g and R_h of m-46 against temperature. (b) Variation of R_g and R_h against the ratio of meso-diad at 15 °C.

Figure A.9 (a) shows temperature dependence of the R_h and R_g of PNiPAM solutions with the various content of meso-diad at 2 wt%. As depicted in figure A.9 (a), R_hs and R_gs are monotonically decreased with increasing temperature. Figure A.9 (b) shows a meso-diad content dependence of the R_h and R_g. R_hs and R_gs are not monotonically decreased with increasing the meso content because of a difference of polymerization degrees among samples.

We calculated R_g/R_h ratio from the respective values estimated by SANS and DLS measurements, respectively. Figure A.10 (a) and (b) show temperature and meso-diad content dependences, respectively, of the R_g/R_h ratio for m-46 system. As shown in Figure A.10 (a), the R_g/R_h ratio of m-46 is approximately 1.5 in the T range of 15 - 29 °C which is below enough the T_c ($= 32 \sim 34$ °C). It is well known that this ratio corresponds to a Gaussian coil conformation of polymer in solution.[37] This result is consistent with the works of Kubota et al.[38] and Wu et al.[24] and confirms the validity of fitting analysis by Debye function with a single contact theory in the

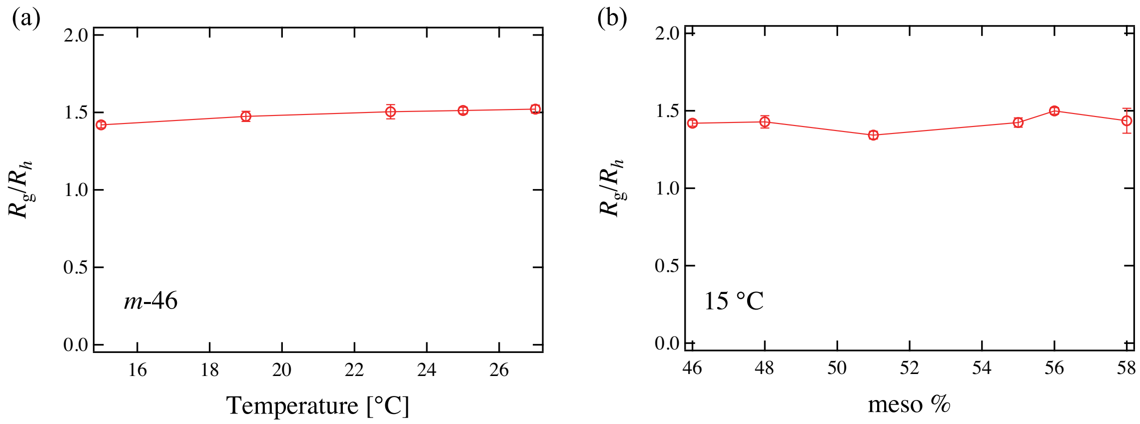

Figure A.10: (a) Variation of the ratio R_g/R_h of m-46 against temperature. (b) Variation of the ratio R_g/R_h against the ratio of meso-diad at 15 °C.

temperature range examined here. As for Figure A.10 (b), the R_g/R_h ratio is also approximately 1.5 at any meso-diad content, which indicates PNiPAM chains behave as Gaussian coils. Combined with the discussion in the previous section, we concluded that the difference in tacticity of PNiPAM does not affect the conformation nor the shrinking behavior of a single chain.

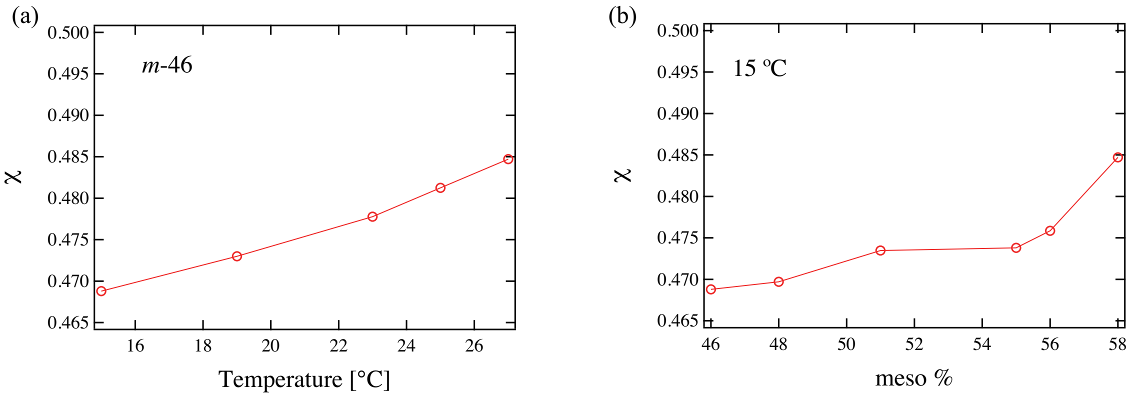

Figure A.11: (a) Temperature dependence of χ for m-46 system and (b) the meso content dependence of χ at 15 °C.

Figure A.11 shows χ values obtained from the fitting analysis of SANS experiments, where χ is the polymer-solvent interaction parameter. It was clearly seen in Figure A.11(a) that there is appreciable temperature dependence of χ for m-46 system, and the χ value increases and approaches 0.5 with increasing temperature. This indicates that the interaction between water and polymer becomes weaker and a polymer becomes hydrophobic. Figure A.11(b) shows the meso-diad content dependence of χ for 15 °C. The χ value also increased with increasing m ratio (in Figure A.11(b)), indicating that hydrophobicity of PNiPAM depends on the m ratio. Katsumoto et al.[30] concluded from the water/chloroform distribution coefficient of DNiPAMs that the hydrophobicity is higher for m-DNiPAM than for r-DNiPAM because r-DNiPAM is advantageous in terms of the hydration free energy and conformational entropy as revealed by the MM simulation. In addtion, Autieri et al.[31] concluded from the simulation that a lower hydrophilicity of isotactic trimer, in comparison with the syndiotactic one, is related to a lower conformational entropy. The result obtained by SANS is in good agreement with these experimental and simulation results for short oligomers.

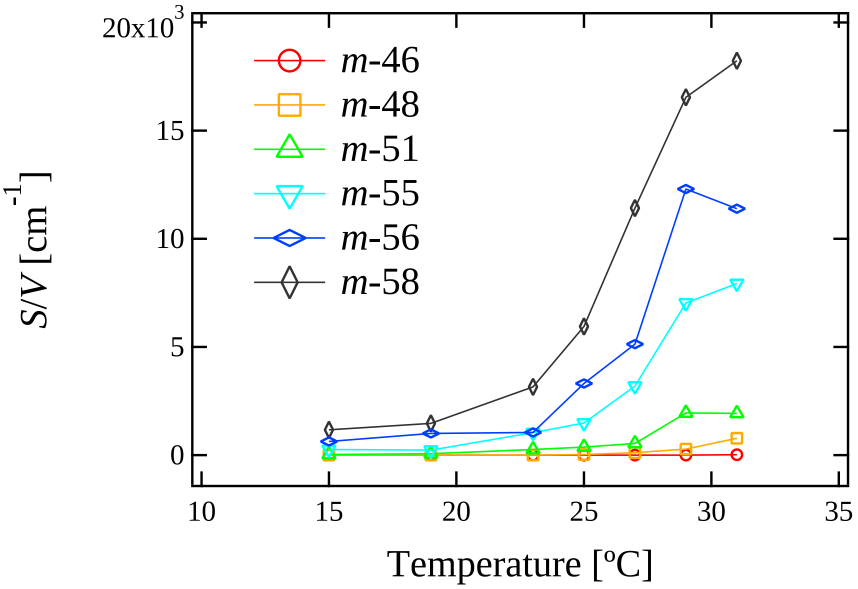

Figure A.12: Specific surface S/V for PNiPAM solutions with various meso content below T_c.

Figure A.12 shows temperature dependence of the specific surface, i.e., the interface area divided by the volume of the domains S/V estimated from the fitting results of Debye-Bueche function or Porod law. For m-46 and $m-48$, no enhancement in the S/V was observed even at any temperatures below T_c, followed by a sudden domain formation at around T_c. On the other hand, for m-51, m-55, m-56, and m-58, the domains gradually grow with increasing temperature, and the extent in the increase is significant for higher meso-content system. It is worth emphasizing that the temperature dependence of S/V for the polymer system is systematically changed by the m content, implying that the thermally-induced aggregation process can be precisely controlled by the stereoregularity of the PNiPAM chain. The results are consistent with those for the transmittance and scattering intensity of DLS as discussed in Figure A.3 and the work by Katsumoto et al.[29] The difference in tacticity does not affect the shrinking behavior of a single chain, but strongly affects the intermolecular interaction.

Structural aspects of phase separation

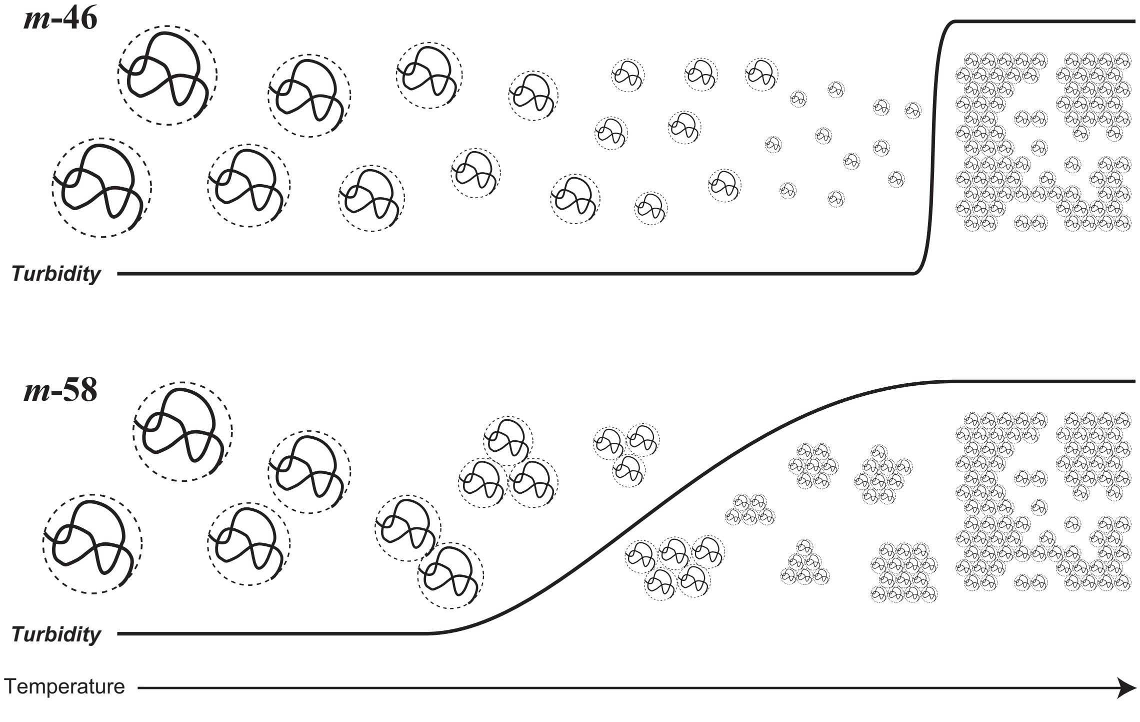

Figure A.13: Schematic illustration for phase separation process with the various meso content.

On the basis of the above-mentioned results, we propose a mechanism for the phase separation process of PNiPAM aqueous solutions and their tacticity dependence, which is illustrated in Figure A.13. As seen in the results of DLS measurement, the single-coil of PNiPAM shrinks at a constant rate by increasing temperature irrespective of their m-content. On the other hand, as SANS measurements revealed, the difference in tacticity strongly affects the intermolecular interaction. In the case of low m-content system, as increasing temperature, the PNiPAM chains shrink but do not aggregate with each other. Around the phase separation temperature, the shrunken PNiPAM chains suddenly associate and then the phase separation process completes. In the case of high m-content system, the PNiPAM chains gradually aggregate to form clusters with increasing temperature, and the phase separation gradually proceeds.

The results obtained here suggest that there be at least two features in the phase separation behavior in response to the variation of the stereosequence: the changes in the T_c and the steepness of thermo-responsiveness. The shift in T_c may simply arise from the change in the population of m-content in the polymer chain. This phenomenon is similar to the situation when hydrophilic or hydrophobic comonomers are incorporated in PNiPAM chains by copolymerization. According to the simulation results of short oligomers by Katsumoto et al.[30] and Autieri et al.[31] a meso-diad is more hydrophobic than a racemo-diad. Therefore, an increase in the m-content leads to an increase in the hydrophobicity of PNiPAM through the changes in the hydrogen bonding among side chains. On the other hand, an increment of hydrophobicity of the polymer chain does not seem to be a sufficient condition for explaining the steepness of the thermo-responsiveness. It has been pointed out that the sharpness of the phase transition of an atactic PNiPAM (m-46) in water is ascribed to the cooperative hydration of the polymer.[39,40] According to Okada and Tanaka, hydration of the polymer chain is characterized by the degree of the cooperativity. That is, the all-or-none phase separation behavior of PNiPAM aqueous system irrespective of polymer concentration is related to a high cooperativity of hydration. In this model, if water molecules stabilizing polymer chains are cooperatively removed by thermal energy, the phase separation occurs steeply at a certain temperature. Thus, we infer that the existence of m sequence in a PNIPAM chain interferes the cooperative hydration of the polymer, causing a gradual responsiveness of the polymer to the temperature.

We finally note that LCST phase separation in aqueous PNiPAM solution is often interpreted from the viewpoints of hydrophobic hydration around bulky iso-propyl group. It is easily expected that the hydrophobic hydration structure depends on the ratio of m- and r-conformers within PNiPAM, i.e., the extent of hydrogen bonding network around iso-propyl group is different between m- and r-conformers. To clarify this at the molecular level, applications of spectroscopy and X-ray/neutron scattering at high-q range to this system are needed, and we are now going on.

A.1.5 Conculusion

The tacticity effect on the phase separation process of PNiPAM aqueous solutions was investigated by dynamic light scattering (DLS) and small angle neutron scattering (SANS) measurements. From the SANS measurement, it was revealed that χ increases and a polymer also becomes hydrophobic with increasing m. This result coincides with the previous results of computational simulation, i.e. racemo-diad is more hydrophilic than meso-diad. In addition, a series of scattering experiments suggests that the ratio of meso-diad does not affect the static conformation or the shrinking behavior of a single chain, but strongly affects the aggregation behavior. The PNiPAM with low meso-contents suddenly associate around the phase separation temperature, while PNiPAM chains of the high meso-content gradually aggregate with increasing temperature. It is demonstrated that the sharpness of the phase separation with respect to temperature can be varied by tuning the microstructure of PNiPAM, i.e., the meso/racemo content.

References

[1] Schild, H. G., *Prog. Polym. Sci.*, **1992**, 17, 163-249.

[2] Gil, E. S.; Hudson, S. M., *Prog. Polym. Wci.* **2004**, 29, 1173-1222.

[3] Alarcon, C. H.; Pennadam, S.; Alexander, C., *Chem. Soc. Rev.*, **2005**, 34, 276-285.

[4] Aoshima, S.; Kanaoka, S., *Adv. Poly. Sci.*, **2008**, 210, 169-208.

[5] Lutz, J.-F.; Akdemir, O.; Hoth, A., *J. Am. Chem. Soc.*, **2006**, 128, (40), 13046-13047.

[6] Wang, X.; Qiu, X.; Wu, C., *Macromolecules*, **1998**, 31, (9), 2972-2976.

[7] Itakura, M.; Inomata, K.; Nose, T., *Polymer*, **2000**, 41, (24), 8681-8687.

[8] Heskins, M.; Guillet, J. E., *J. Macromol. Sci. Chem.*, **1969**, 2, 1441-1455.

[9] Fujishige, S.; Kubota, K.; Ando, I., *J. Phys. Chem.*, **1989**, 93, 3311-3313.

[10] Tong, Z.; Zeng, F.; Zheng, X.; Sato, T., *Macromolecules*, **1999**, 32, 4488-4490.

[11] Otake, K.; Inomata, H.; Konno, M.; Saito, S., *Macromolecules*, **1990**, 23, 283.

[12] Feil, H.; Bae, Y. H.; Feijin, J.; Kim, S. W., *Macromolecules*, **1993**, 26, 2496-2500.

[13] Tiktopulo, E. I.; Bychkova, V. E.; Ricka, J.; Ptitsyn, O. B., *Macromolecules*, **1994**, 27, 2879-2882.

[14] Kujawa, P.; Winnik, F. M., *Macromolecules*, **2001**, 34, (12), 4130-4135.

[15] Shibayama, M.; Morimoto, M.; Nomura, S., *Macromolecules*, **1994**, 27, 5060-5066.

[16] Shibayama, M.; Mizutani, S.; Nomura, S., *Macromolecules*, **1996**, 29, 2019-2024.

[17] Maeda, H.; Higuchi, T.; Ikeda, I., *Langmuir*, **2000**, 16, 7503-7509.

[18] Katsumoto, Y.; Tanaka, T.; Sato, H.; Ozaki, Y., *J. Phys. Chem. A*, **2002**, 106, 3429-3435.

[19] Sun, B.; Lin, Y.; Wu, P.; Siesler, H. W., *Macromolecules*, **2008**, 41, 1512-1520.

[20] Ono, Y.; Shikata, T., *J. Am. Chem. Soc.*, **2006**, 128, 10030-10031.

[21] Winnik, F. M., *Macromolecules*, **1990**, 23, 233.

[22] Schild, H. G.; Muthukumar, M.; Tirrell, D. A., *Macromolecules*, **1991**, 24, 948.

[23] Ringsdorf, H.; Venzmer, J.; Winnik, F. M., *Macromolecules*, **1991**, 24, 1678-1686.

[24] Wu, C.; Zhou, S., *Macromolecules*, **1995**, 28, 8381.

[25] Shibayama, M.; Tanaka, T.; Han, C. C., *J. Chem. Phys.*, **1992**, 97, 6829-6841.

[26] Meier-Koll, A.; Pipich, V.; Busch, P.; Papadakis, C. M.; Muller-Buschbaum, P., *Langmuir*, **2012**, 28, 8791-8798.

[27] Ray, B.; Okamoto, Y.; Kamigaito, M.; Sawamoto, M.; Seno, K.; Kanaoka, S.; Aoshima, S., *Polym. J.*, *2005*, 37, 234-237.

[28] Hirano, T.; Okumura, Y.; Kitajima, H.; Seno, M.; Sato, T., *J. Polym. Sci. Part A: Polym. Chem.*, **2006**, 44, (15), 4450-4460.

[29] Katsumoto, Y.; Kubosaki, N., *Macromolecules*, **2008**, 41, 5955-5956.

[30] Katsumoto, Y.; Kubosaki, N.; Miyata, T., *J. Phys. Chem. B*, **2010**, 114, 13312-13318.

[31] Autieri, E.; Chiessi, E.; Lonardi, A.; Paradossi, G.; Sega, M., *J. Phys. Chem. B*, **2011**, 115, 5827-5839.

[32] Quinn, J. F.; Rizzardo, E.; Davis, T. P., *Chem. Com.*, **2001**, 0, (11), 1044-1045.

[33] Li, J.; Ngai, T.; Wu, C., *Polym. J.*, **2010**, 42, 609-625.

[34] Chen, H.; Ye, X.; Zhang, G.; Zhang, Q., *Polymer*, **2006**, 47, 8367-8373.

[35] Higgins, J. S.; Benoit, H. C., *Polymers and Neutron Scattering.*, Clarendon Press: Oxford, **1994**.

[36] Roe, R. J., *Methods of X-ray and Neutron scattering in polymer science.*, Oxford Universuty: New York, **2000**.

[37] Strobl, G. R., *The Physics of Polymers.* Third Edition ed.; Springer: **2007**.

[38] Kubota, K.; Fujishige, S.; Ando, I., *J. Chem. Phys.*, **1990**, 94, 5154-5158.

[39] Okada, Y.; Tanaka, F., *Macrmolecules*, **2005**, 38, 4465-4471.

[40] Zimm, B. H.; Bragg, J. K., *J. Chem. Phys.*, **1959**, 31, (2), 526-535.

A.2 Scattering from concentration fluctuations

A.2.1 The aim of this section

When we derivate scattering functions which appear in the elementary text of scattering, such as scattering functions of spheres, rods and ideal polymers, $\rho(\mathbf{r})$ of these samples are given in advance and we can calculate the correlation function $g(\mathbf{r})$. However, if one imagine gels and rubbers, one comes to understand that $\rho(\mathbf{r})$ are not always clearly determined. In such a case, i.e., in the case of scattering from concentration fluctuations, Gintzburg-Landau theory is often used to obtain the scattering functions. A typical example is Orstein-Zernike function, which is famous as the scattering function of semi-dilute solutions and gels;

$$I(q) \sim \frac{1}{1+\xi^2 q^2} \qquad . \tag{A.7}$$

When we use this function as a fitting function, we obtain the correlation length ξ. Therefore, it is very important to know the physical meaning of the correlation length and to check its derivation.

A.2.2 Review on Flory-Huggins theory

In general, Ising model is frequently used to explain Landau theory. However, this theory is not well-known for polymer scientists. Thus, I try to explain Landau theory by using Flory-Huggins theory.

For ease of explanation, let us consider the compatibility of molecule A and B, both of which are same size. Each lattice sites are occupied by these molecules, and we denote the fraction of sites occupied by molecule A as ϕ. From Flory-Huggins theory, the mixing free energy is given by

$$\frac{F_{mix}}{k_B T} = f(\phi) = \phi \ln \phi + (1-\phi)\ln(1-\phi) + \chi\phi(1-\phi) \qquad . \tag{A.8}$$

Figure A.14 shows $f(\phi)$ for various χ. $f(\phi)$ is convex down for $\chi < 2$ and they prefer mixing, while in the case of $\chi > 2$, a region of negative curvature exists and the system breaks up into two phases, ϕ_1 and ϕ_2. Thus, $\chi_c = 2$ is the critical point and the concentration at the critical point $\phi_c = \dfrac{1}{2}$.

Next, let us consider the critical behavior. As an example, let us see an exponent β, which is defined as $\phi_1 - \phi_2 \sim (\chi - \chi_c)^{\beta}$. Because ϕ_1 and ϕ_2 are local minimal values for $f(\phi)$, the equation for ϕ_1 and ϕ_2 is derived by derivation of $f(\phi)$.

$$\frac{df(\phi)}{d\phi} = \ln\phi - (1-\phi)\ln(1-\phi) + \chi(1-2\phi) = 0 \tag{A.9}$$

In order to calculate a difference of ϕ_1 and ϕ_2, by considering that both values are close to $\phi_c = \frac{1}{2}$, let us change variable as $\phi = \frac{1}{2} + \delta\phi$

$$\begin{aligned} \ln\left(\frac{1}{2}+\delta\phi\right) - \ln\left(\frac{1}{2}-\delta\phi\right) - 2\chi\delta\phi = 0 \\ \therefore \ln(1+2\delta\phi) - \ln(1-2\delta\phi) - 2\chi\delta\phi = 0 \end{aligned} \tag{A.10}$$

Because $\delta\phi$ is small enough, above equation expands up to 4th order as,

$$\begin{aligned} &\left(2\delta\phi - \frac{1}{2}(2\delta\phi)^2 + \frac{2}{3!}(2\delta\phi)^3 - \frac{6}{4!}(2\delta\phi)^4\right) \\ &\quad - \left(-2\delta\phi - \frac{1}{2}(-2\delta\phi)^2 + \frac{2}{3!}(-2\delta\phi)^3 - \frac{6}{4!}(-2\delta\phi)^4\right) - 2\chi\delta\phi = 0 \end{aligned} \tag{A.11}$$

$$\therefore (\delta\phi)^3 - \frac{3}{4}(\chi-2)\delta\phi = 0 \tag{A.12}$$

Therefore, $\delta\phi = 0, \pm\frac{\sqrt{3(\chi-2)}}{2}$ and $\beta = \frac{1}{2}$.

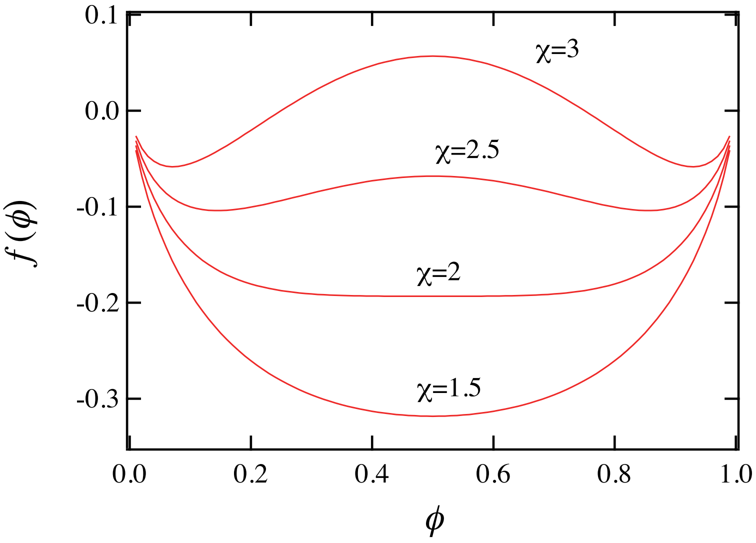

Figure A.14: Flory-Huggins free energy

A.2.3 Landau Theory

The Landau theory is a variant of mean-field theory, which does not include the elementary degrees of freedom of the statistical model. Though the Flory-Huggins free energy is derived from microscopic model on the lattice, the Landau free energy is based on symmetry considerations alone. The free energy is written as a function of the order parameter, the fraction of molecule A, ϕ and the condition of thermal equilibrium as a minimization of the free energy.

The free energy per microscopic degree of freedom or per unit volume will be written as f and is regarded as a function of ϕ. Since we are interested in the critical phenomena, the interaction parameter χ is close to the critical point χ_c, and ϕ is close to the critical value $\phi_c = \dfrac{1}{2}$. This would allow us to expand the free energy in powers of $\delta\phi = \phi - \phi_c$ and retain only the lowest-order terms. Furthermore, considering the symmetry of molecule A and B, the free energy is symmetrical around $\phi = \frac{1}{2}$. Therefore, the free energy is expected to satisfied the condition : $f(\delta\phi) = f(-\delta\phi)$, and is an even function of $\delta\phi$. Thus we get

$$f(\delta\phi) = a_0 + a_2(\delta\phi)^2 + a_4(\delta\phi)^4 \qquad . \tag{A.13}$$

It is convenient to graphically show the functional form of eq (A.13) to identify the location of minima. We first notice that a_4 should be positive. Otherwise, the free energy $f(\delta\phi)$ decreases indefinitely as $\delta\phi$ increases, which implies an instability. The $\delta\phi$ dependence of $f(\delta\phi)$ is illustrated in Figure A.15 for three possible values of the coefficient a_2. For $a_2 > 0$, the minimum is at $\delta\phi = 0$ and thus there is no phase separation. When a_2 is exactly 0, the Landau expansion starts from the fourth order and $f(\delta\phi)$ is very flat at the origin, but still the equilibrium concentration remains $\delta\phi = 0$. As soon as a_2 becomes negative, two minima emerge away from $\delta\phi = 0$ and the absolute $|\delta\phi|$ at these points grows with decreasing a_2. The original Hamiltonian and free energy are symmetric under a change of sign of $\delta\phi$, but the realized state for $a_2 < 0$ does not have such a symmetry since only one of the two minima is actually realized in a physical system. This phenomenon is called *spontaneous symmetry breaking*. A small external field of the initial condition of time evolution of the system determines which of the two states is actually realized, which is also called *ergodicity breaking* because only a part of the phase space is reached by the system.

Since the equilibrium minimum of $f(\delta\phi)$ changes at $a_2 = 0$, we identify $a_2 = 0$ with the critical point $\chi = \chi_c$. This observation would allow us to put a_2 as

$$a_2 = -b(\chi - \chi_c) \qquad , \tag{A.14}$$

where b is a positive constant. From this definition, $a_2 > 0$ corresponds to below critical point and $a_2 < 0$ to above critical point.

Let us evaluate the resulting critical exponents of the Landau theory. The exponent β is determined by the χ dependence of $\delta\phi$ that minimizes the free energy at $a_2 < 0$, i.e. $\chi > \chi_c$. Differentiation of the free energy gives the minimization condition

$$\frac{df}{d\delta\phi} = 2a_2\delta\phi + 4a_4(\delta\phi)^3 = 0 \tag{A.15}$$

$$\therefore \quad \delta\phi = \pm\left(-\frac{a_2}{2a_4}\right)^{\frac{1}{2}} = \pm\left(\frac{b(\chi - \chi_c)}{a_4}\right)^{\frac{1}{2}}, \tag{A.16}$$

from which we conclude $\beta = \dfrac{1}{2}$. Thus the critical exponent of Landau theory corresponds to that of Flory-Huggins theory, and these theories are equivalent.

The merit of Landau theory is simplicity and generality. The Landau theory uses only the symmetry properties of the free energy $f(\delta\phi)$, and predicts the resulting values for the critical exponents with taking account into the details of model systems.

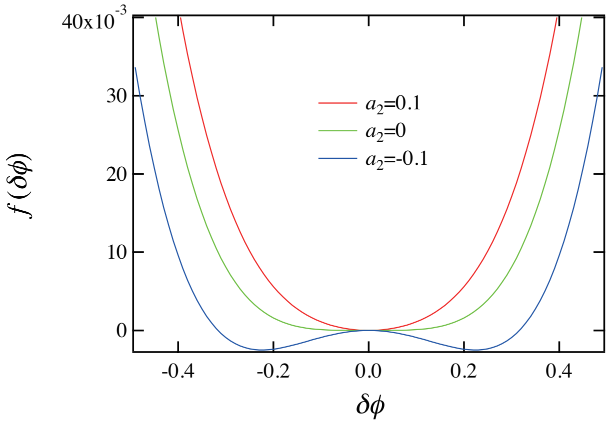

Figure A.15: The $\delta\phi$ dependence of the Landau free energy.

A.2.4 Gintzburg-Landau theory and the derivation of Orstein-Zernike function

In Landau theory, the spatial dependence of $\delta\phi$ and their interaction are not taken into account. To consider the situation, we discuss a generalization of the Landau theory in this section. This theory is called Gintzburg-Landau theory.

Suppose that the fraction of molecule A has some spatial dependence, which we write $\delta\phi(\mathbf{r}) = \phi(\mathbf{r}) - \phi_0$. By using $\delta\phi(\mathbf{r})$, the Landau free energy is generalized to the following form

$$F = \int d\mathbf{r}\Big[a_0 + a_1\delta\phi(\mathbf{r}) + a_2\delta\phi(\mathbf{r})^2 + a_4\delta\phi(\mathbf{r})^4 + \cdots + c_1(\nabla\delta\phi(\mathbf{r}))^2 + c_2(\Delta\delta\phi(\mathbf{r}))^2 + \cdots\Big] \tag{A.17}$$

At what order the expansion is truncated depends on the problem and the accuracy of description desired. The reason I explain the Gintzburg-Landau theory is that scattering function $S(\mathbf{q})$ is related to this equation.

$$F[\delta\phi(\mathbf{r})] = \frac{1}{2\beta}\int d\mathbf{q}\,(S(\mathbf{q}))^{-1}\,\delta\phi(-\mathbf{q})\delta\phi(\mathbf{q}) \tag{A.18}$$

Here, we define Fourier transformation of basic variables

$$\delta\phi(\mathbf{r}) = \frac{1}{(2\pi)^3}\int d\mathbf{q}e^{i\mathbf{q}\cdot\mathbf{r}}\delta\phi(\mathbf{q}),\ \ \delta\phi(\mathbf{q}) = \int d\mathbf{r}e^{-i\mathbf{q}\cdot\mathbf{r}}\delta\phi(\mathbf{r}) \quad . \tag{A.19}$$

The derivation of these equations is a little complicated and will be explain in the next section by using field theoretic approaches. In this section, let us derive Orstein-Zernike function. The free energy is proposed as follows.

$$F = \int d\mathbf{r}a_2\left(\delta\phi(\mathbf{r})\right)^2 + c_1\left(\nabla\delta\phi(\mathbf{r})\right)^2 \tag{A.20}$$

Here, a_2 and c_1 satisfy $a_2 > 0$ and $c_1 > 0$, respectively. By using the following equations

$$\begin{aligned}\int d\mathbf{r}\left(\delta\phi(\mathbf{r})\right)^2 &= \frac{1}{(2\pi)^6}\int d\mathbf{r}\int d\mathbf{q}e^{i\mathbf{q}\cdot\mathbf{r}}\delta\phi(\mathbf{q})\int d\mathbf{q}'e^{i\mathbf{q}'\cdot\mathbf{r}}\delta\phi(\mathbf{q}') \\ &= \frac{1}{(2\pi)^6}\int d\mathbf{r}\int d\mathbf{q}\int d\mathbf{q}'e^{i(\mathbf{q}+\mathbf{q}')\cdot\mathbf{r}}\delta\phi(\mathbf{q})\delta\phi(\mathbf{q}') \\ &= \frac{1}{(2\pi)^3}\int d\mathbf{q}\int d\mathbf{q}'\delta(\mathbf{q}+\mathbf{q}')\delta\phi(\mathbf{q})\delta\phi(\mathbf{q}') \\ &= \frac{1}{(2\pi)^3}\int d\mathbf{q}\delta\phi(\mathbf{q})\delta\phi(-\mathbf{q})\end{aligned} \tag{A.21}$$

and

$$\begin{aligned}\int d\mathbf{r}\,(\nabla\delta\phi(\mathbf{r}))^2 &= \frac{1}{(2\pi)^6}\int d\mathbf{r}\left(\nabla\int d\mathbf{q}e^{i\mathbf{q}\cdot\mathbf{r}}\delta\phi(\mathbf{q})\right)\left(\nabla\int d\mathbf{q}'e^{i\mathbf{q}'\cdot\mathbf{r}}\delta\phi(\mathbf{q}')\right)\\ &= -\frac{1}{(2\pi)^6}\int d\mathbf{r}\int d\mathbf{q}\int d\mathbf{q}'\;\;\mathbf{q}\mathbf{q}'e^{i(\mathbf{q}+\mathbf{q}')\cdot\mathbf{r}}\delta\phi(\mathbf{q})\delta\phi(\mathbf{q}')\\ &= -\frac{1}{(2\pi)^3}\int d\mathbf{q}\int d\mathbf{q}'\mathbf{q}\mathbf{q}'\delta(\mathbf{q}+\mathbf{q}')\delta\phi(\mathbf{q})\delta\phi(\mathbf{q}')\\ &= \frac{1}{(2\pi)^3}\int d\mathbf{q}q^2\delta\phi(\mathbf{q})\delta\phi(-\mathbf{q})\quad, \end{aligned}\tag{A.22}$$

we odtain

$$F=\int d\mathbf{q}(a_2+c_1q^2)\delta\phi(\mathbf{q})\delta\phi(-\mathbf{q})\quad.\tag{A.23}$$

From eq. (A.18), we get Orstein-Zernike function;

$$S(q)\sim\frac{1}{a_2+c_1q^2}\quad.\tag{A.24}$$

A.2.5 Free energy functional

Mathematical preliminary

For following sections, we present general expressions of free energy $\mathcal{F}[\{\varphi_k(\mathbf{r})\}]$ as a function of $\varphi_k(\mathbf{r})$. Let us put some definition. We consider the system S in which there are K types of polymer, the number of type k is M_k, and polymerization degree of each polymer is N. The position vector for n th segment of a th polymer of type k is denoted as $\mathbf{R}_{an}^{(k)}$, and the phase space of segments is defined as $\Gamma = \{\mathbf{R}_{an}^{(k)}\}$. The system S at equilibrium state is represented by a canonical distribution which hamiltonian is $\mathcal{H}(\Gamma) = \mathcal{H}_0(\Gamma) + \mathcal{W}(\Gamma)$. Here, $\mathcal{H}_0(\Gamma)$ is the hamiltonian for reference state and $\mathcal{W}(\Gamma)$ is an interaction term. The distribution function of the system S is given by

$$\mathcal{Z} = \frac{1}{\prod_k M_k!} \int d\Gamma \exp\left[-\beta(\mathcal{H}_0(\Gamma) + \mathcal{W}(\Gamma))\right] \quad , \tag{A.25}$$

where $d\Gamma = \prod_{k,a,n} d\mathbf{R}_{an}^{(k)}$. By using the segment distribution $\hat{\varphi}_k(\mathbf{r};\Gamma)$, the locally-averaged concentration $\varphi_k(\mathbf{r})$ of type k at position $\mathbf{r}$ is defined as

$$\varphi_k(\mathbf{r}) = \langle \hat{\varphi}_k(\mathbf{r};\Gamma)\rangle = \frac{1}{\mathcal{Z}\prod_k M_k!} \int d\Gamma \hat{\varphi}_k(\mathbf{r};\Gamma) \exp\left[-\beta\mathcal{H}(\Gamma)\right] \tag{A.26}$$

$$\hat{\varphi}_k(\mathbf{r};\Gamma) = \sum_{a,n} \delta\left(\mathbf{r} - \mathbf{R}_{an}^{(k)}\right) \quad . \tag{A.27}$$

Next let us check a condition. First we assume an incompressible condition, i.e.

$$\sum_k \varphi_k = 1, \text{ or } \sum_k \delta\varphi_k = 0 \quad . \tag{A.28}$$

In addition, we postulate that the interaction term is a function of $\hat{\varphi}_k(\mathbf{r};\Gamma)$, i.e. $\mathcal{W}(\Gamma) = \mathcal{W}\left[\hat{\varphi}_k(\mathbf{r};\Gamma)\right]$.

Under these circumstances, we apply external force on this system so that the concentration $\varphi_k(\mathbf{r})$ comes to be $\phi_k(\mathbf{r})$ and focus on the difference of free energy from the equilibrium state. The distribution function is

$$\begin{aligned}\mathcal{Z} \;=\; & \frac{1}{\prod_k M_k!} \int d\Gamma \mathcal{D}[\varphi_k(\mathbf{r})] \prod_k \delta\left(\phi_k(\mathbf{r}) - \varphi_k(\mathbf{r})\right) \delta\left(\sum_k \varphi_k(\mathbf{r}) - 1\right) \\ & \qquad \exp[-\beta\left\{\mathcal{H}_0(\Gamma) + \mathcal{W}\left[\hat{\varphi}_k(\mathbf{r};\Gamma)\right]\right\}]\end{aligned}$$

$$
\begin{aligned}
&= \frac{1}{\prod_k M_k!}\int d\Gamma \mathcal{D}[\varphi_k(\mathbf{r})]\prod_k \delta\Big(\varphi_k(\mathbf{r})-\hat{\varphi}_k(\mathbf{r};\Gamma)\Big)\prod_k \delta\Big(\phi_k(\mathbf{r})-\varphi_k(\mathbf{r})\Big)\delta\left(\sum_k \varphi_k(\mathbf{r})-1\right)\\
&\qquad \exp[-\beta\left\{\mathcal{H}_0(\Gamma)+\mathcal{W}\left[\varphi_k(\mathbf{r})\right]\right\}]\\
&\simeq \int d\Gamma \mathcal{D}[\varphi_k(\mathbf{r})]\mathcal{D}[V_k(\mathbf{r})]\mathcal{D}[\gamma_k(\mathbf{r})]\mathcal{D}[\lambda(\mathbf{r})]\\
&\quad \exp\Big[i\beta\sum_k\int V_k(\mathbf{r})\cdot\Big(\varphi_k(\mathbf{r})-\hat{\varphi}_k(\mathbf{r};\Gamma)\Big)d\mathbf{r}\Big]\\
&\quad \exp\Big[i\beta\sum_k\int \gamma_k(\mathbf{r})\cdot\Big(\phi_k(\mathbf{r})-\varphi_k(\mathbf{r})\Big)d\mathbf{r}\Big]\\
&\quad \exp\Big[i\beta\int \lambda(\mathbf{r})\cdot\Big(\sum_k \varphi_k(\mathbf{r})-1\Big)d\mathbf{r}\Big]\exp[-\beta\left\{\mathcal{H}_0(\Gamma)+\mathcal{W}\left[\varphi_k(\mathbf{r})\right]\right\}]
\end{aligned}
\tag{A.29}
$$

From line 2 to 3, we neglect a coefficient. Here, we change variables as $iV_k \to V_k$, $i\gamma_k \to \gamma_k$ and $i\lambda \to \lambda$. When we define

$$
\mathcal{Z}_0 = \frac{1}{\Pi_k M_k!}\int d\Gamma \exp[-\beta(\mathcal{H}_0(\Gamma)+\sum_k\int V_k(\mathbf{r})\cdot\hat{\varphi}_k(\mathbf{r};\Gamma)d\mathbf{r})], \tag{A.30}
$$

we obtain

$$
\begin{aligned}
\mathcal{Z} \simeq &\int \mathcal{D}[\varphi_k(\mathbf{r})]\mathcal{D}[V_k(\mathbf{r})]\mathcal{D}[\gamma_k(\mathbf{r})]\mathcal{D}[\lambda(\mathbf{r})]\\
&\exp\Big[\beta\Big(\frac{1}{\beta}\ln\mathcal{Z}_0-\mathcal{W}\left[\varphi_k(\mathbf{r})\right]+\sum_k\int V_k(\mathbf{r})\cdot\varphi_k(\mathbf{r})d\mathbf{r}\\
&+\sum_k\int\gamma_k(\mathbf{r})\cdot\Big(\phi_k(\mathbf{r})-\varphi_k(\mathbf{r})\Big)d\mathbf{r}+\int\lambda(\mathbf{r})\cdot\Big(\sum_k\varphi_k(\mathbf{r})-1\Big)d\mathbf{r}\Big)\Big]
\end{aligned}
\tag{A.31}
$$

We apply the saddle point approximation to this integration.

$$
\begin{aligned}
\frac{\delta}{\delta\ \varphi_k(\mathbf{r})}\quad &\Big[\frac{1}{\beta}\ln\mathcal{Z}_0-\mathcal{W}\left[\varphi_k(\mathbf{r})\right]+\sum_k\int V_k(\mathbf{r})\cdot\varphi_k(\mathbf{r})d\mathbf{r}\\
&+\sum_k\int\gamma_k(\mathbf{r})\cdot\Big(\phi_k(\mathbf{r})-\varphi_k(\mathbf{r})\Big)d\mathbf{r}+\int\lambda(\mathbf{r})\cdot\Big(\sum_k\varphi_k(\mathbf{r})-1\Big)d\mathbf{r}\Big]=0
\end{aligned}
\tag{A.32}
$$

$$
\begin{aligned}
\frac{\delta}{\delta\ V_k(\mathbf{r})}\quad &\Big[\frac{1}{\beta}\ln\mathcal{Z}_0-\mathcal{W}\left[\varphi_k(\mathbf{r})\right]+\sum_k\int V_k(\mathbf{r})\cdot\varphi_k(\mathbf{r})d\mathbf{r}\\
&+\sum_k\int\gamma_k(\mathbf{r})\cdot\Big(\phi_k(\mathbf{r})-\varphi_k(\mathbf{r})\Big)d\mathbf{r}+\int\lambda(\mathbf{r})\cdot\Big(\sum_k\varphi_k(\mathbf{r})-1\Big)d\mathbf{r}\Big]=0
\end{aligned}
\tag{A.33}
$$

$$\frac{\delta}{\delta\ \gamma_k(\mathbf{r})} \quad \Big[\frac{1}{\beta}\ln\mathcal{Z}_0 - \mathcal{W}\left[\varphi_k(\mathbf{r})\right] + \sum_k \int V_k(\mathbf{r})\cdot\varphi_k(\mathbf{r})d\mathbf{r}$$
$$+\sum_k \int \gamma_k(\mathbf{r})\cdot\Big(\phi_k(\mathbf{r}) - \varphi_k(\mathbf{r})\Big)d\mathbf{r} + \int \lambda(\mathbf{r})\cdot\Big(\sum_k \varphi_k(\mathbf{r}) - 1\Big)d\mathbf{r}\Big] = 0 \tag{A.34}$$

$$\frac{\delta}{\delta\ \lambda(\mathbf{r})} \quad \Big[\frac{1}{\beta}\ln\mathcal{Z}_0 - \mathcal{W}\left[\varphi_k(\mathbf{r})\right] + \sum_k \int V_k(\mathbf{r})\cdot\varphi_k(\mathbf{r})d\mathbf{r}$$
$$+\sum_k \int \gamma_k(\mathbf{r})\cdot\Big(\phi_k(\mathbf{r}) - \varphi_k(\mathbf{r})\Big)d\mathbf{r} + \int \lambda(\mathbf{r})\cdot\Big(\sum_k \varphi_k(\mathbf{r}) - 1\Big)d\mathbf{r}\Big] = 0 \tag{A.35}$$

We get from eq.(A.32)∼(A.35),

$$-\frac{\delta\mathcal{W}}{\delta\varphi_k}\Big|_{\varphi_k=\phi_k} + V_k^0 - \gamma_k^0 + \lambda^0 = 0, \tag{A.36}$$

$$\frac{1}{\beta}\frac{1}{\mathcal{Z}_0}\frac{\delta\mathcal{Z}_0}{\delta V_k}\Big|_{V_k=V_k^0} + \phi_k = 0 \tag{A.37}$$

$$\phi_k - \varphi_k = 0, \tag{A.38}$$

$$\sum_k \phi_k - 1 = 0 \tag{A.39}$$

From these assessment, above integration (eq. A.31) is

$$\mathcal{Z} \approx \mathcal{Z}_0[V_k^0]\exp\Big[-\beta\mathcal{W}\left[\phi_k(\mathbf{r})\right] + \beta\sum_k \int d\mathbf{r} V_k^0(\mathbf{r})\phi_k(\mathbf{r})\Big] \tag{A.40}$$

and thus the Helmholtz free energy is given by

$$\mathcal{F}_S[\phi_k] \approx -k_B T \ln\mathcal{Z}_0[V_k^0] + \mathcal{W}\left[\phi_k(\mathbf{r})\right] - \sum_k \int d\mathbf{r} V_k^0(\mathbf{r})\phi_k(\mathbf{r}) \quad . \tag{A.41}$$

Free energy for weak phase separation

In order to derivate eq. (A.18), we suppose that the concentration $\delta\phi_k$ fluctuates around equilibrium concentration ϕ_k^0. At this moment, we do not extract an interaction term $\mathcal{W}$ from original hamiltonian $\mathcal{H}$. We apply external force on this system so that the concentration $\delta\varphi_k(\mathbf{r}) = \varphi_k(\mathbf{r}) - \varphi_k^0$ comes to be $\delta\phi_k(\mathbf{r})$ and focus on the difference of free energy from the equilibrium state. In that case, free energy as a function of $\delta\phi_k(\mathbf{r})$ can be described by putting $\mathcal{H}_S \to \mathcal{H}$, $\mathcal{W} \to 0$, $\phi_k(\mathbf{r}) \to \delta\phi_k(\mathbf{r})$, and $V_k^0 \to V_k$ into eq.A.41.

$$\mathcal{F}[\delta\phi_k] \approx -k_B T \ln \mathcal{Z}[V_k] - \sum_k \int d\mathbf{r} V_k(\mathbf{r}) \delta\phi_k(\mathbf{r}) \quad . \tag{A.42}$$

In addition, from eq. (A.36)-(A.39), we obtain

$$\delta\phi_k(\mathbf{r}) = -\frac{1}{\beta}\frac{1}{\mathcal{Z}}\frac{\delta\mathcal{Z}}{\delta V_k} \quad . \tag{A.43}$$

As seen in eq. (A.43), V_k is the external force which introduce the concentration fluctuation $\delta\phi_k$ from the equilibrium concentration ϕ_k^0.

Next, we assume that V_k is small enough and expand $\ln \mathcal{Z}(V_k)$ with V_k. This is called cumulant expansion. When one keep in mind that

$$\ln \mathcal{Z} = \ln\Big[\frac{1}{\Pi_k M_k!} \int d\Gamma \exp[-\beta(\mathcal{H}(\Gamma) + \sum_k \int V_k(\mathbf{r}) \cdot \delta\hat{\varphi}_k(\mathbf{r};\Gamma) d\mathbf{r})]\Big] \quad , \tag{A.44}$$

the first cumulant is

$$\frac{\delta}{\delta V_k} \ln \mathcal{Z} = \frac{\int d\Gamma \beta \delta\hat{\varphi}_k(\mathbf{r};\Gamma) \exp[-\beta(\mathcal{H}(\Gamma) + \sum_k \int V_k(\mathbf{r}) \cdot \delta\hat{\varphi}_k(\mathbf{r};\Gamma) d\mathbf{r})]}{\int d\Gamma \exp[-\beta(\mathcal{H}(\Gamma) + \sum_k \int V_k(\mathbf{r}) \cdot \delta\hat{\varphi}_k(\mathbf{r};\Gamma) d\mathbf{r})]} \tag{A.45}$$

$$\therefore \frac{\delta}{\delta V_k} \ln \mathcal{Z}\Big|_{V_k=0} = \frac{\int d\Gamma \delta\hat{\varphi}_k(\mathbf{r};\Gamma) \exp[-\beta\mathcal{H}(\Gamma)]}{\int d\Gamma \exp[-\beta(\mathcal{H}(\Gamma)]} = \beta\langle\delta\hat{\varphi}_k(\mathbf{r})\rangle = 0 \quad . \tag{A.46}$$

In the same way, we obtain the second cumulant,

$$\begin{aligned} \frac{\delta^2}{\delta V_k \delta V_j} \ln \mathcal{Z}\Big|_{V_k=0} &= \beta^2(\langle\delta\hat{\varphi}_k(\mathbf{r})\delta\hat{\varphi}_j(\mathbf{r}')\rangle - \langle\delta\hat{\varphi}_k(\mathbf{r})\rangle\langle\delta\hat{\varphi}_j(\mathbf{r}')\rangle) \\ &= \beta^2\langle\delta\hat{\varphi}_k(\mathbf{r})\delta\hat{\varphi}_j(\mathbf{r}')\rangle \quad . \end{aligned} \tag{A.47}$$

Thus, the Helmholtz free energy is expanded as

$$\begin{aligned}
\mathcal{F}[\delta\phi_k] &= -\frac{1}{\beta}\ln\mathcal{Z}[V_k] \\
&\approx -\frac{1}{\beta}\ln\mathcal{Z}[0] - \frac{1}{\beta}\sum_k\int d\mathbf{r}\frac{\delta}{\delta V_k}\ln[\mathcal{Z}]\Big|_{V_k=0}V_k(\mathbf{r}) \qquad \text{(A.48)} \\
&\quad -\frac{1}{2\beta}\sum_{j,k}\int d\mathbf{r}d\mathbf{r}'\frac{\delta^2}{\delta V_k\delta V_j}\ln[\mathcal{Z}]\Big|_{V_k,V_j=0}V_k(\mathbf{r})V_j(\mathbf{r}') - \sum_k\int d\mathbf{r}V_k(\mathbf{r})\delta\phi_k(\mathbf{r}) \\
&= -\frac{1}{\beta}\ln\mathcal{Z}[0] - \frac{\beta}{2}\sum_{j,k}\int d\mathbf{r}d\mathbf{r}'\langle\delta\hat{\varphi}_k(\mathbf{r})\delta\hat{\varphi}_j(\mathbf{r}')\rangle V_k(\mathbf{r})V_j(\mathbf{r}') - \sum_k\int d\mathbf{r}V_k(\mathbf{r})\delta\phi_k(\mathbf{r}) \\
&\qquad \text{(A.49)}
\end{aligned}$$

In addition, from above equation and eq. (A.43), we obtain the linear response relation;

$$\begin{aligned}
\delta\phi_j(\mathbf{r}) &= -\frac{1}{\beta}\frac{1}{\mathcal{Z}}\frac{\delta\mathcal{Z}}{\delta V_j} \\
&\simeq -\beta\sum_k\int d\mathbf{r}'\langle\delta\hat{\varphi}_k(\mathbf{r})\delta\hat{\varphi}_j(\mathbf{r}')\rangle V_k(\mathbf{r}') \\
&= -\beta\sum_k\int d\mathbf{r}'S_{jk}(\mathbf{r}-\mathbf{r}')V_k(\mathbf{r}') \quad , \qquad \text{(A.50)}
\end{aligned}$$

where S is the scattering matrix. When we define inverse scattering matrix S^{-1};

$$\sum_k\int d\mathbf{r}'(S^{-1})_{jk}(\mathbf{r}-\mathbf{r}')S_{kl}(\mathbf{r}'-\mathbf{r}") = \delta_{jl}\delta(\mathbf{r}-\mathbf{r}") \quad , \qquad \text{(A.51)}$$

Thus eq. (A.50) becomes

$$V_j(\mathbf{r}) = -\frac{1}{\beta}\sum_k\int d\mathbf{r}'(S^{-1})_{jk}(\mathbf{r}-\mathbf{r}')\delta\phi_k(\mathbf{r}') \qquad \text{(A.52)}$$

By this expression, eq. (A.49) becomes

$$\begin{aligned}
\mathcal{F}[\delta\phi_k] &= \mathcal{F}[0] + \frac{1}{2\beta}\sum_{j,k}\int d\mathbf{r}d\mathbf{r}'(S^{-1})_{jk}(\mathbf{r}-\mathbf{r}')\delta\phi_j(\mathbf{r})\delta\phi_k(\mathbf{r}') \\
&= \mathcal{F}[0] + \frac{1}{2\beta}\sum_{j,k}\int d\mathbf{q}(S^{-1})_{jk}(\mathbf{q})\delta\phi_j(-\mathbf{q})\delta\phi_k(\mathbf{q}) \quad . \qquad \text{(A.53)}
\end{aligned}$$

In the last line, we use the Fourier transformation. If we consider the case $i = j$, we obtain eq. (A.18).

Random Phase Approximation

In general, it is difficult to calculate the scattering function S. Thus, in this section, we consider the reference state in which we conduct calculation of its scattering function S_0 in advance, and calculate the scattering function S by introducing an interaction into the reference state. In contrast to the previous section, we extract an interaction term $\mathcal{W}$ from original hamiltonian $\mathcal{H}$. From eq(A.41), the free energy is given by,

$$\mathcal{F}[\delta\phi_k] \approx -k_BT \ln \mathcal{Z}_0[V_k] + \mathcal{W}\left[\delta\phi_k\right] - \sum_k \int d\mathbf{r} V_k(\mathbf{r})\delta\phi_k(\mathbf{r}) \quad , \tag{A.54}$$

where

$$-\frac{\delta\mathcal{W}}{\delta(\delta\phi_k)} + V_k - \gamma_k + \lambda = 0 \tag{A.55}$$

$$\delta\phi_k(\mathbf{r}) = -\frac{1}{\beta}\frac{1}{\mathcal{Z}_0}\frac{\delta\mathcal{Z}_0}{\delta V_k} \tag{A.56}$$

$$\sum_k \delta\phi_k = 0. \tag{A.57}$$

As the same way from eq (A.42) to eq(A.53), eq(A.54) becomes

$$\begin{aligned}
\mathcal{F}[\delta\phi_k] &= \mathcal{F}[0] + \mathcal{W}\left[\delta\phi_k\right] + \frac{1}{2\beta}\sum_{j,k}\int d\mathbf{r}d\mathbf{r}'(S_0^{-1})_{jk}(\mathbf{r}-\mathbf{r}')\delta\phi_j(\mathbf{r})\delta\phi_k(\mathbf{r}') \\
&= \mathcal{F}[0] + \mathcal{W}\left[\delta\phi_k\right] + \frac{1}{2\beta}\sum_{j,k}\int d\mathbf{q}(S_0^{-1})_{jk}(\mathbf{q})\delta\phi_j(-\mathbf{q})\delta\phi_k(\mathbf{q}) \quad .
\end{aligned} \tag{A.58}$$

Also, we obtain the following linear response from eq(A.56) and (A.58)

$$\begin{aligned}
\delta\phi_j(\mathbf{r}) &= -\frac{1}{\beta}\frac{1}{\mathcal{Z}_0}\frac{\delta\mathcal{Z}_0}{\delta V_j} \\
&= -\beta\sum_k\int d\mathbf{r}'\langle\delta\hat{\varphi}_k(\mathbf{r})\delta\hat{\varphi}_j(\mathbf{r}')\rangle_0 V_k(\mathbf{r}') \\
&= -\beta\sum_k\int d\mathbf{r}'\left(S_0\right)_{jk}(\mathbf{r}-\mathbf{r}')V_k(\mathbf{r}') \quad ,
\end{aligned} \tag{A.59}$$

where $\langle * \rangle_0$ denotes

$$\langle * \rangle_0 = \frac{\displaystyle\int d\Gamma * \exp[-\beta\mathcal{H}_0(\Gamma)]}{\displaystyle\int d\Gamma \exp[-\beta\mathcal{H}_0(\Gamma)]}. \tag{A.60}$$

From eq(A.50) and eq(A.61), we get

$$\begin{aligned}\delta\phi_j(\mathbf{r}) &= -\beta\sum_k \int d\mathbf{r}' S_{jk}(\mathbf{r}-\mathbf{r}')V_k(\mathbf{r}') \\ &= -\beta\sum_k \int d\mathbf{r}' \left(S_0\right)_{jk}(\mathbf{r}-\mathbf{r}')\left(\frac{\delta\mathcal{W}}{\delta(\delta\phi_k)}+\gamma_k+\lambda\right) \qquad \text{(A.61)}\end{aligned}$$

When above equation is Fourier transformed, we get

$$\delta\phi_j(\mathbf{q}) = -\beta\sum_k S_{jk}(\mathbf{q})V_k(\mathbf{q}) = -\beta\sum_k \left(S_0\right)_{jk}(\mathbf{q})\left(\frac{\delta\mathcal{W}}{\delta(\delta\phi_k)}+\gamma_k+\lambda\right). \qquad \text{(A.62)}$$

The concept of this approximation is that S_{jk} can be approximately obtained by combining $(S_0)_{jk}$ with an interaction $\dfrac{\delta\mathcal{W}}{\delta(\delta\phi_k)}$. This approximation is often called “Random Phase Approximation”.

Application to polymer blends

Consider the system containing two kinds of polymer A and B. We set the reference state as follows. (i) Incompressible condition is not applied. (ii) An interaction between A and B does not exist. (iii) Each polymer behaves as a Gauss chain. The interaction term $\mathcal{W}[\delta\phi_k]$ is given by

$$\mathcal{W}[\delta\phi_k] = -\int d\mathbf{r}\left(\frac{1}{2}\epsilon_{AA}\delta\phi_A^2 + \epsilon_{AB}\delta\phi_A\delta\phi_B + \frac{1}{2}\epsilon_{BB}\delta\phi_B^2\right). \tag{A.63}$$

At the equilibrium state of system S, from incompressible condition $\delta\hat{\phi}_A + \delta\hat{\phi}_B = 0$, we get

$$S_{AA} = S_{BB} = -S_{AB} = -S_{BA} \equiv S_S(\mathbf{q}). \tag{A.64}$$

When we define $\delta\phi$ as $\delta\phi_A = -\delta\phi_B = \delta\phi$, we obtain from eq(A.62)

$$-\frac{1}{\beta}\delta\phi_A = -\frac{1}{\beta}\delta\phi = S_S(\mathbf{q})[\gamma_A - \gamma_B] \tag{A.65}$$

$$= (S_0)_{AA}(\mathbf{q})[\gamma_A - (\epsilon_{AA} - \epsilon_{AB})\delta\phi + \lambda] + (S_0)_{AB}(\mathbf{q})[\gamma_B - (-\epsilon_{AB} + \epsilon_{BB})(-\delta\phi) + \lambda] \tag{A.66}$$

$$-\frac{1}{\beta}\delta\phi_B = \frac{1}{\beta}\delta\phi = S_S(\mathbf{q})[\gamma_B - \gamma_A] \tag{A.67}$$

$$= (S_0)_{BA}(\mathbf{q})[\gamma_A - (\epsilon_{AA} - \epsilon_{AB})\delta\phi + \lambda] + (S_0)_{BB}(\mathbf{q})[\gamma_B - (-\epsilon_{AB} + \epsilon_{BB})(-\delta\phi) + \lambda] \tag{A.68}$$

We delete λ from eq(A.66) and eq(A.68), and we obtain

$$\delta\phi = -\beta\frac{1}{\tilde{S_0}^{-1}(\mathbf{q}) - 2\chi}[\gamma_A - \gamma_B], \tag{A.69}$$

where

$$\tilde{S_0}^{-1}(\mathbf{q}) = \frac{(S_0)_{AA} + (S_0)_{AB} + (S_0)_{BA} + (S_0)_{BB}}{(S_0)_{AA}(S_0)_{BB} - (S_0)_{AB}(S_0)_{BA}}. \tag{A.70}$$

From eq(A.65) and eq(A.67), we obtain

$$\delta\phi = -\beta S_S(\mathbf{q})(\gamma_A - \gamma_B) = -\beta\frac{1}{\tilde{S_0}^{-1}(\mathbf{q}) - 2\chi}[\gamma_A - \gamma_B]. \tag{A.71}$$

Therefore, the problem is to calculate $(S_0)_{jk}$ of polymer melt.

Let us consider polymer blend of polymer A and B. The numbers of polymer A and B are M_A and M_B, and the polymerization degree of polymer A and B are N_A and N_B, respectively. When V denotes a system volume, we obtain

$$\bar{\phi}_A = \langle \hat{\phi}_A \rangle_0 = \frac{M_A N_A}{V} \tag{A.72}$$

$$\bar{\phi}_B = \langle \hat{\phi}_B \rangle_0 = \frac{M_B N_B}{V}. \tag{A.73}$$

Because there is no correlation between segments of A and B,

$$(S_0)_{AB} = (S_0)_{BA} = \langle \delta\hat{\phi}_A \delta\hat{\phi}_B \rangle_0 = \langle \delta\hat{\phi}_A \rangle_0 \langle \delta\hat{\phi}_B \rangle_0 = 0. \tag{A.74}$$

In addition, when we put X as an alternate for A or B, because each polymer behaves as a Gauss chain,

$$\begin{aligned}
(S_0)_{XX} = \langle \delta\hat{\phi}_X(\mathbf{r}) \delta\hat{\phi}_X(\mathbf{r}') \rangle_0 &= \langle (\hat{\phi}_X(\mathbf{r}) - \bar{\phi}_A)(\hat{\phi}_X(\mathbf{r}') - \bar{\phi}_B) \rangle_0 \\
&= \sum_{m,n} \langle \delta\left(\mathbf{r} - \mathbf{R}_m^X\right) \delta\left(\mathbf{r}' - \mathbf{R}_n^X\right) \rangle_0 - \bar{\phi}_X^2 \\
&= \frac{1}{V} \sum_{m,n} \langle \delta\left(\mathbf{x} - \mathbf{R}_m^X + \mathbf{R}_n^X\right) \rangle_0 - \bar{\phi}_X^2 \\
&= \bar{\phi}_X \left(g_X(\mathbf{x}) - \bar{\phi}_X\right),
\end{aligned} \tag{A.75}$$

where $g_X(\mathbf{x})$ is the correlation function of segments and defined as

$$g_X(\mathbf{x}) = \frac{1}{M_X N_X} \sum_{m,n} \langle \delta\left(\mathbf{x} - \mathbf{R}_m^X + \mathbf{R}_n^X\right) \rangle_0. \tag{A.76}$$

The correlation function for ideal polymer is known as Debye function.

$$g_X(\mathbf{q}) = N_X D\left(q^2 R_g^2\right) \tag{A.77}$$

$$D(x) = \frac{2}{x^2}\left(e^{-x} - 1 + x\right) \approx \begin{cases} \frac{2}{x} & (x \gg 1) \\ 1 - \frac{x}{3} & (x \ll 1) \end{cases} \tag{A.78}$$

Because $(S_0)_{XX}(\mathbf{q}) = \bar{\phi}_X g_X(\mathbf{q})$, we obtain from eq(A.71) and (A.74)

$$\begin{aligned}
S_S^{-1}(\mathbf{q}) = S_0^{-1}(\mathbf{q}) - 2\chi &= \frac{1}{(S_0)_{AA}(\mathbf{q})} + \frac{1}{(S_0)_{BB}(\mathbf{q})} - 2\chi \\
&= \frac{1}{\bar{\phi}_A g_A(\mathbf{q})} + \frac{1}{\bar{\phi}_B g_B(\mathbf{q})} - 2\chi \\
&\approx \frac{1}{\bar{\phi}_A N_A} + \frac{1}{\bar{\phi}_B N_B} - 2\chi + \frac{b^2 \bar{\phi}_0}{18 \bar{\phi}_A \bar{\phi}_B} |\mathbf{q}|^2,
\end{aligned} \tag{A.79}$$

where $\bar{\phi}_0 = \bar{\phi}_A + \bar{\phi}_B$. This is a scattering function for polymer blend. By using these expressions, we obtain the following free energy.

$$\begin{aligned}\mathcal{F}[\delta\phi_k] &= \mathcal{F}[0] + \frac{1}{2\beta}\int d\mathbf{q}\left(\frac{1}{\bar{\phi}_A N_A} + \frac{1}{\bar{\phi}_B N_B} - 2\chi + \frac{b^2\bar{\phi}_0}{18\bar{\phi}_A\bar{\phi}_B}|\mathbf{q}|^2\right)|\delta\phi(\mathbf{q})|^2 \\ &= \mathcal{F}[0] + k_BT\int d\mathbf{r}\left[\frac{1}{2}\left(\frac{1}{\bar{\phi}_A N_A} + \frac{1}{\bar{\phi}_B N_B} - 2\chi\right)\delta\phi^2(\mathbf{r}) + \frac{b^2\bar{\phi}_0}{36\bar{\phi}_A\bar{\phi}_B}|\nabla\delta\phi(\mathbf{r})|^2\right] \end{aligned}\tag{A.80}$$

At the end, let us confirm the relation to Flory-Huggins theory. From eq(A.80), we obtain

$$\left.\frac{\delta^2\mathcal{F}}{\delta\phi_A^2}\right|_{\phi_A=\phi_A} = \left.\frac{\delta^2\mathcal{F}}{\delta(\delta\phi)^2}\right|_{\delta\phi=0} = k_BT\left(\frac{1}{N_A\bar{\phi}_A} + \frac{1}{N_B\bar{\phi}_B} - 2\chi\right). \tag{A.81}$$

When we postulate that $\bar{\phi}_A$ is $\phi_A(\mathbf{r})$ and integrate eq(A.81) under boundary condition: $\mathcal{F}[\phi_A(\mathbf{r}) = 0]$ and $\mathcal{F}[\phi_A(\mathbf{r}) = 1]$, we obtain

$$\mathcal{F}[\phi_A] = k_BT\int d\mathbf{r}\left[\frac{1}{N_A}\phi_A(\mathbf{r})\ln\phi_A(\mathbf{r}) + \frac{1}{N_B}(1-\phi_A(\mathbf{r}))\ln(1-\phi_A(\mathbf{r})) + \chi\phi_A(\mathbf{r})(1-\phi_A(\mathbf{r}))\right]. \tag{A.82}$$

This equation corresponds to Flory-Huggins theory. When we use this expression for eq(A.80), we obtain

$$\begin{aligned}\mathcal{F}[\phi_A] = k_BT\int d\mathbf{r}[&\frac{1}{N_A}\phi_A(\mathbf{r})\ln\phi_A(\mathbf{r}) + \frac{1}{N_B}(1-\phi_A(\mathbf{r}))\ln(1-\phi_A(\mathbf{r})) \\ &+\chi\phi_A(\mathbf{r})(1-\phi_A(\mathbf{r})) + \frac{b^2\bar{\phi}_0}{36\bar{\phi}_A\bar{\phi}_B}|\nabla\delta\phi(\mathbf{r})|^2],\end{aligned}\tag{A.83}$$

which is called "Flory-Huggins-de Gennes free energy".

List of Publications

Original Papers

1. K. Nishi, K. Fujii, M. Chijiishi, Y. Katsumoto, U. Chung, T. Sakai, and M. Shibayama, "Kinetic Study for AB-Type Coupling Reaction of Tetra-Arm Polymer", *Macromolecules*, **45**, 1031-1036, (2012)
   (**Chapter 2**)

2. K. Nishi, K. Fujii, Y. Katsumoto, T. Sakai, and M. Shibayama, "Kinetic Aspect on Gelation Mechanism of Tetra-PEG Hydrogel", *submitted*
   (**Chapter 3**)

3. K. Nishi, M. Chijiishi, Y. Katsumoto, T. Nakao, K. Fujii, U. Chung, H. Noguchi, T. Sakai, and M. Shibayama, "Rubber Elasticity for Incomplete Polymer Networks", *J. Chem. Phys.*, **137**, 1-7, (2012)
   (**Chapter 4**)

4. K. Nishi, H. Noguchi, T. Sakai, and M. Shibayama, "Real-space renormalization and effective-medium approximation on percolation of phantom polymer networks", *submitted* (**Chapter 5**)

5. K. Nishi, H. Asai, K. Fujii, Y.-S. Han, T.-H. Kim, T. Sakai, and M. Shibayama, "Small-Angle Neutron Scattering Study on Defect-Controlled Polymer Networks", *Macromolecules*, *accepted*
   (**Chapter 6**)

Other publications

- K. Nishi, T. Hiroi, K. Hashimoto, K. Fujii, Y.-S. Hang, T.-H. Kim, Y. Katsumoto, M. Shibayama, "SANS and DLS Studies of the tacticity effects on the hydrophobicity and the phase separation of poly(N-isopropylacrylamide)", *Macromolecules*, **46**, 6225-6232, (2013).

- H. Asai, K. Fujii, K. Nishi, T. Sakai, K. Ohara, Y. Umebayashi, M. Shibayama, "Solvation Structure of Poly(ethylene glycol) in Ionic Liquids Studied by High-energy X-ray Diffraction and Molecular Dynamics Simulations", *Macromolecules*, **46**, 2369-2375, (2013).

- H. Asai, K. Nishi, H. Takashi, K. Fujii, T. Sakai, and M. Shibayama, "Gelation Process of Tetra-PEG Ion-gel Investigated by Time-Resolved Dynamic Light Scattering", *Polymer*, **54**, 1160-1166, (2013)

- M. Kurakazu, T. Katashima, M. Chijiishi, K. Nishi, Y. Akagi, T. Matsunaga, M. Shibayama, U. Chung, and T. Sakai, "Evaluation of Gelation Kinetics of Tetra-PEG Gel", *Macromolecules*, **43**, 3935-3940, (2010)

Acknowledgements

This thesis is based on the study carried out in the research group of Professor Ung-il Chung at Department of Bioengineering, Graduate School of Engineering, The University of Tokyo from 2008 to 2011 and Professor Mitsuhiro Shibayama at Department of Advanced Materials Science, Graduate School of Frontier Sciences, The University of Tokyo from 2011 to 2014.

First of all, I would like to express my sincere gratitude to **Professor Mitsuhiro Shibayama** for giving many chances and research environment throughout my life in laboratory. Especially, I learned a model for how to live as a scientist from his passion for research.

I am deeply grateful to thank **Professor. Ung-il Chung** and **Dr. Takamasa Sakai** for guiding me into gel science. Their research projects on Tetra-PEG gel always excited and motivated me. What I learned from them is the basis of my research career.

I would like to acknowledge valuable advices and helpful discussions given by **Dr. Kenta Fujii**. His vast knowledge on chemistry and positive attitude on research and life always help me.

I would also like to thank **Dr. Yukiteru Katsumoto** for teaching me IR measurement technique and providing good samples. I am really impressed by his enthusiasm and commitment.

I want to thank **Dr. Hiroshi Noguchi** for his help for simulation. The simulation result plays an important role in this thesis. His advices on my work are always essential and important for me.

I am deeply grateful to **Dr. Toshio Nakao**. He understands me every time and is a good supporter for me. I show my respect for his profound knowledge and way of life as a scientist. I'll never forget his word in my life.

My special thanks are extended to my colleagues of all present and past members of Shibayama laboratory, Chung laboratory and all the staff of the Institute of Solid State Physics, The University of Tokyo, for their kind cooperation.

I am deeply indebted to my family for their support, patience, and encouragement during the course of my work.

March, 2014
Kengo Nishi